NTNU – Trondheim
Norwegian University of
Science and Technology

Mathematical Modelling of a Foil Propulsion System

Fridtjof Camillo Eitzen

Marine Technology
Submission date: June 2012
Supervisor: Sverre Steen, IMT
Co-supervisor: Asgeir Sørensen, IMT
Eirik Bøckmann, IMT

Norwegian University of Science and Technology
Department of Marine Technology

Scope of work

MASTER THESIS IN MARINE TECHNOLOGY
SPRING 2012
for
Fridtjof Camillo Eitzen

NTNU Trondheim
Norwegian University of Science and Technology
Department of Marine Technology

One of the potential technologies for fuel saving of ships is to utilise wave power for propulsion. Attaching foils to a ship, and using the relative vertical motions between the water and the ship, is an old concept which has received renewed attention over the last few years. Mostly, due to increasing bunker prices and increasing environmental concerns. The increasing capabilities and availability (reduced cost) of active control systems suggest that active control of the foils (most likely the geometric angle of attack) could be an attractive improvement of the wave propulsion system. This is in comparison to previous systems, which have applied fixed-foils or foils with passive-control (spring-loaded). The aims for the master thesis are to investigate the gain in thrust that can be obtained by the use of active control and to outline the control system. On this background, it is recommended that the student shall do the following in the thesis:

- Select a suitable case vessel
- Establish a mathematical model for the wave propulsion system (including the motions of the ship)
- Use the mathematical model to explore the various options; fixed foil, spring-loaded foil, and actively controlled foil. Various control strategies will need to be explored here
- Use a few example operational scenarios to quantify the performance gains of using active control

In the thesis, the candidate shall present his personal contribution to the resolution of problem within the scope of the thesis work. Theories and conclusions should be based on mathematical derivations and/or logic reasoning identifying the various steps in the deduction. The candidate should utilise the existing possibilities for obtaining relevant literature.

The thesis should be organised in a rational manner to give a clear exposition of results, assessments, and conclusions. The text should be brief and to the point, with a clear language. Telegraphic language should be avoided.

The thesis shall contain the following elements: A text defining the scope, preface, list of contents, summary, main body of thesis, conclusions with recommendations for further work, list of symbols and acronyms, reference and (optional) appendices. All figures, tables and equations shall be enumerated.

The supervisor may require that the candidate, in an early stage of the work, present a written plan for the completion of the work. The plan should include a budget for the use of computer and laboratory resources that will be charged to the department. Overruns shall be reported to the supervisor.

The original contribution of the candidate and material taken from other sources shall be clearly defined. Work from other sources shall be properly referenced using an acknowledged referencing system.

In case computer programs have been made as part of the thesis work, the source code shall be included. In case of experimental work, the experimental results shall be included in a suitable electronic format.

Supervisor : Professor Sverre Steen
Advisor : Eirik Bockmann
Start : 10.01.2012
Deadline : 10.06.2012

Trondheim, 10.06.2012

Sverre Steen
Supervisor

Preface

This report is the Master Thesis of Fridtjof Camillo Eitzen, in fulfilment of the degree at the Department of Marine Technology, at the Norwegian University of Science and Technology (NTNU), in Trondheim. It corresponds to a full semester's work load. The thesis is supervised by Professor Sverre Steen and advisor PhD-candidate Eirik Bockmann. The project was advocated by Eirik Bockmann, and the study presented in following report is meant as support to his Doctoral Thesis. Professor Sverre Steen is also Bockmann's supervisor, on his Doctoral Thesis at NTNU.

I have worked hard on the project, but still, I miss out on a large amount of the work projected by Steen. The original scope of the project was to evaluate and compare the effects of using active foil control against conventional fixed-foils or spring-loaded equivalents. However, the task has been more intricate and complicated than first expected, and I have thus decided to deviate slightly from the scope. The thesis has evolved into a study of mathematical modelling techniques for the foil propulsion system. Rather than focusing on the control of the foil, the focus has shifted towards identifying the forces on the foil system.

I am grateful to my supervisor Professor Sverre Steen at the Department of Marine Technology (NTNU) who has been orderly and helpful along the process. Additionally, I would like to thank Asgeir Sorensen for his shared insight and contributions.

I would especially like to thank Thor Inge Fossen, Professor of Guidance, Navigation and Control at NTNU, for invaluable help in the process of understanding the physics of a dynamical system. He has been exceptionally wholehearted, and I am grateful for the time and effort he has put into sharing his knowledge with me. In close cooperation, we have established a link between the Coriolis term in the body-fixed equation of motion and the speed dependent hydrodynamic coefficients from potential theory.

Finally, I would like to extend my sincerest thanks to Eirik Bockmann of whom I have shared many discussions. I am highly grateful for the opportunity I was given to work on this project, to participate in model tests and to be introduced for foil dynamics.

Thank you.

Trondheim, June 10th, 2012 **Fridtjof Camillo Eitzen**

Summary

This thesis considers a foil propulsion system on a supply vessel. In analysing the potential of a foil propulsion system, it is imperative to establish a rigid mathematical model. In that respect, modelling of the dynamic system is emphasised, and a comprehensive study is presented on the matter.

The equations of motion for an oscillating foil and a vessel are derived, separately. The two systems are then combined, to form the coupled vessel-foil structure. For the vessel, a time-domain model based on *Cummins*' equation is proposed. *Cummins*' equation has proven efficient in assessing a unified seakeeping and manoeuvring problem (Fossen [2011]). In line, the vessel-foil system will be exposed to both vessel oscillatory motion due to waves and forward speed effects, i.e seakeeping and manoeuvring. Moreover, the efficiency of the foil is directly dependent on the two.

Additionally, aspects of foil control is looked into. In theory, active control could maximise thrust while preventing stall, which would be ideal. The validity of simulations with active control, however, is highly dependent on the accuracy of the *basic* vessel-foil model. Consequently, effort has been focused on presenting a rigid mathematical foundation.

Contents

Scope of work i

Preface iii

Summary v

1 Introduction 1

I Mathematical Modelling 3

2 Ship Model 5
- 2.1 Potential theory 5
  - 2.1.1 Conservation of Mass 6
  - 2.1.2 Conservation of Momentum 7
  - 2.1.3 Forces 8
  - 2.1.4 Boundary Conditions 8
- 2.2 Boundary Value Problem (BVP) 9
- 2.3 Radiation potential 10
  - 2.3.1 *Cummins*' formulation 11
  - 2.3.2 Strip-theory 12
- 2.4 Excitation potential 13
- 2.5 Second-order effects 14
  - 2.5.1 Added resistance in waves 14
  - 2.5.2 Calm water resistance 15
- 2.6 Equations of motion 17
  - 2.6.1 Frequency-domain model 17
  - 2.6.2 *Cummins*' equation 18
  - 2.6.3 *Ogilvie*'s transformation 18
  - 2.6.4 Time-domain model 20
  - 2.6.5 State-space model 21
- 2.7 Forward speed effects 22
  - 2.7.1 *Salvesen*, *Tuck* and *Faltinsen* 1970 22
  - 2.7.2 Energy approach 25
- 2.8 System coefficients 25
  - 2.8.1 ShipX-VERES 25
  - 2.8.2 FDI MSS toolbox 28

3 Unified Seakeeping and Maneuvering model 29
3.1 Preliminaries . . . 29
3.1.1 Orientation . . . 29
3.1.2 Notation . . . 29
3.1.3 Coefficients . . . 31
3.2 Rigid-body kinetics . . . 31
3.2.1 Newton-Euler equations of motion . . . 32
3.2.2 *Kirchhoff's* equations . . . 34
3.3 Seakeeping- to body frame . . . 35
3.3.1 Kinematics . . . 35
3.3.2 Kinetics . . . 38
3.4 Energy approach . . . 39
3.5 Comparing to STF . . . 40
3.6 Verification . . . 43

4 Foil Model 47
4.1 Foil theory . . . 47
4.1.1 Quasi-static lifting theory . . . 48
4.1.2 Unsteady lifting theory . . . 49
4.1.3 Drag . . . 51
4.2 Oscillating foil . . . 53
4.2.1 Circulatory forces . . . 53
4.2.2 Non-circulatory forces . . . 54
4.2.3 Forces on oscillating foil . . . 54
4.2.4 Open-loop stability . . . 55
4.2.5 Closed-loop stability . . . 56
4.3 Controller . . . 56
4.3.1 PID-controller . . . 56
4.3.2 PD-controller . . . 57
4.4 Equation of motion . . . 58
4.4.1 Frequency-domain . . . 61
4.4.2 Time-domain . . . 62
4.5 Thrust . . . 62
4.5.1 Time-averaged thrust . . . 63
4.5.2 Time-domain thrust . . . 65
4.6 Active control . . . 65
4.6.1 The controller . . . 66
4.6.2 Spring-loaded foil . . . 66

II Model Tests 67

5 Models 69
5.1 Foil system . . . 70

6 Marine Cybernetics Lab 71
6.1 Experimental set up . . . 71
6.2 The experiments . . . 71
6.2.1 Quasi-static approach . . . 71

6.2.2 Dynamic approach 74
6.2.3 Scenario 1: No stall 75
6.2.4 Scenario 2: Stalling 75
6.2.5 Thrust 76

7 MARINTEK Towing Tank 79
7.1 Experimental set up 79
7.2 The experiment 80
7.2.1 Time-series 80
7.2.2 RAO's 80
7.2.3 Angle of attack 83
7.2.4 Lift, drag and thrust 84
7.2.5 Total resistance 85
7.2.6 Calm water resistance 85
7.2.7 Added resistance 85
7.3 Concluding remarks 88
7.4 Active control 88
7.4.1 Hardware and Software 89

III Mathematical Simulation 95

8 Choice of Model 97

9 The Model and Verification 99
9.1 Ship model 99
9.2 Foil model 101
9.3 Extended Simulations 101
9.3.1 Regular and irregular seas 103

10 Conclusions and Discussions 107

11 Recommendations for Further Work 109

Bibliography I

Appendices III

A Rigid-body kinetics III

B Programming flow IX

Nomenclature

Vectors and Matrices

Bold types are used to denote vectors and matrices

Symbols

α	Angle of attack
β	Angle of oblique sea
$\boldsymbol{\mu}$	State-space representation of the retardation function $\boldsymbol{K}$
$\boldsymbol{\nu}$	Body-fixed linear velocity
$\boldsymbol{\tau}$	An arbitrary external force
$\boldsymbol{\tau}_{foil}$	Forces from foil in the vessel equation of motion
$\boldsymbol{\tau}_{hs}$	Hydrostatic force due to hydrostatic pressure
$\boldsymbol{\tau}_{hyd}$	Hydrodynamic force due to hydrodynamic pressure
$\boldsymbol{\tau}_{wave1}$	First-order wave forces
$\boldsymbol{\tau}_{wave2}$	Second-order wave forces
$\boldsymbol{\xi}$	Motion vector in seakeeping coordinates
$\boldsymbol{A}$	Added mass coefficient
$\boldsymbol{B}$	Potential damping coefficient
$\boldsymbol{C}$	Restoring coefficient
$\boldsymbol{C}_A^*$	Coriolis and centrifugal terms due to added mass rotation about seakeeping frame
$\boldsymbol{C}_{RB}^*$	Coriolis and centrifugal terms due to rigid-body rotation about to seakeeping frame
$\boldsymbol{C}_A^{VERES}$	Coriolis and centrifugal terms due to rigid-body rotation compared to STF
$\boldsymbol{C}_A$	Coriolis and centrifugal terms due to added mass rotation about earth;fixed frame
$\boldsymbol{C}_{RB}$	Coriolis and centrifugal terms due to rigid-body rotation about earth;fixed frame
$\boldsymbol{g}$	Acceleration due to gravity vector
$\boldsymbol{H}$	System transfer function
$\boldsymbol{I}$	Identity matrix
$\boldsymbol{K}$	Retardation function
$\boldsymbol{L}$	Characteristic matrix
$\boldsymbol{M}$	Inertia matrix
$\boldsymbol{n}$	Normal vector
$\boldsymbol{r}_g$	Position vector of CG with regards to CO
$\boldsymbol{R}_{AW}$	Added resistance

$\boldsymbol{U}$	A characteristic velocity vector
$\boldsymbol{v}$	Characteristic velocity
$\ddot{\boldsymbol{\xi}}$	Acceleration vector in seakeeping coordinates
δ	*Dirac*'s impulse function
$\dot{\boldsymbol{\xi}}$	Velocity vector in seakeeping coordinates
Γ	Circulation
Λ	Aspect ratio
λ	Froude-scaling factor
μ	Fluid viscosity
∇	Laplace operator
ω	Wave angular frequency
ω_0	Eigenfrequency of system
ω_e	Angular frequency of encounter
Φ	Characteristic foil angle
ϕ	Velocity potential
ϕ_0	Incident wave potential
ϕ_D	Diffraction potential
ϕ_R	Radiation potential
ψ	Unit velocity potential
ρ	Characteristic density
ρ_m	Density of fresh-water (model-test)
ρ_s	Density of sea-water (full-scale ship)
φ	Unit velocity potential
ς	Relative damping factor
ζ	Wave elevation
ζ_a	Wave amplitude
a	One-dimensional added mass coefficient
a	One-dimensional restoring coefficient
A_{ij}	Element ij of the added mass coefficient
b	One-dimensional potential damping coefficient
B_{ij}	Element ij of the potential damping coefficient
C	An arbitrary constant
c	Cord length
$C(k_f)$	*Theodorsen* function, dependent on reduced frequency k_f
C_D	Drag coefficient
C_L	Lift coefficient
C_{ij}	Element ij of the restoring coefficient
CG	Centre of gravity
CO	Centre of origin of vessel (seakeeping frame)
F_j	An arbitrary force in j-direction
g	Acceleration of 9.81 kg/ms^2
K_d	Regulator derivative gain
k_f	Reduced frequency
K_i	Regulator integral gain
K_p	Regulator proportional gain
K_{ij}	Element ij of the retardation function matrix
L_{WL}	Length on waterline of vessel
m	One-dimensional mass

MSS	Marine Systems Simulator, Fossen and Perez [2004]
p	Pressure
s	Complex coordinate
s	Span width
S_0	Boundary at vessel hull for the Laplace domain
$S_{\pm\infty}$	Infinite boundary for the Laplace domain
S_B	Boundary at free-surface for the Laplace domain
S_B	Boundary at sea-bed for the Laplace domain
STF	Salvesen, Tuck and Faltinsen potential theory, Salvesen et al. [1970]
T	Kinetic energy
T	Wave period
t	Time
u	Linear velocity component of $\boldsymbol{v}$ in body-fixed frame in x-direction (surge)
v	Linear velocity component of $\boldsymbol{v}$ in body-fixed frame in y-direction (sway)
w	Linear velocity component of $\boldsymbol{v}$ in body-fixed frame in z-direction (heave)
x	Inertial x-position
x_f	Position of foil with regards to CO in x-direction
y	Inertial y-position
y_f	Position of foil with regards to CO in y-direction
z	Inertial z-position
z_f	Position of foil with regards to CO in z-direction
ξ_3	Linear velocity component of $\boldsymbol{\xi}$ in z-direction (heave)
ξ_4	Angular velocity component of $\boldsymbol{\xi}$ about x-axis (roll)
ξ_5	Angular velocity component of $\boldsymbol{\xi}$ about y-axis (pitch)
h	Water depth
R_T	Total calm water resistance
U	Forward speed of vessel

!

List of Figures

2.1 Laplace domain 6
2.2 VERES and STF axes 22
2.3 Reference frames 26
2.4 Added mass curve in heave 27
2.5 Damping curve in heave 27
2.6 Fitted added mass and damping curves 28

3.1 Transformation between reference frames 30
3.2 Coordinate system orientation 30
3.3 Eart-fixed-, seakeeping and body-fixed reference frame 35
3.4 Frequency response of vessel at 8 knots in heave 44
3.5 Frequency response of vessel at 8 knots in pitch 44
3.6 Frequency response of vessel at 10 knots in heave 44
3.7 Frequency response of vessel at 10 knots in pitch 44
3.8 Frequency response of vessel at 12 knots in heave 45
3.9 Frequency response of vessel at 12 knots in pitch 45

4.1 Circulation and induced velocity on foil 48
4.2 Unsteady effect on foil 49
4.3 Effective angle of attack of foil 50
4.4 Thedorsen function 51
4.5 Fitted Theodorsen function 52
4.6 Oscillating foil 53
4.7 Open- and closed-loop foil systems 56
4.8 PID-controller 57
4.9 Step-response of foil system 59
4.10 Forces and angles of foil 59
4.11 Frequency response of vessel at 10 knots in heave with foil 62
4.12 Frequency response of vessel at 10 knots in pitch with foil 62
4.13 Time-domain SIMULINK model 63
4.14 Characteristic angles and forces on foil in unsteady flow 63
4.15 Thrust for vessel with foil 65

5.1 Vessel 3D drawing from ShipX 69
5.2 Foil system, including struts, motor and force transducers 70

6.1 Experimental set up in Marine Cybernetics Lab 72

6.2 Lift coefficients for NACA15 at $R_n = 2.3e5$ 73
6.3 Drag coefficients for NACA15 at $R_n = 2.3e5$ 73
6.4 Pressure nozzles on the foil 73
6.5 Quasi-static lift coefficient versus angle of attack 74
6.6 Quasi-static pressure difference interpolation chart 74
6.7 Angle of attack and lift forces from experiments at $\xi_{3a} = 0.0886m$ 76
6.8 Oscillatory and non-oscillatory forces at $\xi_{3a} = 0.0886m$ 77
6.9 Angle of attack and lift forces from experiments at $\xi_{3a} = 0.135m$ 77
6.10 Oscillatory and non-oscillatory forces at $\xi_{3a} = 0.135m$ 78
6.11 Thrust forces below stall angle 78
6.12 Thrust forces on the verge of stalling 78

7.1 Experimental set up in towing tank 79
7.2 Time series results from towing-tank in model-scale 81
7.3 Heave reduction from experiments 82
7.4 Pitch reduction from experiments 82
7.5 Experimental RAO in heave at 8 knots 82
7.6 Experimental RAO in pitch at 8 knots 82
7.7 Experimental RAO in heave at 10 knots 83
7.8 Experimental RAO in pitch at 10 knots 83
7.9 Experimental RAO in heave at 12 knots 83
7.10 Experimental RAO in pitch at 12 knots 83
7.11 Angle of attack of foil in towing tank 84
7.12 Lift on foil in towing tank 85
7.13 Thrust force on foil in towing tank 85
7.14 Resistance reduction from experiments 86
7.15 Calm water resistance from experiments 86
7.16 Thrust force at 8 knots 87
7.17 Added resistance at 8 knots 87
7.18 Thrust force at 10 knots 87
7.19 Added resistance at 10 knots 87
7.20 Thrust force at 12 knots 88
7.21 Added resistance at 12 knots 88
7.22 Simulation Interface Toolkit flowchart, in MATLAB 90
7.23 LabView and CompactRio interface flowchart 92
7.24 Picture taken of the experimental set up, from above 93

9.1 Vessel block diagram with force RAO 99
9.2 Vessel block 100
9.3 Time-domain- versus steady-state response for zero speed 101
9.4 Time-domain- versus steady-state response at 12 knots 101
9.5 Combined vessel and foil model in SIMULINK 101
9.6 Foil block in SIMULINK 102
9.7 Time-domain heave response with foil at 8 knots 102
9.8 Time-domain pitch response with foil at 8 knots 102
9.9 Time-domain heave response with foil at 12 knots 103
9.10 Time-domain pitch response with foil at 12 knots 103
9.11 Thrust for extended model at 8 and 12 knots 104
9.12 Thrust for extended model at 8 and 12 knots in irregular sea 104

9.13 JONSWAP spectrum 105
9.14 Sea-state visualisation 105

A.1 Rigid-body kinematics IV
A.2 Geometry of vessel at an exaggerated angle, at forward speed VI

List of Tables

2.1 Resistance scaling from model- to full-scale 16
2.2 Heave- and pitch added mass and damping coefficients from STF-theory . . . 24

4.1 Features of a PID-controller 56
4.2 Added mass-, potential damping- and restoring coefficients due to the foil . . 61

5.1 Principal hull data and dimensions for the UT-751 design vessel in full- and model-scale 69
5.2 Principal dimensions for the NACA-0015 foil in full- and model-scale 70

7.1 Run data for towing tank 80

Chapter 1

Introduction

In times of increased environmental awareness, and strong competition in the maritime sector, development of innovative vessel concepts is of acknowledged importance. A vessel oscillating in waves is exposed to large amounts of kinetic and potential energy. By harvesting *some* of that energy, a vessel could increase its energy efficiency, prove more environmental friendly and benefit economically. This thesis considers a foil propulsion system and attempts to verify the potential associated with its employment.

PhD candidate Eirik Bockmann at Norwegian University of Science and Technology, is writing his Doctoral Thesis on the subject of foil propulsion. This report is meant as support to his work, where the overall objective is to verify whether a foil system is commercially viable. That being said, the main emphasis has been put into establishing a solid mathematical model. Thereafter, the model could hopefully serve as a basis for evaluating the potential of a vessel-foil system.

The concept of foil propulsion is based on mounting a submerged wing in the bow-section of a vessel. The foil utilises the relative vertical motion between the wing and the water particles to create lift. In theory, the lift acts normal to the direction of the incoming flow. As the vessel oscillates, the incoming angle of attack will oscillate, and some of the lift force is directed forwards, as thrust.

In optimising the thrust the application of an active controller is discussed. In active control, the foil is steered towards an optimal angle of attack. The optimal angle is calculated from the ratio between the lift- and drag coefficients, and in the report the coefficients are identified from experimental data. However, in controlling the foil the actual angle of attack must also be a known variable. The application of pressure sensors and theoretical calculations is used in finding the actual angle. Control theory is presented, although no valid simulations were performed. The reason being that the application and simulation of a fixed foil was complicated enough to verify.

The angle of attack is dependent on the vessel motion. Therefore, a rigid simulation model is necessary for the foil forces to be modelled correctly. A time-domain model is chosen for the purpose. The model is compared with computational results from VERES and experimental data from model tests.

An outline of the important discussions in the report follows:

Part I :
Different vessel models are discussed. The classical frequency-domain model is derived from potential theory, and a time-domain model using *Cummins*' formulation is proposed. The formulation adopts a fluid memory term to account for the frequency dependency of the hydrodynamic coefficients. The fluid memory term is evaluated using a state-space approximation. The time-domain model is chosen as the principle system for assessing the foil propulsion system. VERES is used extensively in verification of the method. An energy approach is utilised to account for forward speed effects

Part II :
The aspects of foil modelling is studied, and foil control is exemplified. In this part, the foil model is combined with the vessel model to form the coupled vessel-foil system

Part III :
Model tests have been performed and the results are presented. Data from the model tests of the foil is used to complement the mathematical model. The experimental results are also used in verification of the simulation model proposed

Part IV :
Results form preliminary simulations is described. A conclusion is formulated

Part I

Mathematical Modelling

Chapter 2

Ship Model

The following chapter will propose various approaches in modelling a vessel, and discuss their associated strengths and weaknesses. As a basis for the discussion, it is emphasised that a linear (or linearised) system can be analysed in the frequency-domain, while any non-linear system is operated in the time-domain.

The vessel can be modelled as a floating body satisfying Newton's second law in six-degrees of freedom

$$\boldsymbol{M}\ddot{\boldsymbol{\xi}} = \boldsymbol{\tau}_{hyd} + \boldsymbol{\tau}_{hs} + \boldsymbol{\tau}_{foil} \tag{2.1}$$

where $\boldsymbol{M} = \boldsymbol{M}_{6\times6}$ is the inertia matrix, $\ddot{\boldsymbol{\xi}} = \ddot{\boldsymbol{\xi}}_{6\times1}$ is the acceleration of the system state-variables and $\boldsymbol{\tau}_{\{\}} = \boldsymbol{\tau}_{\{\}6\times1}$ expresses the forces acting on the body. $\boldsymbol{\tau}_{hyd}$ can be understood as the forces induced due to hydrodynamic pressure. Hydrodynamic pressure arise due to both vessel- and wave motion and $\boldsymbol{\tau}_{hyd}$ consists of radiation-, diffraction- and Froude-Krylov-forces. Both the radiation- and diffraction are found by solving a zero-penetration boundary value problem for the body-surface. The Froude-Krylov forces originate from integration, of the hydrodynamic pressure due to the presence of waves, over the body-surface. Further, $\boldsymbol{\tau}_{hs}$ is the restoring force due to changing hydrostatic pressure (buoyancy), as the body oscillates vertically. The above forces are found by solving boundary value problems under potential theory and will be elucidated in the coming sections.

2.1 Potential theory

The domain or control-volume, in which the body from (2.1) floats, is shown in figure 2.1. It is restricted by the boundaries $S_{-\infty}, S_{\infty}, S_0, S_B$ and S_F (all $\in S$), where S_B is the body surface and S_F the free-surface.

In potential theory, the following assumptions must be valid throughout the domain

1. Conservation of mass and -momentum apply

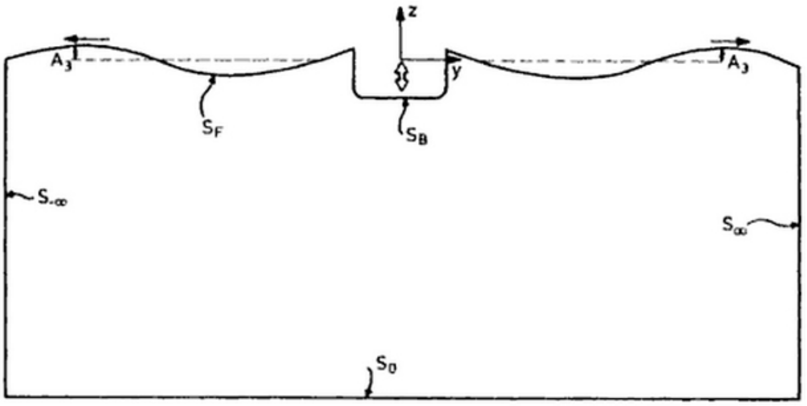

Figure 2.1: The domain and boundaries of the Laplace fluid surrounding the floating body. Courtesy of [Faltinsen, 1990, pg.46]

2. The fluid is incompressible → $\rho = constant$
3. The flow-field is irrotational and continuous → the field is conservative

2.1.1 Conservation of Mass

From the definition of conserved mass, and by employing the divergence theorem, we obtain

$$\frac{dm}{dt} = \iint\limits_S \rho \mathbf{v} \cdot \mathbf{n} \; dS = \iiint\limits_V \operatorname{div}(\rho \mathbf{v}) \; dV = 0 \tag{2.2}$$

where the velocity at an arbitrary position can be described by the vector $\mathbf{v} = u\mathbf{i} + v\mathbf{j} + w\mathbf{k}$ and $\mathbf{n}$ is the normal vector at the surface, S. The double integral can be understood as the net flux of mass through the control-volume bound by S, which must equal to zero for conservation of mass to be fulfilled. As the fluid is assumed incompressible, the density of water, ρ is considered constant and can be cancelled out of the expression. (2.2) is valid for every infinitesimal part of the domain and we thereby derive the continuity equation

$$\operatorname{div}(\mathbf{v}) = \nabla \cdot \mathbf{v} = \frac{\partial u}{\partial x} + \frac{\partial v}{\partial y} + \frac{\partial w}{\partial z} = 0 \tag{2.3}$$

In the above, it is presumed that the velocity field is continuous throughout the domain. Further, the domain is considered conservative, which in mathematical terms means that any line integral is path independent. In physical terms, it implies that energy is not lost, only replaced. A conservative vector-field is also irrotational, and can be described using mathematical potentials as

$$\mathbf{v} = \nabla \phi \tag{2.4}$$

where $\phi = \phi(x, y, z, t)$ is a scalar. By introducing (2.4) in the continuity equation of (2.3), it follows that the potential must satisfy the *Laplace* equation

$$\nabla^2 \phi = 0 \tag{2.5}$$

The process of describing the flow-field, of an incompressible and irrotational fluid, reduces to finding the solution of the Laplace equation, with the relevant boundary conditions. The solutions to the *Laplace* partial differential equation are harmonic functions, and the study of such functions is known as potential theory.

2.1.2 Conservation of Momentum

From conservation of momentum, the *Navier-Stokes* equations appear as

$$\underbrace{\rho\left(\frac{\partial \mathbf{v}}{\partial t} + \mathbf{v} \cdot \nabla \mathbf{v}\right)}_{\frac{D\mathbf{v}}{Dt}} = \rho \mathbf{g} - \nabla p + \mu \nabla^2 \mathbf{v} \tag{2.6}$$

where the parentheses on the left form the *total* vector field-acceleration, $\mathbf{g} = [0, 0, -g]$ are the accelerations due to body forces, $p = p(x, y, z, t)$ is the pressure at an arbitrary point and μ is the fluid viscosity.

It is common to neglect the effects of viscosity and assume water to be inviscid. In that case, the *Navier-Stokes* equations reshapes to form the *Euler* equations

$$\rho \frac{D\mathbf{v}}{Dt} - \rho \mathbf{g} + \nabla p = 0 \tag{2.7}$$

The pressure can be found by integrating over a path, $d\mathbf{s}$, and substituting for the velocity potential. The result is recognised as the unsteady *Bernoulli* equation

$$p + \rho \frac{\partial \phi}{\partial t} + \rho \frac{|\nabla \phi|^2}{2} + \rho g z = C \tag{2.8}$$

where C is interpreted as the total pressure at an arbitrary point in the domain. C must be constant for conservation of momentum, in an inviscid fluid, to apply. By using the fact that the total pressure at the free-surface *is* atmospheric, we impose the relation $C = p_0$, and accept that $p = p_0$ and $z = \zeta$. Consequently, under linear theory, the dynamic free-surface boundary condition must hold

$$\left.\frac{\partial \phi}{\partial t} + g\zeta = 0\right|_{z=0} \tag{2.9}$$

By reorganising and linearising, equation 2.8 becomes

$$p - p_0 = -\rho \frac{\partial \phi}{\partial t} - \rho g z \tag{2.10}$$

For a floating body in equilibrium, the forces of interest arise due to a change in hydrodynamic- or hydrostatic pressure. Ergo, the relative pressure is of essence, and p_0 is conveniently set to zero, implying that $p = \Delta p$.

2.1.3 Forces

Force due to pressure is governed by the expression; $d\mathbf{F} = p\mathbf{n}dS$. Introducing (2.10), and generalizing, the expression yields

$$\sum_{j=1}^{6} F_j = \iint\limits_{S} \left(-\rho \frac{\partial \phi}{\partial t} - \rho g z\right) dS \tag{2.11}$$

where F_j is the force due to hydrodynamic- and hydrostatic pressure, in a given degree of freedom, j. The hydrodynamic force from (2.1) is recognised as

$$\boldsymbol{\tau}_{hyd} = \iint\limits_{S} -\rho \frac{\partial \phi}{\partial t}\ dS \tag{2.12}$$

while the hydrostatic force is

$$\boldsymbol{\tau}_{hs} = \iint\limits_{S} -\rho g z\ dS \tag{2.13}$$

By denoting the motion in an arbitrary point as $z = \xi_3 + y\xi_4 - x\xi_5$, we obtain

$$\tau^{i}_{hs} = -\sum_{j=1}^{6} \xi_j\ C_{ij} \tag{2.14}$$

where C_{ij} is the restoring force coefficient.

Now that the forces, from Newton's second law (from (2.1)), are identified we turn our attention to finding the unknown potential, ϕ, for the Laplacian fluid.

2.1.4 Boundary Conditions

From Faltinsen [1990], we define the boundary condition for the free-surface and body-surface to be

$$\frac{\partial \phi}{\partial n} = \boldsymbol{U}\mathbf{n} \quad \in\ S_B, S_F \tag{2.15}$$

where $\boldsymbol{U}$ is a characteristic velocity. On the free-surface the characteristic velocity in the vertical direction can be approximated (under linear theory) by the time derivative of the wave elevation, ζ. Thus, a linear approximation of the kinematic free-surface boundary condition reads

$$\frac{\partial \phi}{\partial z} = \frac{\partial \zeta}{\partial t}\bigg|_{z=0} \tag{2.16}$$

The kinematic- and dynamic boundary conditions (from (2.16) and (2.9), respectively) can be combined to form the general boundary expression

$$\frac{\partial^2 \phi}{\partial^2 t} + g\frac{\partial \phi}{\partial z} = 0\bigg|_{z=0} \tag{2.17}$$

For a given point on the rigid body, translatory and rotary effects are included to make up the characteristic velocity. The boundary condition thereby implies that, the velocity of the body at a given point *is* the same as the velocity of the fluid at that same point. Moreover, (2.15) is also valid at the sea-bottom S_0, at $z = -h$, where h is the water depth, by setting $\boldsymbol{U} = 0$.

2.2 Boundary Value Problem (BVP)

Let us now imagine a floating vessel subjected to a single wave, what will happen? The wave hits the vessel, and energy transferred from the wave to the vessel. Next, due to the excitation force, the vessel is perturbed from equilibrium and starts to oscillate. As the vessel oscillates, it sets up a wave-field where energy is transmitted away from the body by the radiating waves. Finally, as all the energy is dissipated it reaches equilibrium once more. In short, the floating vessel behaves like a mass-spring-damper system, and the wave is an impulse force. Such a system can be modelled as

$$a\ddot{\xi}(t) + b\xi(t) + c\xi(t) = \delta(t) \tag{2.18}$$

where ξ is the state variable, $[a, b, c]$ are the system coefficients and δ is the impulse wave force. The steady-state solution is

$$\xi(s) = \frac{c}{1 + 2\varsigma\frac{s}{\omega_0} + \left(\frac{s}{\omega_0}\right)^2} \tag{2.19}$$

where $\varsigma = \frac{b}{2m\omega_0}$ is the relative damping factor and $\omega_0 = \sqrt{c/m}$ is the eigenfrequency. We seek to find the system coefficients and the excitation force. The system coefficients are found from a radiation BVP while the force is found by solving an excitation BVP. Under potential theory superposition is valid and we can split the problem in two: the radiation- and excitation problem. Greco [2010] denotes the total potential as

$$\phi = \phi_R + \phi_0 + \phi_D \tag{2.20}$$

where ϕ_R is the radiation potential and $\phi_0 + \phi_D$ is the potential from solving the excitation problem. The complete potential must satisfy the boundary conditions for the domain.

2.3 Radiation potential

A radiation potential is the induced wave potential due to radiating waves, as the vessel is perturbed from equilibrium. In finding the potential, Newman [1977] proposed a solution which has served as the basis for the frequency-domain formulation. Cummins [1962] formulated a time-domain approach, while Ogilvie [1964] made the transformation between the two procedures.

Newman [1977] suggested the radiation potential in all degrees of freedom (hereby referred to as DOF) take the form

$$\phi_R = \sum_{j=1}^{6} \dot{\xi}_j(t)\psi_j(t,\mathbf{r}) \qquad \text{where} \qquad \frac{\partial \psi_j}{\partial n_j} = n_j \tag{2.21}$$

Here, ψ_j is the potential per unit velocity, dependent on time, position and frequency of oscillation (Newman [1977]) and ξ is the velocity of the vessel in the j^{th} mode. Introducing this potential to (2.12), yields the hydrodynamic force due to radiation

$$\tau_R^i = \iint\limits_S -\rho \frac{\partial \phi_R}{\partial t}\, dS = -\sum_{j=1}^{6} \ddot{\xi}_j \rho \iint\limits_S \psi_j dS - \sum_{j=1}^{6} \dot{\xi}_j \rho \iint\limits_S \dot{\psi}_j dS \tag{2.22}$$

$$= -\sum_{j=1}^{6} \ddot{\xi}_j A_{ij} - \sum_{j=1}^{6} \dot{\xi}_j B_{ij} \tag{2.23}$$

and

$$A_{ij} = A_{ij}(\omega) = \rho \iint\limits_S \psi_j dS \tag{2.24}$$

$$B_{ij} = B_{ij}(\omega) = \rho \iint\limits_S \dot{\psi}_j dS = i\omega\rho \iint\limits_S \psi_j dS \tag{2.25}$$

where A_{ij} and B_{ij} are the frequency dependent added mass- and damping coefficient. This notation serves as the basis for what is commonly known as the frequency-domain seakeeping model. The model is used extensively in literature and will be explained in detail within the coming sections. Nevertheless, it is important to beware that the formulation is only valid for steady-state response under influence of a sinusoidal force (oscillation at a single, unique frequency), and does not account for transient dynamics (Cummins [1962]). In other words, the formulation fail to fulfil its boundary condition at $t = \tau$ (initial condition), during an impulse forcing, $\delta(t - \tau)$.

2.3.1 *Cummins*' formulation

Cummins [1962] derived a procedure for evaluating the forces acting on a vessel, using impulse response function in a convolution integral, thereby accounting for transient dynamics. The procedure will be outlined in the following bulk.

Again, we consider an impulse force, acting on the body at $t = \tau$. This time, we also contemplate that the instantaneous velocity of the body is proportional to *Dirac*'s delta function, $\dot{\xi}(t) = \delta(t{-}\tau)$ during the impulse. This implies that, the body will displace according to a step-function, as the integral of a the delta function is a step. The instantaneous change in velocity must be included in the total fluid potential for the problem to satisfy the given boundary conditions, entirely. After the impulse, the body will oscillate and decay according to the potential in (2.21).

Let us now examine the boundary conditions a little closer. We know that the wave elevation initial condition must be: $\zeta = 0$ and $\dot{\zeta} \neq 0$. The dynamic boundary condition can then be satisfied if, and only if, $\phi = 0$. Furthermore, as $\phi = 0$ and $\dot{\zeta} \neq 0$, the kinematic boundary condition fail. In order to satisfy both boundary conditions for all t an additional potential must be derived. Let the impulse potential be $\phi_R^j\Big|_{t=\tau}$ so that the total potential from (2.20) becomes

$$\phi = \phi_R + \phi_R^j\Big|_{t=\tau} + \phi_0 + \phi_D \tag{2.26}$$

The potential of the impulse can be estimated according to (2.21), as

$$\phi_R^j\Big|_{t=\tau} = \delta_j(t-\tau)\varphi_j(\mathbf{r}) \tag{2.27}$$

where the unit potential, φ_j is independent on time and frequency (Cummins [1962]) and $\dot{\xi}(t) = \delta(t-\tau)$. From the kinematic free-surface boundary condition we get

$$\delta_j(t)\frac{\partial \varphi_j}{\partial z} = \frac{\partial \zeta}{\partial t}\Big|_{z=0} \quad \rightarrow \quad \zeta = \frac{\partial \varphi_j}{\partial z}\Big|_{z=0} \qquad \text{as} \qquad \int_{-\infty}^{\infty} \delta(t) = 1 \tag{2.28}$$

Consequently, both boundary conditions are satisfied at the initial condition; $\zeta = 0$ and $\varphi_j = 0$, at $t = \tau$.

Furthermore, it is known that arbitrary motion can be described by convolution integrals. A convolution integral can be interpreted as the sum of impulse responses, hence it must, under linear theory (superposition), be valid for the same boundary conditions as the unique impulse potential, $\phi_R^j\Big|_{t=\tau}$. *Cummins* proves this statement and generalises (2.27), for an arbitrary motion

$$\phi_R^j\Big|_{t=\tau} = \int_{-\infty}^{t} \varphi_j(t-\tau)\delta_j(\tau)d\tau \tag{2.29}$$

where the impulse potential in equation (2.27) is reformulated into a convolution integral by

$$\int_{-\infty}^{t} \varphi_j(t-\tau)\delta_j(\tau)d\tau = \int_{-\infty}^{t} \delta_j(t-\tau)\varphi_j(\tau)d\tau = \delta_j(t-\tau)\varphi_j(\tau) \tag{2.30}$$

Now, by the same reasoning as presented by Newman [1977], *Cummins* introduces the potential in (2.21), which satisfies the general boundary condition (combined kinematic and dynamic), from (2.17). Subsequently, a complete potential in all DOF, valid for all t, yields

$$\phi_R^j = \dot{\xi}_j\psi_j + \int_{-\infty}^{t} \varphi_j(t-\tau)\dot{\xi}(\tau)d\tau \tag{2.31}$$

Similarly to the *Newman*'s procedure, the hydrodynamic forces due to radiation is found through

$$\tau_R^i = \iint_S -\rho\frac{\partial\phi_R^j}{\partial t}dS \tag{2.32}$$

$$= -\sum_{j=1}^{6}\left[A_{ij}\ddot{\xi}_j + B_{ij}\dot{\xi}_j + \int_{-\infty}^{t} K_{ij}(t-\tau)\dot{\xi}_j(\tau)d\tau\right] \tag{2.33}$$

where

$$A_{ij} = \rho\iint_S \psi_j dS \tag{2.34}$$

$$B_{ij} = \rho\iint_S \dot{\psi}_j dS \tag{2.35}$$

and

$$K_{ij}(t-\tau) = \rho\iint_S \frac{\partial\varphi_j(t-\tau)}{\partial t}dS \tag{2.36}$$

Here, $K_{ij}(t-\tau)$ is the retardation function which accounts for fluid memory effects. The unit velocity potentials, φ and ψ are still deemed unknown. They can be found from strip-theory. Consequently, both $\boldsymbol{A}$ and $\boldsymbol{B}$ will be known.

2.3.2 Strip-theory

In finding the system coefficients the potential, ψ must be identified. This is normally done by strip-theory (2-D potential theory) or panel methods (3-D potential theory). In strip-theory, the vessel is divided into a finite number of *strips* that are deemed two-dimensional under a slender-body approximation. Hence, the 2-D coefficients are determined by 2-D potential theory. The coefficients for the body as a whole can thus be found by summarising the contributions from the lone strips (Faltinsen [1990]). Hydrodynamic codes, such as MARINTEK's ShipX-VERES (hereby referred to as VERES), use strip-theory to determine these coefficients.

2.4 Excitation potential

In the following, we seek a potential describing the propagation of incident, regular waves in the domain, as well as the diffraction potential due to interaction between waves and the vessel. The potential due to incident waves can be found by solving the boundary value problem for the domain (from (2.17) and (2.5)). The procedure is covered extensively in many publications (Newman [1977], Dean and Dalrymple [1991]) and will not be emphasised in this report. The potential can be represented by the following

$$\phi_0 = \frac{g\zeta_a}{\omega} e^{kz} e^{ik(x\cos\beta + y\sin\beta)} e^{i\omega_e t} \tag{2.37}$$

where ω is the wave frequency, β is the wave propagation direction and ζ_a is the wave amplitude. The vector $\mathbf{r} = x\mathbf{i} + y\mathbf{j} + z\mathbf{k}$ is the position at where we are analysing ϕ_0, while ω_e is the encounter frequency given by

$$\omega_e = \omega + kU\cos\beta \tag{2.38}$$

From (2.37) and the dynamic free-surface condition in (2.9), the wave elevation can be seen to be

$$\begin{aligned} \zeta &= -i\zeta_a e^{ik(x\cos\beta + y\sin\beta)} e^{i\omega t} && (2.39) \\ &= \zeta_a \cos(\omega t + \theta(\beta, \mathbf{r})) && (2.40) \end{aligned}$$

where $z = 0$ and $\omega_e = \omega$.

The diffraction potential can be found in a similar manner as the radiation potential. The essential boundary condition assures that no water penetrates the hull and is given by (derived from (2.15))

$$\frac{\partial \phi_D}{\partial n} = \frac{\partial \phi_0}{\partial n} \tag{2.41}$$

where ϕ_0 and ϕ_D is the incident- and diffraction potential, respectively. In this report, the incident- and diffraction potential will be accounted for as one (in accordance with the output from the computational programs used). The resulting hydrodynamic force can be found according to equation (2.12) from

$$\tau_{wave1} = \iint_S -\rho \frac{\partial(\phi_0 + \phi_D)}{\partial t}\, dS \tag{2.42}$$

where the force due to the incident potential is characterised as the Froude-Krylov force. The total first-order force, due to hydrodynamic pressure from waves and diffraction, is denoted τ_{wave1}. By means of strip-theory, the force can be calculated efficiently in hydrodynamic computational programs where the output would be on the form

$$\tau^i_{wave1} = F^i_{wave1}(\omega)\zeta \tag{2.43}$$

where

$$F^i_{wave1} = |F^i_{wave1}|e^{\angle F^i_{wave1}} \tag{2.44}$$

and

$$|F^i_{wave1}| = \sqrt{\mathrm{Im}\{F^i_{wave1}\}^2 + \mathrm{Re}\{F^i_{wave1}\}^2} \tag{2.45}$$

$$\angle F^i_{wave1} = \arctan\left(\frac{\mathrm{Im}\{F^i_{wave1}\}}{\mathrm{Re}\{F^i_{wave1}\}}\right) \tag{2.46}$$

F^i_{wave1} from (2.43) is a force response amplitude operator (hereby denoted RAO), which can be represented by its characteristic transfer-function ($|F^i_{wave1}(\omega)|$) and phase-shift function ($\angle F^i_{wave1}(\omega)$), under complex theory. These results will be adopted at a later stage.

2.5 Second-order effects

2.5.1 Added resistance in waves

In the previous sections, linear potential theory has been applied to define the forces on a vessel oscillating in a fluid. However, there will be substantial contributions to the force picture from non-linear effects, and they should be accounted for. We will reduce ourselves to identifying the second-order wave drift loads, which are the source of what is referred to as added resistance. We shall see that the added resistance is highly dependent on the relative vertical velocity between the ship and waves. In that respect, it is an important parameter when assessing the benefits of using a submerged foil system on a vessel, as a foil reduces the ship motion in both pitch and heave, and thus influence the added resistance.

In exemplifying the concept, we shall implement the direct pressure integration method (Pinkster and van Oortmessen [1977], Faltinsen [1990]). Waves interact with a two-dimensional, vertical body in a fluid. By assuming short wavelength i.e high frequency, the body can be regarded as fixed. As incident waves are diffracted from the fixed body, the resulting wave-field is made up of two waves travelling in opposite direction, which in fact is a standing wave. The standing wave at the body (say $x = 0$) can then be expressed as

$$\begin{align} \zeta_{tot} &= \zeta_a \cos(\omega t + kx) + \zeta_a \cos(\omega t - kx) \tag{2.47} \\ &= 2\zeta_a \cos(\omega t)|_{x=0} \tag{2.48} \end{align}$$

The second-order drift forces from direct pressure integration method arise due to:

1. Second-order solution to the Laplace equation; $\phi = \phi_0 + \phi_2$
2. A change of integration limits in the Bernoulli equation; $-\infty$ to ζ
3. Inclusion of the velocity-squared term in the Bernoulli equation; $|\nabla\phi|^2$

The second-order solution, ϕ_2 do not contribute to drift loads as the time-averaged integral is zero. Furthermore, the pressure from Bernoulli's equation is usually evaluated from $z = -\infty$ to $z = 0$ at infinite water depth, which also give no contributions to a mean force. However, when changing the upper limit to $z = \zeta$, a constant drift force will appear. Additionally, the squared velocity will give drift if evaluated from $z = -\infty$ to $z = 0$. Here, $z = 0$ is used as the upper limit as $z = \zeta$ would bring about fourth order forces.

Hence, the pressure to be integrated over the surface of the body is now

$$p = -\rho g z - \rho\frac{\partial\phi}{\partial t} - \rho\frac{|\nabla\phi|^2}{2} \tag{2.49}$$

Meanwhile, the drift force is found by a time-averaged integral given as

$$\tau = \overline{-\rho\int\limits_0^{\zeta}\left(gz + \frac{\partial\phi_{tot}}{\partial t}|_{z=0}\right)dz} - \overline{\frac{\rho}{2}\int\limits_{-\infty}^{0}|\nabla\phi_{tot}|^2 dz} \tag{2.50}$$

By using a potential and a wave elevation corresponding to the standing wave in (2.47), the total force sums to match Maruo's formula for short wavelengths:

$$\tau_{wave2} = \frac{1}{2}\rho g\zeta_a \tag{2.51}$$

It can be understood as the force due to diffraction of waves. Faltinsen has derived a formula which extends the applicability of (2.51) and account for forward speed ([Faltinsen, 1990, pg.145]). It should be noted that, diffraction is governing only in a high-frequency environment. For larger wavelengths, added resistance due to resonance or radiation is what governs the force picture.

As the body resonates in waves, the wetted surface of the body is dependent on the relative motion between the ship and the waves, not only the wave motion, as was the case for diffraction. Gerritsma and Beukelman [1972] showed the correlation between relative motion and added resistance and derived a widely-used formula for added resistance. It is adopted by for instance VERES (Fathi and Hoff [2010]) and VERES' estimate of added resistance will be used later in this report.

As a concluding remark, Faltinsen [1990] shows how (2.51) can be approximated to account for relative vertical motion by setting $\zeta_a = \zeta_R$. Here, ζ_R is the relative displacement between wave and body.

2.5.2 Calm water resistance

Calm water resistance of a full-scale vessel can be estimated based on scaling theory and model tests. When scaling a model it is imperative that there exist a similarity in geometry, kinematics and kinetics (Steen [2007]). This implies that, both the Froude- and Reynolds-number must remain unchanged in model- and full-scale. Froude-similarity can easily be obtained, however consistency in Reynolds number is hardly possible. The friction force coefficient is dependent on Reynold's number. In order to obtain complete similarity a pull-force must be applied to the model, to account for the difference in friction coefficients.

According to Steen [2007] the calm water resistance is calculated by the following algorithm:

• $C_{Rm} = C_{T_m} - C_{Vm}$	*Residual coeff. model scale*
– $C_{Tm} = \frac{R_{Tm}}{\frac{1}{2}\rho_m V_m^2 S_m}$	*Total coeff. model scale*
– $C_{Vm} = (1+k)C_{Fm}$	*Viscous coeff. model scale*
– $C_{Fm} = \frac{0.075}{(log(Rnm)-2)^2}$	*Friction ITTC-57 coeff. model scale*
– $Rnm = \frac{V_m L_{WLm}}{\nu_m}$	*Reynolds number model scale*
• $C_{Rs} = C_{Rm}$	*Froude scaling*
• $C_{Ts} = C_{Rs} + C_{Vs}$	*Total resistance coeff. full scale*
– $C_{Vs} = (1+k)(C_{Fs} + \Delta C_F)$	*Viscous coeff. full scale*
– $\Delta C_F = [110(HV)^{0.21} - 403]C_{Fs}$	*Roughness friction coeff. full scale*
– $C_{Fs} = \frac{0.075}{(log(Rns)-2)^2}$	*Friction ITTC-57 coeff. full scale*
– $Rns = \frac{V_s L_{WLs}}{\nu_s}$	*Reynolds number model scale*
• $R_{Ts} = \frac{C_{Ts}}{\frac{1}{2}\rho_s V_s^2 S_s}$	*Total resistance full scale*

Table 2.1: Resistance scaling from experimental data in model scale to full scale resistance estimates. All of the equalities, given above, are dimensionless resistance coefficients (apart from the Reynolds number, which is a dimensionless parameter). '*coeff.*' is short for coefficient, and m denotes model scale- and s full scale values. V is speed, k is a form-factor, S is wetted surface, L_{WL} is the water-line length, H (dimension μm) is an estimated roughness factor and ν is fluid viscosity. All equations are recited from Steen [2007]

From 2.1, the total calm water resistance can be found to be

$$R_{Ts} = \lambda^3 \frac{\rho_s}{\rho_m}\left(R_{Tm} + \underbrace{(1+k)[C_{Fs} + \Delta C_F - C_{Fm}]\frac{1}{2}\rho_m V_m^2 S_m}_{F_s} \right) \tag{2.52}$$

where the latter term, in the parentheses, is the tow-force, F_s. $\lambda = \frac{L_{WLs}}{L_{WLm}}$ is the Froude scaling factor. The calm water resistance will be used later in the report.

2.6 Equations of motion

Newton's second law and rigid-body kinetics in seakeeping coordinates yields

$$\boldsymbol{M}\ddot{\boldsymbol{\xi}} = \boldsymbol{\tau}_{hyd} + \boldsymbol{\tau}_{hs} + \boldsymbol{\tau}_{foil} \tag{2.53}$$

where

$$\boldsymbol{\tau}_{hyd} = \iint\limits_{S} -\rho \frac{\partial(\phi_0 + \phi_D + \phi_R)}{\partial t}\, dS \qquad\qquad \boldsymbol{\tau}_{hs} = \iint\limits_{S} -\rho g z \; dS \tag{2.54}$$

In reformulating, using the identities in (2.42) and (2.32), the problem simplifies to

$$\begin{aligned}
\boldsymbol{\tau}_{hyd} &= \boldsymbol{\tau}_{R} + \boldsymbol{\tau}_{wave1} \\
&= -\left[\boldsymbol{A}(\omega)\ddot{\boldsymbol{\xi}} + \boldsymbol{B}(\omega)\dot{\boldsymbol{\xi}} + \int\limits_{-\infty}^{t} \boldsymbol{K}(t-\tau)\dot{\boldsymbol{\xi}}(\tau)d\tau\right] + \boldsymbol{\tau}_{wave1} \qquad (2.55)\\
\boldsymbol{\tau}_{hs} &= -\boldsymbol{C}\boldsymbol{\xi} \qquad (2.56)
\end{aligned}$$

and

$$[\boldsymbol{M} + \boldsymbol{A}(\omega)]\ddot{\boldsymbol{\xi}} + \boldsymbol{B}(\omega)\dot{\boldsymbol{\xi}} + \int\limits_{-\infty}^{t} \boldsymbol{K}(t-\tau)\dot{\boldsymbol{\xi}}(\tau)d\tau + \mathbf{C}\boldsymbol{\xi} = \boldsymbol{\tau}_{wave1} \tag{2.57}$$

where the system coefficients $\boldsymbol{A}(\omega)$ and$\boldsymbol{B}(\omega)$ are assumed known by strip-theory. Equation (2.57) is both time- and frequency dependent and is therefore unsuited for analysis in either the time- or frequency-domain.

2.6.1 Frequency-domain model

By assuming the equation to be on the form of a classical mass-spring-damper system, hence ignoring the contributions from the convolution integral, (2.57) simplifies to

$$[\boldsymbol{M} + \boldsymbol{A}(\omega)]\ddot{\boldsymbol{\xi}} + \boldsymbol{B}(\omega)\dot{\boldsymbol{\xi}} + \boldsymbol{C}\boldsymbol{\xi} = \boldsymbol{\tau}_{wave1} \tag{2.58}$$

This is the classical frequency-domain model. As it does not include the convolution integral, and thus fails to describe transient dynamics, it is emphasised that (2.58) is only valid:

1. Under linear theory
2. For harmonically forced oscillations

3. During steady-state response

This implies that the system must be analysed at a given frequency $\omega = \omega_n$, and the excitation force must be a (or a combination of many) sinusoidally varying forces. Superposition holds and $\boldsymbol{\tau}_{wave1}$ is

$$\boldsymbol{\tau}_{wave1} = \sum_{n=1}^{\infty} \boldsymbol{f} \cos(\omega_n t + \theta_n) \tag{2.59}$$

where $\boldsymbol{f} = \boldsymbol{F}_{wave1}(\omega)\zeta_a$ is the force amplitude. Expression (2.58) is in reality still a false time-domain model (Fossen [2011]). A more correct notation is found by taking the Fourier-transform

$$\left(-\omega^2[\boldsymbol{M} + \boldsymbol{A}(\omega)] - i\omega\boldsymbol{B}(\omega) + \boldsymbol{C}(\omega)\right)\boldsymbol{\xi}(i\omega) = \boldsymbol{\tau}_{wave1}(i\omega) \tag{2.60}$$

where all initial conditions are set to zero. The system response is found by

$$\boldsymbol{\xi}(i\omega) = \boldsymbol{H}(\omega)\boldsymbol{\tau}_{wave1}(i\omega) \tag{2.61}$$

where $\boldsymbol{H}$ is the system transfer-function defined as

$$\boldsymbol{H} = \left[-\omega^2[\boldsymbol{M} + \boldsymbol{A}(\omega)] - i\omega\boldsymbol{B}(\omega)\right]^{-1} \tag{2.62}$$

2.6.2 *Cummins*' equation

In finding a valid time-domain model, the system coefficients in (2.57) are assumed independent of frequency; $\boldsymbol{A}(\omega) = \hat{\boldsymbol{A}}$ and $\boldsymbol{B}(\omega) = \hat{\boldsymbol{B}}$. The result is time-domain model known as *Cummins*' equation

$$[\boldsymbol{M} + \hat{\boldsymbol{A}}]\ddot{\boldsymbol{\xi}} + \hat{\boldsymbol{B}}\dot{\boldsymbol{\xi}} + \int_{-\infty}^{t} \boldsymbol{K}(t-\tau)\dot{\boldsymbol{\xi}}(\tau)d\tau + \mathbf{C}\boldsymbol{\xi} = \boldsymbol{\tau}_{wave1} \tag{2.63}$$

Here, $\hat{\boldsymbol{A}}$, $\hat{\boldsymbol{B}}$ and $\boldsymbol{K}(t-\tau)$ are unknown.

2.6.3 *Ogilvie*'s transformation

Ogilvie [1964] presented a method in finding the unknown coefficients, by transforming the time-domain model to the frequency-domain, from (2.58).

If

$$\xi_j = \cos(\omega t) \tag{2.64}$$

then (2.63) becomes

$$-\omega^2[\boldsymbol{M} + \hat{\boldsymbol{A}}]\cos(\omega t) - \omega\hat{\boldsymbol{B}}\sin(\omega t) \tag{2.65}$$

$$-\,\omega \int\limits_{-\infty}^{t} \boldsymbol{K}(\tau)\sin(\omega t - \omega\tau)d\tau + \mathbf{C}\cos(\omega t) = \boldsymbol{\tau}_{wave1} \tag{2.66}$$

where a convolution identity is used

$$\int f(t-\tau)g(\tau) = \int f(\tau)g(t-\tau) \tag{2.67}$$

Using the trigonometric identity

$$\sin(\omega t - \omega\tau) = \sin(\omega t)\cos(\omega\tau) - \cos(\omega t)\sin(\omega\tau) \tag{2.68}$$

and rearranging

$$\begin{aligned} &-\omega^2\left[\boldsymbol{M} + \hat{\boldsymbol{A}} - \frac{1}{\omega}\int\limits_{-\infty}^{t} \boldsymbol{K}(\tau)\sin(\omega\tau)d\tau\right]\cos(\omega t) \\ &-\omega\left[\hat{\boldsymbol{B}} + \int\limits_{-\infty}^{t} \boldsymbol{K}(\tau)\cos(\omega\tau)d\tau\right]\sin(\omega t) + \boldsymbol{C}\cos(\omega t) = \boldsymbol{\tau}_{wave1} \end{aligned} \tag{2.69}$$

We wish to determine the retardation function and find the unknown variables of $\hat{\boldsymbol{A}}$ and $\hat{\boldsymbol{B}}$. This can be done by comparison to the coefficients of the frequency-domain model, which in turn are known from strip-theory. By introducing $\xi_j = \cos(\omega t)$ to the frequency-domain model in (2.58), the expression becomes

$$-\omega^2[\boldsymbol{M} + \boldsymbol{A}(\omega)]\cos(\omega t) - \omega\boldsymbol{B}(\omega)\sin(\omega t) + \boldsymbol{C}\cos(\omega t) = \boldsymbol{\tau}_{wave1} \tag{2.70}$$

By comparing the coefficients of (2.69) and (2.70) the result yields

$$\boldsymbol{A}(\omega) = \hat{\boldsymbol{A}} - \frac{1}{\omega}\int\limits_{-\infty}^{t} \boldsymbol{K}(\tau)\sin(\omega\tau)d\tau \tag{2.71}$$

$$\boldsymbol{B}(\omega) = \hat{\boldsymbol{B}} + \int\limits_{-\infty}^{t} \mathbf{K}(\tau)\cos(\omega\tau)d\tau \tag{2.72}$$

Equation (2.71) is valid for all ω, including the limit $\omega \to \infty$, so that

$$\lim_{\omega \to \infty} \boldsymbol{A}(\omega) = \boldsymbol{A}(\infty) = \hat{\boldsymbol{A}} \tag{2.73}$$

The impulse response function (retardation function) $\boldsymbol{K}(\tau)$ is of finite energy (Kristiansen and Egeland [2003]) and thus converges towards zero for infinite frequency. Thereby, we define

$$\hat{\boldsymbol{B}} = \boldsymbol{B}(\infty) \tag{2.74}$$

It follows that the retardation function, $\boldsymbol{K}(\tau)$ can be found by inverse Fourier transform of either (2.71) or (2.72)

$$\boldsymbol{K}(t) = -\int_0^\infty \omega[\boldsymbol{A}(\omega) - \boldsymbol{A}(\infty)] \sin(\omega t) d\omega \tag{2.75}$$

$$\boldsymbol{K}(t) = \int_0^\infty [\boldsymbol{B}(\omega) - \boldsymbol{B}(\infty)] \cos(\omega t) d\omega \tag{2.76}$$

which concludes the transformation.

2.6.4 Time-domain model

The time-domain equation of motion is formally known as

$$[\boldsymbol{M} + \boldsymbol{A}(\infty)]\ddot{\boldsymbol{\xi}} + \boldsymbol{B}(\infty)\dot{\boldsymbol{\xi}} + \int_0^t \boldsymbol{K}(t-\tau)\dot{\boldsymbol{\xi}}(\tau) d\tau + \boldsymbol{C}\boldsymbol{\xi} = \boldsymbol{\tau}_{wave1} \tag{2.77}$$

where the limit is changed due to causality (Fossen [2011]). The system coefficients are

$$\boldsymbol{A}(\omega) = \boldsymbol{A}(\infty) - \frac{1}{\omega}\int_0^t \boldsymbol{K}(\tau) \sin(\omega\tau) d\tau \tag{2.78}$$

$$\boldsymbol{B}(\omega) = \boldsymbol{B}(\infty) + \int_0^t \boldsymbol{K}(\tau) \cos(\omega\tau) d\tau \tag{2.79}$$

where $\boldsymbol{B}(\infty)$ can be proved to be zero (R. Taghipour and Moan [2008]), for zero speed. However, it is kept as a formality for later derivations.

2.6.5 State-space model

The convolution integral in (2.77) is “neither efficient for implementing numerical simulations nor convenient for control system analysis and design”(Perez and Fossen [2008]). As a result, Kristiansen and Egeland [2003] developed a state-space approximation to the convolution term in *Cummins*’ formula. The method was later improved and implemented by Perez and Fossen [2008]. The Laplace transform of the convolution integral is

$$\mathcal{L}\left\{\int_0^t \boldsymbol{K}(t-\tau)\dot{\boldsymbol{\xi}}(\tau)d\tau\right\} = s\boldsymbol{K}(s)\boldsymbol{\xi}(s) \tag{2.80}$$

It is evident that it can be approximated by a linear transfer-function $s\boldsymbol{K}(s)$.

A transfer-function is in practice a filter, contributing to what is known as fluid memory effects: adjustment in magnitude and phase-shift of the original signal (in this case $\boldsymbol{\xi}(s)$). Any transfer-function can be replaced by a state-space model and vice versa. Consequently, the state-space model for the convolution integral becomes (Perez and Fossen [2008])

$$\dot{\boldsymbol{x}} = \boldsymbol{A}_r\boldsymbol{x} + \boldsymbol{B}_r\dot{\boldsymbol{\xi}} \tag{2.81}$$

$$\boldsymbol{\mu} = \boldsymbol{C}_r\boldsymbol{x} \tag{2.82}$$

where

$$\boldsymbol{\mu}(s) = s\boldsymbol{K}(s)\boldsymbol{\xi} = \mathcal{L}\{\int_0^t \boldsymbol{K}(t-\tau)\dot{\boldsymbol{\xi}}(\tau)d\tau\} \tag{2.83}$$

and

$$\boldsymbol{K}(s) = \boldsymbol{C}_r(s\boldsymbol{I} - \boldsymbol{A}_r)^{-1}\boldsymbol{B}_r \tag{2.84}$$

$\boldsymbol{A}_r$, $\boldsymbol{B}_r$ and $\boldsymbol{C}_r$ are parameters of the model and are found by *Frequency-Domain Identification using the MSS FDI Toolbox for MATLAB* developed by *Perez* and *Fossen* (Fossen and Perez [2004]).

In determining $\boldsymbol{K}(s)$ we use the sine-cosine Fourier transform

$$K(i\omega) = \int_0^\infty \cos(\omega t)k(t) - i\int_0^\infty \sin(\omega t)k(t) \tag{2.85}$$

applied to (2.78) and (2.79), which gives

$$\boldsymbol{K}(i\omega) = [\boldsymbol{B}(\omega) - \boldsymbol{B}(\infty)] + i\omega[\boldsymbol{A}(\omega) - \boldsymbol{A}(\infty)] \tag{2.86}$$

In section 2.8.2, the derivation of $\boldsymbol{K}(i\omega)$ is exemplified.

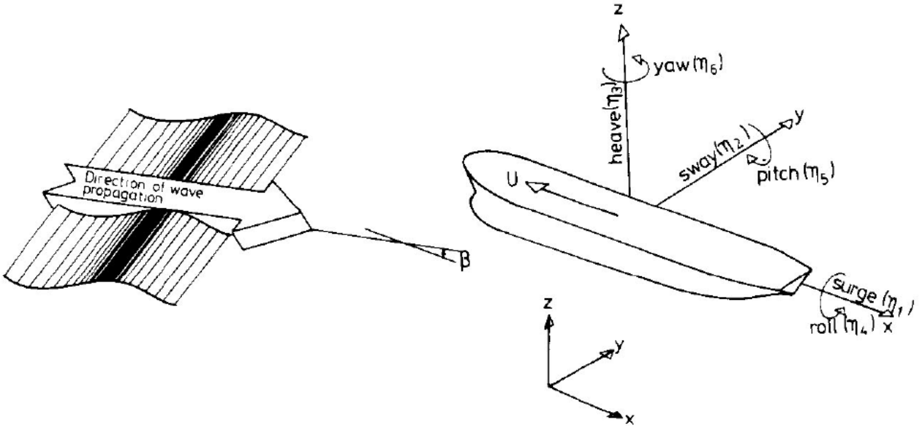

Figure 2.2: Orientation of coordinate system used by STF and VERES. Courtesy of Fathi [2010]

2.7 Forward speed effects

Equation (2.77) is given in the seakeeping frame (see figure 2.2). The seakeeping frame is inertial and follows the vessel with speed U, where the origin is placed at the vessel's equilibrium position. When the vessel is at speed, the hydrodynamic coefficients change.

Salvesen et al. [1970] (hereby, STF) have derived a method for finding the speed-dependent coefficients, by redefining the zero-speed boundary value problem to account for velocity.

Fossen [2011] presents an alternative approach, more suitable for time-domain implementation and control design. The method is based on an energy approach and identifies the speed-dependent terms by means of mere mechanical transformations between reference systems. Regardless, the method is still dependent on the zero-speed potential coefficients.

2.7.1 *Salvesen*, *Tuck* and *Faltinsen* 1970

Due to speed, the velocity potential is altered and forces due to radiation and excitation change. Let the new potential be referred to as

$$\phi = \phi_R + \phi_0 + \phi_D + Ux \tag{2.87}$$

where Ux is a steady flow along the horizontal axis (a simulation of forward speed as the vessel is held still). ϕ_R is the radiation potential while ϕ_0 and ϕ_D is the incident- and diffraction potential, accordingly, and make up the excitation potential. Using *Bernoulli's* equation from (2.8) in combination with (2.87), the pressure yields

$$p = -\rho(\frac{\partial}{\partial t} + U\frac{\partial}{\partial x})(\phi_R + \phi_0 + \phi_D) \tag{2.88}$$

Note that linear theory is still adopted; as a consequence all second-order terms are neglected. Additionally, the hydrostatic force has been omitted as it is safely modelled in the restoring force (2.13) (Salvesen et al. [1970]). In finding (2.88), we have used[1]

$$|\nabla\phi|^2 = |\nabla\phi_{U0}|^2 + 2U\frac{\partial\phi_{U0}}{\partial x} + U^2 \tag{2.89}$$

The first term in (2.88) is the dynamic pressure. The dynamic pressure is the source of the speed-independent added mass- and potential damping coefficients and force RAO's. All of which were identified and discussed in sections 2.3 and 2.4. The second term in (2.88), however, is the speed-dependent pressure that contribute in the equation of motion. The problem can again be broken into two; contributions from the radiation- and excitation potentials.

Radiation potential

In STF, the radiation term can be transformed by means of *Stoke*'s theorem into two, more easily digestible terms; one surface integral and one line-integral.

The surface integral appears due to the transformation from an inertial earth-fixed frame to the seakeeping coordinate system. This has been shown to be true by Fossen [2005], and will be discussed in the subsequent section. Secondly, the line-integral is what STF refers to as *end-terms*. From literature, *end-terms* are also known as transom-stern effects (Fossen [2011]) or hull-lift damping (Faltinsen [2005]). In his explanation of the hull-lift damping effect, *Faltinsen* compares the submerged part of the vessel to a low-aspect ratio lifting surface, where the trailing edge is at the transom stern. Such a lift-phenomena affect the equation of motion.

By using strip-theory, the forces due to the radiation potential can be found. These will give contributions to the added mass and potential damping, and we can say that

$$\boldsymbol{A}(\omega_e, U) = \boldsymbol{A}(\omega) + \boldsymbol{\alpha}(\omega_e, U) \tag{2.90}$$

$$\boldsymbol{B}(\omega_e, U) = \boldsymbol{B}(\omega) + \boldsymbol{\beta}(\omega_e, U) \tag{2.91}$$

where $\boldsymbol{A}(\omega)$ and $\boldsymbol{B}(\omega)$ are the zero-speed potential coefficients from section 2.3. $\boldsymbol{\alpha}(\omega_e, U)$ and $\boldsymbol{\beta}(\omega_e, U)$ are the additional speed-dependent coefficients derived by STF. ω_e is the encounter frequency and indicate a speed- and heading-dependency. The coefficients in heave and pitch are defined by Salvesen et al. [1970], as in table 2.2.

Motivated by table 2.2, we can redefine the parameters in a more systematic manner, on vector form. For notational simplicity we do not account for hull-lift damping, in this example.

$$\boldsymbol{A}(\omega_e, U) = \boldsymbol{A}(\omega_e) + \frac{U}{\omega_e^2}\begin{bmatrix} 0 & -B_{33}^0 \\ B_{33}^0 & A_{33}^0 \end{bmatrix} \tag{2.92}$$

$$\boldsymbol{B}(\omega_e, U) = \boldsymbol{B}(\omega_e) + U\begin{bmatrix} 0 & A_{33}^0 \\ -A_{33}^0 & \frac{U^2}{\omega_e^2}B_{33}^0 \end{bmatrix} \tag{2.93}$$

---

[1] As given in [Faltinsen, 2005, pg. 247]

A_{33}	$A^0_{33} - \frac{U}{\omega_e^2} b^A_{33}$
A_{35}	$A^0_{35} - \frac{U}{\omega_e^2} B^0_{33} + \frac{U}{\omega_e^2} x_A b^A_{33} - \frac{U^2}{\omega_e^2} a^A_{33}$
A_{53}	$A^0_{53} + \frac{U}{\omega_e^2} B^0_{33} - \frac{U^2}{\omega_e^2} x_A b^A_{33}$
A_{55}	$A^0_{55} + \frac{U^2}{\omega_e^2} A^0_{33} - \frac{U}{\omega_e^2} x_A^2 b^A_{33} + \frac{U^2}{\omega_e^2} x_A a^A_{33}$
B_{33}	$B^0_{33} + U a^A_{33}$
B_{35}	$B^0_{35} + U A^0_{33} - U x^A a^A_{33} + \frac{U^2}{\omega_e^2} b^A_{33}$
B_{53}	$B^0_{53} - U A^0_{33} - U x^A a^A_{33}$
B_{55}	$B^0_{55} + \frac{U^2}{\omega_e^2} B^0_{33} + U x_A^2 a^A_{33} + \frac{U^2}{\omega_e^2} x_A b^A_{33}$

Table 2.2: Heave- and pitch added mass and potential damping coefficients from STF-theory. The superscript '0' indicate zero-speed while 'A' distinguish the end-terms. x_A is the longitudinal distance from CO to stern and a_{ij}/b_{ij} is the two dimensional added mass/damping coefficient at x_A

Excitation potential

The diffraction potential, ϕ_D is found from the same principles as for the radiation potential. The force contributions from the incident potential ϕ_0, however, is more neatly analysed. From (2.37) the potential is

$$\phi_0 = \frac{g\zeta_a}{\omega} e^{kz} e^{ik(x\cos\beta + y\sin\beta)} e^{i\omega_e t} \tag{2.94}$$

and by applying it to (2.88), we get

$$\begin{aligned} p &= -\rho(\frac{\partial}{\partial t} + U\frac{\partial}{\partial x})\phi_0 & (2.95) \\ &= -\rho(i\omega + iUk\cos\beta)\phi_0 \to -\rho\omega_e\phi_0 & (2.96) \end{aligned}$$

where ω is the encounter frequency from (2.38). Furthermore, the pressure is integrated over the surface of the vessel and the speed-dependent forces due to waves can be found:

$$\boldsymbol{\tau}_{wave1} = \boldsymbol{F}_{wave1}(\omega, U, \beta)\zeta \tag{2.97}$$

As a concluding remark, hydrodynamic software like VERES implement the STF-theory and can determine: $\boldsymbol{A}(\omega_e, U)$, $\boldsymbol{B}(\omega_e, U)$ and $\boldsymbol{F}_{wave1}(\omega_e, U, \beta)$ for an arbitrary 3D-model. By knowing these parameters we can solve the frequency-domain model given as

$$[\boldsymbol{M} + \boldsymbol{A}(\omega_e, U)]\ddot{\boldsymbol{\xi}} + \boldsymbol{B}(\omega_e, U)\dot{\boldsymbol{\xi}} + \boldsymbol{C}\boldsymbol{\xi} = \boldsymbol{F}_{wave1}(\omega, U, \beta)\zeta \tag{2.98}$$

Alternatively, we can apply the parameters to the *Cummins* equation and time-domain model from (2.77). In that case we must remember that we have adopted an infinite frequency environment, which also must be imposed for the speed-dependent coefficients. Hence, most of the terms in table 2.2 actually vanish due to the singularities. For infinite frequency equation (2.92) develops to

$$\boldsymbol{A}(\infty, U) = \boldsymbol{A}(\omega) \tag{2.99}$$

$$\boldsymbol{B}(\infty, U) = \boldsymbol{B}(\omega) + UA_{33}^{0}\begin{bmatrix} 0 & 1 \\ -1 & 0 \end{bmatrix} \tag{2.100}$$

Here, it is made clear that the speed-dependent added mass for heave and pitch, at infinite frequency, is equal to that of zero-speed. This also applies to the remaining DOF which are not featured. The damping matrix is still dependent on speed.

2.7.2 Energy approach

An alternate approach can be derived using an energy approach and vectorial mechanics. This approach will give the same results as those derived by STF, as explicitly proven by Marshall et al. [1982]. Now, the energy approach is also the basis for Fossen [2011] marine ship motion theory. The idea of the energy approach, being a substitute for conventional potential theory, is highly interesting and a separate chapter will be devoted to the issue (see chapter 3).

The seakeeping frame is inertial, meaning it is non-accelerating (at constant speed) and fixed in orientation at the equilibrium position of the vessel. An inertial reference frame is not capable of describing the real accelerations acting on the vessel at forward speed in waves. On the contrary, a non-inertial, body-fixed reference system is free to translate and rotate with respect to an inertial, earth-fixed system, and is more suited to describe the motions of a vessel in 6 DOF. Additionally, the vessel excitation forces are derived from the fluid pressure at the hull, which is known to act normally to the orientation of the vessel, i.e in body-fixed coordinates. Figure 2.3 attempt to capture the concept visually.

Due to fact that a body-fixed coordinate system accelerate in space, fictitious forces appear. These forces are the main ingredient in the speed-dependent hydrodynamical coefficients in STF-theory, which we shall see in chapter 3.

2.8 System coefficients

The system coefficients are found by the ShipX Vessel Responses (VERES) software (Fathi [2010]) and the Frequency-domain identification (FDI) tool in the MSS toolbox for MATLAB (Fossen and Perez [2004]).

2.8.1 ShipX-VERES

VERES use strip-theory approximations according to section 2.3.2 and include forward speed effects as of the STF-method (see section 2.7.1). The software input is a 3D-model of the vessel, and relevant output span hydrodynamic coefficients and Response Amplitude Operator's (RAO's). Additionally, VERES allows the user to add appendices like foils.

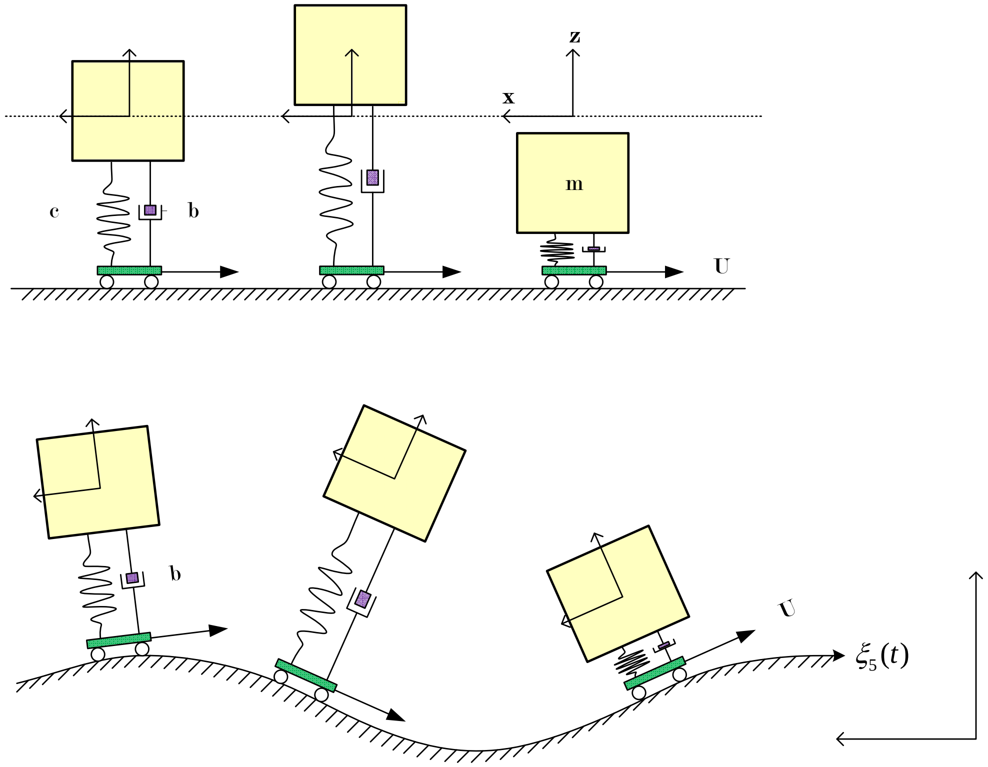

Figure 2.3: Example of different reference frames. Top: Inertial system with coordinate system in equilibrium and constant speed. Bottom: Non-inertial reference frame with accelerating body-fixed coordinate system. The coordinate system in the corner is inertial

Hydrodynamic coefficients

Output: $\boldsymbol{A}(\omega, U)$, $\boldsymbol{B}(\omega, U)$, $\boldsymbol{C}$
VERES output frequency-, heading- and speed-dependent added mass-, potential damping- and restoring coefficient matrices for all degrees of freedom (DOF). An example-curve for the coefficients is given in figures 2.4 and 2.5.

Force RAO's

Output: $\boldsymbol{F}(\omega, \beta, U)$
VERES create force RAO's, in a relevant range of frequencies, for all headings and speeds, in all DOF's. The force RAO's are independent of any appendices added to the model.

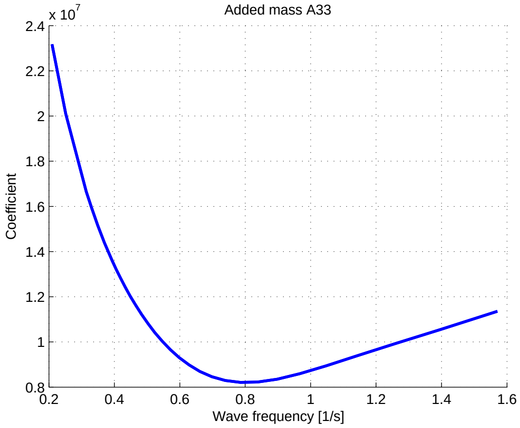

Figure 2.4: Added mass coefficient in {33} for zero speed

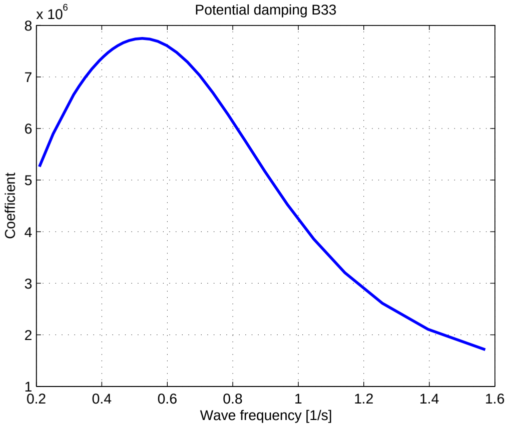

Figure 2.5: Potential damping coefficient in {33} for zero speed

Motion RAO's

Output: $\boldsymbol{H}(\omega, \beta, U)$
VERES set up the motion RAO's, in a relevant range of frequencies, for all headings and speeds, in all DOF's. The motion RAO's are dependent on the appendices added to the model, like foils, which means that the foil interaction will alter the vessel motion transfer-function.

The RAO can be found by Laplace transformation. Originally the model is:

$$[\boldsymbol{M} + \boldsymbol{A}(\omega_e, U)]\ddot{\boldsymbol{\xi}} + \boldsymbol{B}(\omega_e, U)\dot{\boldsymbol{\xi}} + \boldsymbol{C}\boldsymbol{\xi} = \boldsymbol{\tau} \tag{2.101}$$

and by transformation we get

$$\boldsymbol{\xi}(s) = [(\boldsymbol{M} + \boldsymbol{A}(\omega_e, U))s^2 + \boldsymbol{B}(\omega_e, U)s + \boldsymbol{C}]^{-1}\boldsymbol{\tau}\big|_{s=i\omega} \tag{2.102}$$

where

$$\boldsymbol{H}(\omega, U) = \frac{|\boldsymbol{\xi}(i\omega)|}{\zeta_a} \tag{2.103}$$

Added resistance

Output: $\boldsymbol{R}_{AW}(\omega, \beta, U)$
VERES calculates the speed- and heading dependent added resistance due to waves by using the Gerritsma & Beukelman method (see section 2.5).

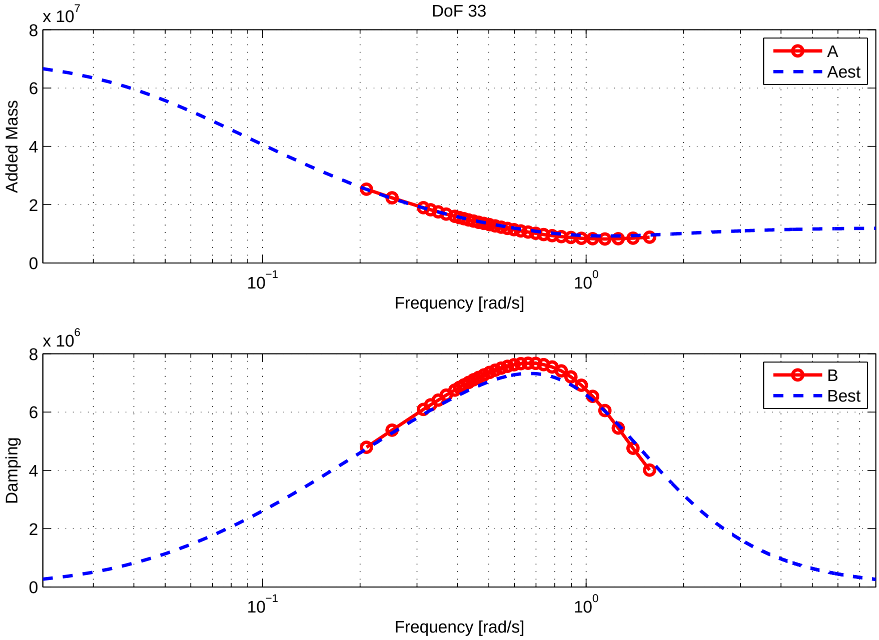

Figure 2.6: MSS fitted added mass- and damping coefficient for zero speed in dimension {33}

Calm water resistance

Output: $R_T(U)$
VERES estimate the total calm water resistance curves, by either the Holtrop-84- or Hollenbach-98 method.

Foil effects

Foils can be added manually in VERES. The output is additional added mass-, damping and restoring coefficient matrices and additional force RAO's. The vessel motion RAO will depend on the foil coefficients.

2.8.2 FDI MSS toolbox

The FDI tool implement the state-space theory from section 2.6. The tool use frequency-domain fitting to represent the zero-speed potential coefficients by transfer-functions. An example of the fitted curves is shown in figure 2.6. From the transfer-functions the infinite added mass can be identified. Furthermore, as $\boldsymbol{A}$, $\boldsymbol{B}$ and $\boldsymbol{A}(\infty)$ are determined, $\boldsymbol{K}(s)$ can be found, using equation (2.86), from section 2.6.5. $\boldsymbol{K}(s)$ and $\boldsymbol{A}(\infty)$ are key ingredients in the time-domain model.

Chapter 3

Unified Seakeeping and Maneuvering model

T. I. Fossen and T. Perez (Fossen [2011], Fossen [2005], Perez and Fossen[2008]) are among the only authors that address the problem of transforming motions between the seakeeping- and body-frame, in marine hydrodynamics. Their work provides an alternative to the Salvesen-Tuck-Faltinsen (STF) method in deriving speed-dependent hydrodynamic coefficients, better suited for time-domain simulations and thus control-design.

3.1 Preliminaries

3.1.1 Orientation

NED
North-East-Down oriented inertial and earth-fixed reference frame referred to as {n}. The origin is at o_n

Body-fixed
Rotating reference frame fixed at body. The frame is denoted {b} and the origin is at o_b

Seakeeping
Inertial reference frame travelling at constant speed with an origin that coincides with the equilibrium position of a {b}. The frame is assigned the abbreviation {s}

3.1.2 Notation

As of Fossen [2005] the generalised position, velocity and force vectors read

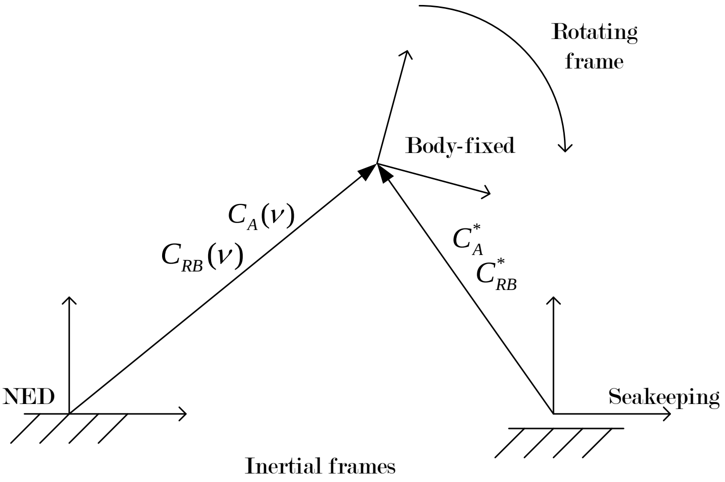
Rotating frame
Body-fixed
$C_A(\nu)$
$C_{RB}(\nu)$
C_A^*
C_{RB}^*
NED
Seakeeping
Inertial frames

Figure 3.1: Transformation between coordinate systems impute the forming of Coriolis and centripetal forces

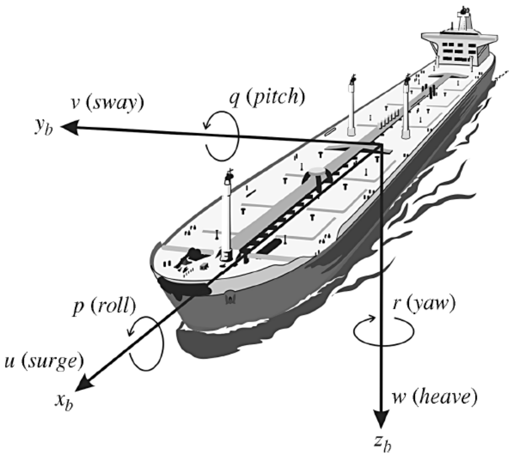
v (sway)
y_b
q (pitch)
p (roll)
u (surge)
x_b
r (yaw)
w (heave)
z_b

Figure 3.2: Convention for direction of ship motion velocities as used by Fossen. Figure from Fossen [2011]

$$\boldsymbol{\eta} = [n, e, d, \phi, \theta, \psi]^T \tag{3.1}$$

$$\boldsymbol{\nu} = [u, v, w, p, q, r]^T \tag{3.2}$$

$$\boldsymbol{\tau} = [X, Y, Z, K, M, N]^T \tag{3.3}$$

Here, $\boldsymbol{\eta}$ is the position in an inertial earth-fixed frame, which can be represented by the north-east-down position $\boldsymbol{p} = [n, e, d]^T$ and the Euler angles $\boldsymbol{\Theta} = [\phi, \theta, \psi]^T$, as follows

$$\boldsymbol{\eta} = [\boldsymbol{p}, \boldsymbol{\Theta}]^T \tag{3.4}$$

whereas, under the same convention, $\boldsymbol{\nu} = [\boldsymbol{v}, \boldsymbol{\omega}]^T$.

The seakeeping perturbation coordinates are defined relative to a constant speed inertial reference frame, according to

$$\boldsymbol{\xi} = [\xi_1, \xi_2, \xi_3, \xi_4, \xi_5, \xi_6]^T \tag{3.5}$$

where the velocity of the frame is assumed equal to $\nu_0 = [U, 0, 0, 0, 0, 0]^T$.

3.1.3 Coefficients

The mass matrix at CG take the following form

$$\boldsymbol{M} = \begin{bmatrix} m & 0 & 0 & 0 & 0 & 0 \\ 0 & m & 0 & 0 & 0 & 0 \\ 0 & 0 & m & 0 & 0 & 0 \\ 0 & 0 & 0 & I_x & -I_{xy} & -I_{xz} \\ 0 & 0 & 0 & -I_{yx} & I_y & -I_{yz} \\ 0 & 0 & 0 & -I_{zx} & -I_{zy} & I_z \end{bmatrix} \tag{3.6}$$

whereas the added mass coefficient is denoted

$$\boldsymbol{M}_A = \begin{bmatrix} A_{11} & A_{12} & A_{13} & A_{14} & A_{15} & A_{16} \\ A_{21} & A_{22} & A_{23} & A_{24} & A_{25} & A_{26} \\ A_{31} & A_{32} & A_{33} & A_{34} & A_{35} & A_{36} \\ A_{41} & A_{42} & A_{43} & A_{44} & A_{45} & A_{46} \\ A_{51} & A_{52} & A_{53} & A_{54} & A_{55} & A_{56} \\ A_{61} & A_{62} & A_{63} & A_{64} & A_{65} & A_{66} \end{bmatrix} \tag{3.7}$$

3.2 Rigid-body kinetics

Newton's second law about centre of gravity o_g in {n} yields

$$\boldsymbol{M}\frac{d}{dt}\dot{\boldsymbol{\eta}} = \boldsymbol{\tau} \tag{3.8}$$

where $\boldsymbol{\tau}$ is the external force.

3.2.1 Newton-Euler equations of motion

By means of Newtonian mechanics the inertial vectorial velocity $\boldsymbol{\eta}$ can be transferred to an arbitrary body-frame. From (3.8), it can be shown that the force acting on {b} is (Egeland and Gravdahl [2002] and appendix A)

$$\begin{aligned} m[\dot{\boldsymbol{v}}^b_{b/n} + \dot{\boldsymbol{\omega}}^b_{b/n} \times \boldsymbol{r}^b_g + 2\boldsymbol{\omega}^b_{b/n} \times \frac{d\boldsymbol{r_g}}{dt} \\ + \boldsymbol{\omega}^b_{b/n} \times \boldsymbol{v}^b_{b/n} + \boldsymbol{\omega}^b_{b/n} \times (\boldsymbol{\omega}^b_{b/n} \times \boldsymbol{r}^b_g)] = \boldsymbol{f}^b_b \end{aligned} \tag{3.9}$$

Here, $\boldsymbol{r}^b_g$ is the position-vector of an arbitrary point o_b, with respect to o_g, expressed in {b}. The sub- and superscripts define the system variables, according Fossen [2011]'s notational convention, as

$\boldsymbol{v}^b_{b/n}$	:	linear velocity of the point o_b with respect to {n} expressed in {b}
$\boldsymbol{\omega}^b_{b/n}$	:	angular velocity about the point o_b with respect to {n} expressed in {b}
$\boldsymbol{f}^b_b$	:	force with line of action through the point o_b expressed in {b}
$\boldsymbol{m}^b_b$	:	moment about o_b expressed in {b}

As $\boldsymbol{r}^b_g$ is of constant value the Coriolis-term with its time derivative vanishes. Consequently, the resulting force becomes

$$m[\dot{\boldsymbol{v}}^b_{b/n} + \dot{\boldsymbol{\omega}}^b_{b/n} \times \boldsymbol{r}^b_g + \boldsymbol{\omega}^b_{b/n} \times \boldsymbol{v}^b_{b/n} + \boldsymbol{\omega}^b_{b/n} \times (\boldsymbol{\omega}^b_{b/n} \times \boldsymbol{r}^b_g)] = \boldsymbol{f}^b_b \tag{3.10}$$

By similar derivations the moment about o_b can be shown to be

$$\boldsymbol{I}_b\dot{\boldsymbol{\omega}}^b_{b/n} + \boldsymbol{\omega}^b_{b/n} \times \boldsymbol{I}_b\boldsymbol{\omega}^b_{b/n} + m\boldsymbol{r}^b_g \times (\dot{\boldsymbol{v}}^b_{b/n} + \boldsymbol{\omega}^b_{b/n} \times \boldsymbol{v}^b_{b/n}) = \boldsymbol{m}^b_b \tag{3.11}$$

where $\boldsymbol{I}_g$ is the system inertia matrix about o_g.

A matrix-representation of equation (3.10) and (3.11) yields (Fossen [2011])

$$\boldsymbol{M}_{RB}\dot{\nu} + \boldsymbol{C}_{RB}\boldsymbol{\nu} = \boldsymbol{\tau} \tag{3.12}$$

where

$$\boldsymbol{M}_{RB} = \begin{bmatrix} m\boldsymbol{I}_{3\times 3} & -m\boldsymbol{S}(\boldsymbol{r}_g^b) \\ m\boldsymbol{S}(\boldsymbol{r}_g^b) & \boldsymbol{I}_g - m\boldsymbol{S}^2(\boldsymbol{r}_g^b) \end{bmatrix} \tag{3.13}$$

$$\boldsymbol{C}_{RB} = \begin{bmatrix} m\boldsymbol{S}(\boldsymbol{\omega}_{b/n}^b) & -m\boldsymbol{S}(\boldsymbol{\omega}_{b/n}^b)\boldsymbol{S}(\boldsymbol{r}_g^b) \\ m\boldsymbol{S}(\boldsymbol{\omega}_{b/n}^b)\boldsymbol{S}(\boldsymbol{r}_g^b) & -\boldsymbol{S}((\boldsymbol{I}_g - m\boldsymbol{S}^2(\boldsymbol{r}_g^b))\boldsymbol{\omega}_{b/n}^b) \end{bmatrix} \tag{3.14}$$

In the above, $\boldsymbol{S}()$ is the cross-product operator defined by

$$\boldsymbol{S}(\boldsymbol{\lambda})\boldsymbol{a} = \boldsymbol{\lambda} \times \boldsymbol{a} \tag{3.15}$$

and the identity $\boldsymbol{I}_b = \boldsymbol{I}_g - m\boldsymbol{S}^2(\boldsymbol{r}_g^b)$ is used (Egeland and Gravdahl [2002]).

(3.12) is the non-linear rigid-body Coriolis and centripetal matrix. Basically, it represent the forces that are concerned with rotations of a body about an inertial reference frame; the forces felt by the body as it is accelerated arbitrarily in a domain. For comparison reasons, we are going to need this matrix in the following sections to conclude our proof.

In VERES, it is custom to calculate the hydrodynamic forces through and about a point in the waterline, within the same cross-section as o_g. Hence $\boldsymbol{r}_g^b = [0, 0, z_g]$. On component form in 3 DOF (surge,heave and pitch), we have (Fossen [2011])

$$\boldsymbol{C}_{RB}(\boldsymbol{\nu}) = \begin{bmatrix} 0 & 0 & mw \\ 0 & 0 & -m(z_g q + u) \\ -mw & m(z_g q + u) & 0 \end{bmatrix} \tag{3.16}$$

The Coriolis matrices are not unique and can be rearranged. In (3.16) we see that the term $\boldsymbol{C}_{RB}^{[61]}$ and $\boldsymbol{C}_{RB}^{[63]}$ cancel when multiplying out $\boldsymbol{C}_{RB}(\boldsymbol{\nu})\boldsymbol{\nu}$. Thereby,

$$\boldsymbol{C}_{RB}(\boldsymbol{\nu}) = \begin{bmatrix} 0 & 0 & mw \\ 0 & 0 & -m(z_g q + u) \\ 0 & mz_g q & 0 \end{bmatrix} \tag{3.17}$$

The linear equivalent of (3.17) about $\boldsymbol{\nu} = \boldsymbol{\nu}_0 = [U, 0, 0, 0, 0, 0]^T$ can be denoted

$$\boldsymbol{C}_{RB}^{*}(\boldsymbol{\nu}) = \begin{bmatrix} 0 & 0 & 0 \\ 0 & 0 & -mu \\ 0 & 0 & 0 \end{bmatrix} = \boldsymbol{MLU} \tag{3.18}$$

as mwq is negligible under linear theory, because w and q are perturbations about $\boldsymbol{\nu}_0$. In the above

$$\boldsymbol{L} = \begin{bmatrix} 0 & 0 & 0 \\ 0 & 0 & -1 \\ 0 & 0 & 0 \end{bmatrix} \tag{3.19}$$

3.2.2 *Kirchhoff's* equations

In the previous section C_{RB} was identified using the *Newton-Euler* equations of motions. An alternate approach utilising the principles of Lagrangian mechanics is presented by Marshall et al. [1982] and Fossen [2011]. The *Euler-Lagrange* equation is based on an energy method, where the dynamics of a system can be found by ensuring that the equations are satisfied. Furthermore, *Kirchhoff* derived an energy formulation better suited for fluid dynamics (Fossen [2011]), which will be applied in the following.

Kirchhoff's equations are given

$$\frac{d}{dt}\left(\frac{\partial T}{\partial \boldsymbol{v}}\right) = \frac{\partial T}{\partial \boldsymbol{\omega}} \times \boldsymbol{\omega} + \boldsymbol{f} \tag{3.20}$$

$$\frac{d}{dt}\left(\frac{\partial T}{\partial \boldsymbol{\omega}}\right) = \frac{\partial T}{\partial \boldsymbol{\omega}} \times \boldsymbol{\omega} + \frac{\partial T}{\partial \boldsymbol{v}} \times \boldsymbol{v} + \boldsymbol{m} \tag{3.21}$$

For notational convenience $\boldsymbol{v} = \boldsymbol{v}_{b/n}^{b}$ and $\boldsymbol{\omega} = \boldsymbol{\omega}_{b/n}^{b}$ when using *Kirchhoff's* method. As, $\boldsymbol{\lambda} \times \boldsymbol{a} = -\boldsymbol{a} \times \boldsymbol{\lambda}$ and by using the identity in (3.15) we obtain

$$\frac{d}{dt}\left(\frac{\partial T}{\partial \boldsymbol{v}}\right) + \boldsymbol{S}(\boldsymbol{\omega})\frac{\partial T}{\partial \boldsymbol{\omega}} = \boldsymbol{f} \tag{3.22}$$

$$\frac{d}{dt}\left(\frac{\partial T}{\partial \boldsymbol{\omega}}\right) + \boldsymbol{S}(\boldsymbol{\omega})\frac{\partial T}{\partial \boldsymbol{\omega}} + \boldsymbol{S}(\boldsymbol{v})\frac{\partial T}{\partial \boldsymbol{v}} = \boldsymbol{m} \tag{3.23}$$

where the kinetic energy, T, of the rigid-body can be written in a quadratic form as

$$T = \frac{1}{2}\boldsymbol{\nu}^T \boldsymbol{M}\boldsymbol{\nu} \tag{3.24}$$

whereas $\boldsymbol{M} = \boldsymbol{M}_{RB}$ and

$$\boldsymbol{M} = \begin{bmatrix} \boldsymbol{M}_{11} & \boldsymbol{M}_{12} \\ \boldsymbol{M}_{21} & \boldsymbol{M}_{22} \end{bmatrix} \tag{3.25}$$

By using the same procedure as presented in Fossen [2011], the kinetic energy can be expanded

$$T = \frac{1}{2}(\boldsymbol{v}^T \boldsymbol{M}_{11}\boldsymbol{v} + \boldsymbol{v}^T \boldsymbol{M}_{12}\boldsymbol{\omega} + \boldsymbol{\omega}^T \boldsymbol{M}_{21}\boldsymbol{v} + \boldsymbol{\omega}^T \boldsymbol{M}_{22}\boldsymbol{\omega}) \tag{3.26}$$

Due to symmetry in $\boldsymbol{M}$, $\boldsymbol{M}_{12} = \boldsymbol{M}_{21}^T$ and $\boldsymbol{M}_{21} = \boldsymbol{M}_{12}^T$. By applying matrix calculus, the energy derivatives in (3.22) becomes

$$\frac{\partial T}{\partial \boldsymbol{v}} = \boldsymbol{M}_{11}\boldsymbol{v} + \boldsymbol{M}_{12}\boldsymbol{\omega} \tag{3.27}$$

$$\frac{\partial T}{\partial \boldsymbol{\omega}} = \boldsymbol{M}_{21}\boldsymbol{v} + \boldsymbol{M}_{22}\boldsymbol{\omega} \tag{3.28}$$

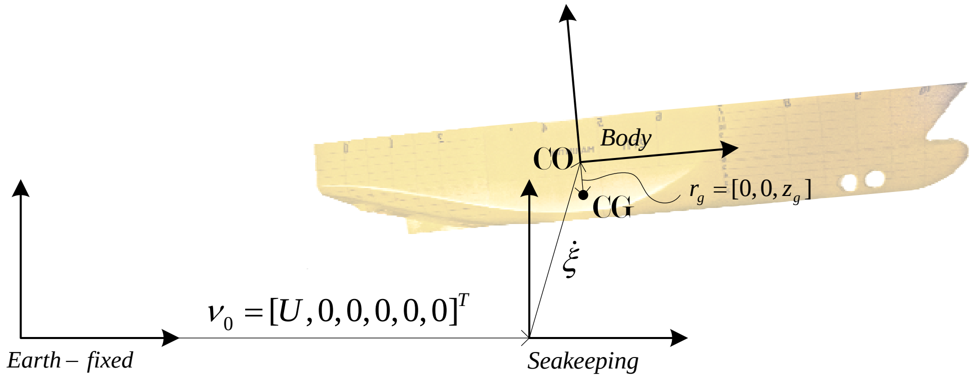

Figure 3.3: Reference coordinate systems: Earth-fixed, seakeeping and body-fixed, and the relation between them

Equation (3.22) can be reformulated to represent the standard form $\boldsymbol{M}_{RB}\dot{\boldsymbol{\nu}} + \boldsymbol{C}_{RB}(\boldsymbol{\nu})\boldsymbol{\nu} = \boldsymbol{\tau}$:

$$\boldsymbol{M}_{RB}\dot{\boldsymbol{\nu}} + \underbrace{\begin{bmatrix} \boldsymbol{S}(\boldsymbol{\omega})\frac{\partial T}{\partial \boldsymbol{v}} \\ \boldsymbol{S}(\boldsymbol{\omega})\frac{\partial T}{\partial \boldsymbol{\omega}} + \boldsymbol{S}(\boldsymbol{v})\frac{\partial T}{\partial \boldsymbol{v}} \end{bmatrix}}_{\boldsymbol{C}_{RB}(\boldsymbol{\nu})\boldsymbol{\nu}} = \boldsymbol{\tau} \tag{3.29}$$

where $\boldsymbol{C}_{RB}(\boldsymbol{\nu}$ can be shown to be (Fossen [2011])

$$\boldsymbol{C}_{RB}(\boldsymbol{\nu}) = \begin{bmatrix} \boldsymbol{0}_{3\times3} & -\boldsymbol{S}(\frac{\partial T}{d\boldsymbol{v}}) \\ -\boldsymbol{S}(\frac{\partial T}{d\boldsymbol{v}}) & -\boldsymbol{S}(\frac{\partial T}{d\boldsymbol{\omega}}) \end{bmatrix} \tag{3.30}$$

which for $\boldsymbol{M} = \boldsymbol{M}_{RB}$, and by imposing the skew-symmetric property of the Coriolis matrix, can be written as (Fossen [2011])

$$\boldsymbol{C}_{RB}(\boldsymbol{\nu}) = \begin{bmatrix} m\boldsymbol{S}(\boldsymbol{\omega}^b_{b/n}) & -m\boldsymbol{S}(\boldsymbol{\omega}^b_{b/n})m\boldsymbol{S}(\boldsymbol{r}^b_g) \\ -m\boldsymbol{S}(\boldsymbol{\omega}^b_{b/n})m\boldsymbol{S}(\boldsymbol{r}^b_g) & -\boldsymbol{S}(\boldsymbol{I}_b\boldsymbol{\omega}^b_{b/n}) \end{bmatrix} \tag{3.31}$$

The Coriolis term found by using the energy method is evidently similar to that of *Newton-Euler* from (3.14), thus the procedure is a solid alternative. This will prove useful when deriving the Coriolis term due to added mass.

3.3 Seakeeping- to body frame

3.3.1 Kinematics

Both the {n}-frame and the {s}-frame are inertial reference frames, and simple superposition of velocities is valid. Transferring the earth-fixed velocity, $\dot{\boldsymbol{\eta}}$, to the seakeeping velocity, $\dot{\boldsymbol{\xi}}$, yields

$$\dot{\boldsymbol{\eta}} = \boldsymbol{\nu}_0 + \dot{\boldsymbol{\xi}} = \begin{bmatrix} U + \dot{\xi}_1 \\ \dot{\xi}_2 \\ \dot{\xi}_3 \\ \dot{\xi}_4 \\ \dot{\xi}_5 \\ \dot{\xi}_6 \end{bmatrix} \tag{3.32}$$

As for the {b}-frame, the velocities, $\boldsymbol{\nu}$, can be linearised about $\boldsymbol{\nu}_0 = [U, 0, 0, 0, 0, 0]^T$. This gives

$$\boldsymbol{\nu} = \boldsymbol{\nu}_0 + \begin{bmatrix} \delta u \\ \delta v \\ \delta w \\ \delta p \\ \delta q \\ \delta r \end{bmatrix} = \begin{bmatrix} U + \delta u \\ \delta v \\ \delta w \\ \delta p \\ \delta q \\ \delta r \end{bmatrix} \tag{3.33}$$

The {b}-frame angular velocities, $\boldsymbol{\omega}^b_{b/n} = [\delta p, \delta q, \delta r]^T$ are given relative to the inertial axes, which implies that

$$\begin{bmatrix} \dot{\xi}_4 \\ \dot{\xi}_5 \\ \dot{\xi}_6 \end{bmatrix} = \begin{bmatrix} \delta p \\ \delta q \\ \delta r \end{bmatrix} \tag{3.34}$$

Assuming small angles, the kinematic transformation between {b} and {s} for the linear velocity, can be shown to be (see appendix A).

$$\dot{\boldsymbol{\eta}}_{1,2,3} = \boldsymbol{v}^b_{b/n} + \boldsymbol{\xi}_{4,5,6} \times \boldsymbol{v}^b_{b/n} + \boldsymbol{\omega}_{b/n} \times \boldsymbol{r}^b_g \tag{3.35}$$

In finding $[\xi_1, \xi_2, \xi_3]^T$, we apply (3.35). Neglecting higher order terms and using the fact that $\dot{\boldsymbol{\eta}}_{1,2,3} = [U + \delta u, \delta v, \delta w]^T$ and $\boldsymbol{r}_g = [0, 0, z_g]^T$, we get

$$\begin{bmatrix} U + \dot{\xi}_1 \\ \dot{\xi}_2 \\ \dot{\xi}_3 \end{bmatrix} = \begin{bmatrix} U + \delta u + z_g \delta q \\ \delta v + (U + \delta u)\xi_6 - z_g \delta p \\ \delta w - (U + \delta u)\xi_5 \end{bmatrix} \tag{3.36}$$

Let $U >> \delta u$ and $U + \delta u \rightarrow U$ and simplify

$$\begin{bmatrix} \dot{\xi}_1 \\ \dot{\xi}_2 \\ \dot{\xi}_3 \end{bmatrix} = \begin{bmatrix} \delta u + z_g \delta q \\ \delta v + U\xi_6 - z_g \delta p \\ \delta w - U\xi_5 \end{bmatrix} \tag{3.37}$$

The accelerations yield

$$\ddot{\boldsymbol{\xi}} = \begin{bmatrix} \delta\dot{u} + z_g\delta\dot{q} \\ \delta\dot{v} + U\delta r - z_g\delta\dot{p} \\ \delta\dot{w} - U\delta q \\ \dot{\delta p} \\ \dot{\delta q} \\ \dot{\delta r} \end{bmatrix} \tag{3.38}$$

which equivalently can be derived by linearising the acceleration terms from (3.10), about $\boldsymbol{\nu}_0$. Let ξ_5 and ξ_6 be

$$\xi_5 = \xi_{5a}\cos(\omega_e t) \rightarrow \ddot{\xi}_5 = -\omega_e^2\xi_{5a}\cos(\omega_e t) \tag{3.39}$$

$$\xi_6 = \xi_{6a}\cos(\omega_e t) \rightarrow \ddot{\xi}_6 = -\omega_e^2\xi_{6a}\cos(\omega_e t) \tag{3.40}$$

and hence

$$\xi_5 = -\frac{1}{\omega_e^2}\ddot{\xi}_5 \qquad\qquad \xi_6 = -\frac{1}{\omega_e^2}\ddot{\xi}_6 \tag{3.41}$$

Using the above result the velocity becomes

$$\dot{\boldsymbol{\xi}} = \begin{bmatrix} \delta u + z_g\delta q \\ \delta v - U\frac{1}{\omega_e^2}\delta\dot{r} - z_g\delta p \\ \delta w + U\frac{1}{\omega_e^2}\delta\dot{q} \\ \delta p \\ \delta q \\ \delta r \end{bmatrix} \tag{3.42}$$

The velocity (3.42) and the acceleration (3.38) can be written in compact form, as of Fossen [2005]

$$\dot{\boldsymbol{\xi}} = \mathbf{J}\delta\boldsymbol{\nu} - \frac{U}{\omega_e^2}\mathbf{L}\delta\dot{\boldsymbol{\nu}} \tag{3.43}$$

$$\ddot{\boldsymbol{\xi}} = \mathbf{J}\delta\dot{\boldsymbol{\nu}} + U\mathbf{L}\delta\boldsymbol{\nu} \tag{3.44}$$

where $\delta\boldsymbol{\nu} = [\delta u, \delta v, \delta w, \delta p, \delta q, \delta r]^T$ and

$$\mathbf{J} = \begin{bmatrix} 1 & 0 & 0 & 0 & z_g & 0 \\ 0 & 1 & 0 & -z_g & 0 & 0 \\ 0 & 0 & 1 & 0 & 0 & 0 \\ 0 & 0 & 0 & 1 & 0 & 0 \\ 0 & 0 & 0 & 0 & 1 & 0 \\ 0 & 0 & 0 & 0 & 0 & 1 \end{bmatrix} \qquad \mathbf{L} = \begin{bmatrix} 0 & 0 & 0 & 0 & 0 & 0 \\ 0 & 0 & 0 & 0 & 0 & 1 \\ 0 & 0 & 0 & 0 & -1 & 0 \\ 0 & 0 & 0 & 0 & 0 & 0 \\ 0 & 0 & 0 & 0 & 0 & 0 \\ 0 & 0 & 0 & 0 & 0 & 0 \end{bmatrix} \tag{3.45}$$

As $\delta\boldsymbol{\nu} = \boldsymbol{\nu} - \boldsymbol{\nu}_0$ (see equation (3.33)), and therefore $\delta\dot{\boldsymbol{\nu}} = \dot{\boldsymbol{\nu}}$, (3.43) and (3.44) can be written

$$\dot{\boldsymbol{\xi}} = \mathbf{J}\boldsymbol{\nu} - \frac{U}{\omega_e^2}\mathbf{L}\dot{\boldsymbol{\nu}} - \mathbf{J}\boldsymbol{\nu}_0 \tag{3.46}$$

$$\ddot{\boldsymbol{\xi}} = \mathbf{J}\dot{\boldsymbol{\nu}} + U\mathbf{L}\boldsymbol{\nu} - \cancelto{0}{U\mathbf{L}\boldsymbol{\nu}_0} \tag{3.47}$$

where the last term in (3.47) is zero, and the last term in (3.46) is a constant offset, equal to $\boldsymbol{\nu}_0$. Such an offset can be regarded as constant force when introduced in the equation of motion, which we will see.

As an example of the methods validity, so far, we consider a vessel at zero speed, and again, *Newton's* second law. In addition, we demand symmetry by mathematically introducing $\mathbf{J}^T$:

$$(\mathbf{J}^T\boldsymbol{M}^*\mathbf{J})\dot{\boldsymbol{\nu}} = \mathbf{J}^T\boldsymbol{\tau}^* \rightarrow \boldsymbol{M}_{RB}\dot{\boldsymbol{\nu}} = \boldsymbol{\tau} \tag{3.48}$$

Here, $\boldsymbol{M}_{RB}$ will be identical to the generalised mass matrix derived by STF (Salvesen et al. [1970]) and the $\boldsymbol{M}_{RB}$ from (3.13). Additionally, (3.19) and (3.45) are identical, which they should be.

3.3.2 Kinetics

The time-domain model from section 2.6.4 is

$$[\boldsymbol{M}_{RB} + \boldsymbol{A}(\infty)]\ddot{\boldsymbol{\xi}} + \boldsymbol{B}(\infty)\dot{\boldsymbol{\xi}} + \int_0^t \boldsymbol{K}(t-\tau)\dot{\boldsymbol{\xi}}(\tau)d\tau + \boldsymbol{C}\boldsymbol{\xi} = \boldsymbol{\tau} \tag{3.49}$$

Setting, $\mathbf{J} = \mathbf{I}$ to ease the example, introducing (3.46) and (3.47), the above expression yields

$$\begin{aligned}
&[\boldsymbol{M}_{RB} + \boldsymbol{A}(\infty)](\dot{\boldsymbol{\nu}} + U\mathbf{L}\boldsymbol{\nu}) + \boldsymbol{B}(\infty)(\boldsymbol{\nu} - \frac{U}{\omega_e^2}\mathbf{L}\dot{\boldsymbol{\nu}} - \boldsymbol{\nu}_0) \\
&\qquad + \int_0^t \boldsymbol{K}(t-\tau)(\boldsymbol{\nu} - \frac{U}{\omega_e^2}\mathbf{L}\dot{\boldsymbol{\nu}} - \boldsymbol{\nu}_0)d\tau + \boldsymbol{C}\boldsymbol{\xi} = \boldsymbol{\tau}_{wave1}
\end{aligned} \tag{3.50}$$

(3.49) is analysed at $\omega_e \rightarrow \infty$ and the $\frac{1}{\omega_e^2}$-terms vanish. By re-structuring, the expression reads

$$[\boldsymbol{M}_{RB} + \boldsymbol{M}_A(\infty)]\dot{\boldsymbol{\nu}} + \boldsymbol{C}_{RB}^*\boldsymbol{\nu} + \boldsymbol{C}_A^*\boldsymbol{\nu} + \boldsymbol{B}(\infty)\boldsymbol{\nu} + \boldsymbol{\mu} + \boldsymbol{C}\boldsymbol{\xi} = \boldsymbol{\tau} + \boldsymbol{\tau}_{\boldsymbol{\nu}_0} \tag{3.51}$$

where

$$\boldsymbol{M}_A(\infty) = \boldsymbol{A}(\infty) \tag{3.52}$$

$$\boldsymbol{C}^*_{RB} = U\boldsymbol{M}_{RB}\mathbf{L} \tag{3.53}$$

$$\boldsymbol{C}^*_{A} = U\boldsymbol{A}(\infty)\mathbf{L} \tag{3.54}$$

$$\boldsymbol{\mu} = \int\limits_0^t \boldsymbol{K}(t-\tau)(\boldsymbol{\nu}(\tau) - \boldsymbol{\nu}_0)d\tau \tag{3.55}$$

$$\boldsymbol{\tau}_{\boldsymbol{\nu}_0} = \boldsymbol{\nu}_0\boldsymbol{B}(\infty) \tag{3.56}$$

$\boldsymbol{C}_{RB}*$ and $\boldsymbol{C}_A*$ are the linearised Coriolis-centripetal coefficients, where $\boldsymbol{C}_{RB}*$ is consistent with expression (3.18). $\boldsymbol{\tau}_{\boldsymbol{\nu}_0}$ is the linearised constant damping force in surge due to forward speed. It can be interpreted as the vessel resistance due to manoeuvring.

In 3 DOF $\boldsymbol{C}^*_A$ is

$$\boldsymbol{C}^*_A = U\begin{bmatrix} 0 & 0 & -A_{13} \\ 0 & 0 & -A_{33} \\ 0 & 0 & -A_{53} \end{bmatrix} \tag{3.57}$$

3.4 Energy approach

Motivated by the fact that we were able to define the $\boldsymbol{C}_{RB}$ from conservation of energy of $\boldsymbol{M}_{RB}$, we wish to include the added mass term $\boldsymbol{M}_A$ in a similar manner.

Applying the same methodology as described in section 3.2.2, we expect the Coriolis term due to added mass $\boldsymbol{C}_A$ to take the form

$$\boldsymbol{C}_A(\boldsymbol{\nu}) = \begin{bmatrix} \mathbf{0}_{3\times 3} & -\boldsymbol{S}(\frac{\partial T}{d\boldsymbol{v}}) \\ -\boldsymbol{S}(\frac{\partial T}{d\boldsymbol{v}}) & -\boldsymbol{S}(\frac{\partial T}{d\boldsymbol{\omega}}) \end{bmatrix} \tag{3.58}$$

where

$$\frac{\partial T}{\partial \boldsymbol{v}} = \boldsymbol{M}_{11}\boldsymbol{v} + \boldsymbol{M}_{12}\boldsymbol{\omega} \tag{3.59}$$

$$\frac{\partial T}{\partial \boldsymbol{\omega}} = \boldsymbol{M}_{21}\boldsymbol{v} + \boldsymbol{M}_{22}\boldsymbol{\omega} \tag{3.60}$$

and this time $\boldsymbol{M} = \boldsymbol{M}_A$ defined by

$$\boldsymbol{M}_A = \begin{bmatrix} \boldsymbol{M}_{11} & \boldsymbol{M}_{12} \\ \boldsymbol{M}_{21} & \boldsymbol{M}_{22} \end{bmatrix} \tag{3.61}$$

On component form, the solution in 3 DOF yields (Fossen [2011])

$$\boldsymbol{C}_A(\boldsymbol{\nu}) = \begin{bmatrix} 0 & 0 & a_3 \\ 0 & 0 & -a_1 \\ -a_3 & a_1 & 0 \end{bmatrix} \tag{3.62}$$

where

$$a_1 = A_{11}u + A_{13}w + A_{15}q \tag{3.63}$$

$$a_3 = A_{31}u + A_{33}w + A_{35}q \tag{3.64}$$

The equation of motion, due to rotation of the added mass in {b} about {n}, now is

$$\boldsymbol{M}_A\dot{\boldsymbol{\nu}} + \boldsymbol{C}_A\boldsymbol{\nu} = \boldsymbol{\tau} \tag{3.65}$$

3.5 Comparing to STF

STF is based on solving a boundary value problem under potential theory. Meanwhile, the energy approach is based on defining the dynamics of a system by keeping track of the energy balance. VERES and other hydrodynamical programs use STF as a basis for their computation of the speed-dependent terms in the system matrices; added mass, potential damping and restoring. However, when reviewing the STF it is somewhat unclear how the forces appear and what really causes them. A more flexible and transparent procedure is the energy approach.

The classical frequency-domain formulation is given as

$$[\boldsymbol{M} + \boldsymbol{A}(\omega_e, U)]\ddot{\boldsymbol{\xi}} + \boldsymbol{B}(\omega_e, U)\dot{\boldsymbol{\xi}} + \boldsymbol{C}\boldsymbol{\xi} = \boldsymbol{\tau}_{wave1} \tag{3.66}$$

where $\boldsymbol{A}(\omega_e, U)$ and $\boldsymbol{B}(\omega_e, U)$ are speed-dependent added mass and damping coefficients found from STF-theory by for instance VERES (see expression (2.99)). As we are using the *Cummins* equation, the coefficients are to be evaluated at infinite frequency.

In deriving the STF coefficients by the energy approach, we will start in the {n}-frame and work ourselves into seakeeping coordinates by the transformations presented in the previous sections.

In {n}, we have

$$(\boldsymbol{M} + \boldsymbol{M}_A)\frac{d}{dt}\dot{\boldsymbol{\eta}} = \boldsymbol{\tau} \tag{3.67}$$

The transformation to {b}, is found from (3.65) and (3.12), and is

$$(\boldsymbol{M}_{RB} + \boldsymbol{M}_A)\dot{\boldsymbol{\nu}} + \boldsymbol{C}_{RB}\boldsymbol{\nu} + \boldsymbol{C}_A\boldsymbol{\nu} = \boldsymbol{\tau} \tag{3.68}$$

The transformation matrices between {s} and {b} is given in (3.46) and (3.47). $\boldsymbol{\nu}$ and $\dot{\boldsymbol{\nu}}$ can thus be expressed by seakeeping coordinates in the following manner

$$\mathbf{J}\boldsymbol{\nu} = \dot{\boldsymbol{\xi}} + \frac{U}{\omega_e^2}\mathbf{L}\dot{\boldsymbol{\nu}} + \mathbf{J}\boldsymbol{\nu}_0 \tag{3.69}$$

$$\mathbf{J}\dot{\boldsymbol{\nu}} = \ddot{\boldsymbol{\xi}} - U\mathbf{L}\boldsymbol{\nu} \tag{3.70}$$

For infinite frequency, setting $\mathbf{J} = \mathbf{I}$ for the purpose of the example and ignoring $\boldsymbol{\nu}_0$ for the moment, the transformation reads

$$\boldsymbol{\nu} = \dot{\boldsymbol{\xi}} \tag{3.71}$$

$$\dot{\boldsymbol{\nu}} = \ddot{\boldsymbol{\xi}} - U\mathbf{L}\boldsymbol{\nu} \tag{3.72}$$

Introducing the above to (3.68), the expression reads

$$(\boldsymbol{M}_{RB} + \boldsymbol{M}_A)\ddot{\boldsymbol{\xi}} - U\boldsymbol{M}_{RB}\boldsymbol{L}\dot{\boldsymbol{\xi}} - U\boldsymbol{M}_A\boldsymbol{L}\dot{\boldsymbol{\xi}} + \boldsymbol{C}_{RB}(\boldsymbol{\nu})\dot{\boldsymbol{\xi}} + \boldsymbol{C}_A\boldsymbol{\nu}\dot{\boldsymbol{\xi}} = \boldsymbol{\tau} \tag{3.73}$$

Simplifying,

$$(\boldsymbol{M}_{RB} + \boldsymbol{M}_A)\ddot{\boldsymbol{\xi}} + \underbrace{(\boldsymbol{C}_{RB}(\boldsymbol{\nu}) - \boldsymbol{C}^*_{RB})}_{\boldsymbol{C}_{RB}^{VERES}}\dot{\boldsymbol{\xi}} + \underbrace{(\boldsymbol{C}_A(\boldsymbol{\nu}) - \boldsymbol{C}^*_A)}_{\boldsymbol{C}_A^{VERES}}\dot{\boldsymbol{\xi}} = \boldsymbol{\tau} \tag{3.74}$$

where the added mass Coriolis and centripetal term is given as

$$\boldsymbol{C}^*_A = U\begin{bmatrix} 0 & 0 & 0 \\ 0 & 0 & -A_{33} \\ 0 & 0 & -A_{53} \end{bmatrix} \tag{3.75}$$

$$\boldsymbol{C}_A(\boldsymbol{\nu}) = \begin{bmatrix} 0 & 0 & A_{33}w + A_{53}q \\ 0 & 0 & -A_{11}u \\ -A_{33}w - A_{53}q & +A_{11}u & 0 \end{bmatrix} \tag{3.76}$$

$$\approx U\begin{bmatrix} 0 & 0 & 0 \\ 0 & 0 & -A_{11} \\ 0 & A_{11} - A_{33} & -A_{53} \end{bmatrix} \tag{3.77}$$

where $A_{13} = A_{15} = 0$, $A_{35} = A_{53}$, $u = U$ and $(A_{33}w + A_{53}q) = O(e^2)$ is a second-order perturbation term. The sum $\boldsymbol{C}_A^{VERES} = \boldsymbol{C}_A(\boldsymbol{\nu}) - \boldsymbol{C}^*_A$ is recognised as

$$\boldsymbol{C}_A^{VERES} = U\begin{bmatrix} 0 & 0 & 0 \\ 0 & 0 & A_{33} - A_{11} \\ 0 & A_{11} - A_{33} & 0 \end{bmatrix} \tag{3.78}$$

VERES neglect the effect of A_{11} and by that it is made evident that the coefficient matches the speed-dependent terms of the STF-formulation perfectly, in an infinite frequency environment. It is stressed that VERES' axes (x backwards, y port and z upwards) are defined differently than those of Fossen [2011] (see section 3.1.1). The transformation satisfies

$\boldsymbol{A}_{Fossen} = \boldsymbol{T}\boldsymbol{A}_{VERES}\boldsymbol{T}$, where $\boldsymbol{T} = \mathrm{diag}\{-1, 1, -1, -1, 1, -1\}$. The same goes for $\boldsymbol{B}$. Note that also U changes direction.

The rigid-body Coriolis terms are

$$\boldsymbol{C}_{RB}(\boldsymbol{\nu}) = \begin{bmatrix} 0 & 0 & mw \\ 0 & 0 & -m(z_g q + u) \\ 0 & m z_g q & 0 \end{bmatrix} \qquad \boldsymbol{C}^*_{RB}(\boldsymbol{\nu}) = \begin{bmatrix} 0 & 0 & 0 \\ 0 & 0 & -mu \\ 0 & 0 & 0 \end{bmatrix} \tag{3.79}$$

hence, by neglecting second-order terms $\boldsymbol{C}_{RB}^{VERES} = \boldsymbol{C}_{RB}(\boldsymbol{\nu}) - \boldsymbol{C}^*_{RB}$ the sum satisfies

$$\boldsymbol{C}_{RB}^{VERES} = \boldsymbol{0} \tag{3.80}$$

It is made clear that the rigid-body terms have no immediate impact on the speed-dependent seakeeping coefficients, in accordance with STF.

The speed-dependent, linear expression at $\omega = \infty$ reads

$$(\boldsymbol{M}_{RB} + \boldsymbol{M}_A)\ddot{\boldsymbol{\xi}} + \boldsymbol{C}_A^{VERES}\dot{\boldsymbol{\xi}} = \boldsymbol{\tau} \tag{3.81}$$

Formulation (3.81) clearly states that, the speed-dependent terms within STF-theory are solely caused by a mechanical transformation between the inertial earth-fixed frame and the seakeeping frame (except for hull-lift damping). Consequently, frequency dependent terms can be added to the solution without considering the effects of speed; that is the fluid-memory- and infinite damping term in *Cummins*' equation.

Kirchhoff's equation does not consider gravitational forces, and these must thus be included separately.

From *Cummins*' equation, valid formulations are:

In the seakeeping-frame:

$$(\boldsymbol{M}_{RB} + \boldsymbol{M}_A(\infty))\ddot{\boldsymbol{\xi}} + \boldsymbol{C}_A^{VERES}\dot{\boldsymbol{\xi}} + \boldsymbol{B}(\infty)\dot{\boldsymbol{\xi}} + \int_0^t \boldsymbol{K}(t-\tau)\dot{\boldsymbol{\xi}}(\tau)d\tau + \boldsymbol{C}\boldsymbol{\xi} = \boldsymbol{\tau} \tag{3.82}$$

In the body-fixed-frame:

$$(\boldsymbol{M}_{RB} + \boldsymbol{M}_A(\infty))\dot{\boldsymbol{\nu}} + \boldsymbol{C}_{RB}(\boldsymbol{\nu})\boldsymbol{\nu} + \boldsymbol{C}_A(\boldsymbol{\nu})\boldsymbol{\nu} + \boldsymbol{B}(\infty)\boldsymbol{\nu} + \boldsymbol{\mu} + \boldsymbol{C}\boldsymbol{\xi} = \boldsymbol{\tau} \tag{3.83}$$

where

$$\boldsymbol{M}_A(\infty) = \boldsymbol{A}(\infty) \tag{3.84}$$

$$\boldsymbol{C}_A^{VERES} = \boldsymbol{C}_A(\boldsymbol{\nu}_{\boldsymbol{\nu}_0}) - \boldsymbol{C}_A^* \tag{3.85}$$

$$\boldsymbol{\mu} = \int_0^t \boldsymbol{K}(t-\tau)(\boldsymbol{\nu}(\tau) - \boldsymbol{\nu}_0)d\tau \tag{3.86}$$

$\boldsymbol{C}_A(\boldsymbol{\nu})$ and $\boldsymbol{C}_A(\boldsymbol{\nu})$ are the non-linear Coriolis and centripetal matrices, due to rotation of {b} around {n}, while $\boldsymbol{C}_A(\boldsymbol{\nu}_{\boldsymbol{\nu}_0})$ is the linear counterpart. $\boldsymbol{C}_A^*$ is the linear Coriolis term due to rotation of {b} about {s}.

VERES' potential coefficients at infinite frequency can thereby be reformulated to

$$\boldsymbol{A}(\infty, U) = \boldsymbol{A}(\infty, 0) = \boldsymbol{M}_A(\infty) \tag{3.87}$$

$$\boldsymbol{B}(\infty, U) = \boldsymbol{B}(\infty, 0) + \boldsymbol{C}_A^{VERES}(\infty) \tag{3.88}$$

The result is highly intriguing, as the user can apply 2D-potential, strip-theory for zero speed to a unified seakeeping- and manoeuvring problem (at forward speed). As a curiosity, the frequency dependent added mass coefficient is made superfluous in the above models. The speed-dependent coefficients outputted from VERES are numerically unstable for low frequency as the $\frac{1}{\omega_e}$-terms are difficult to interpret and physically abnormal. This problem is circumvented by using the energy-approach and *Cummins*' equation. It must be noted that the frequency-dependent hull-lift damping terms (see section 2.7.1) are neglected using the unified model.

Furthermore, it is also possible to utilise 3D potential theory programs, like WAMIT, for the analysis of the equations of motion.

3.6 Verification

As a verification of the method, frequency response in heave and pitch is compared with the response from the time-domain, unified model. The response from the time-domain model is extracted by finding the standard deviation of the response from the time-series. The standard deviation is related to response amplitude by $\xi_a = \sqrt{2}\sigma$. The results for heave and pitch are illustrated in figures 3.4-3.9. The results from a model test using the same model is also used in the comparison.

The frequency-domain model and the time-domain model coincide well for high and low frequencies. The pitch angle is underestimated, and as the pitch and heave angles are coupled within $\boldsymbol{C}_A^{VERES}$ the result is affected in heave response as well. This issue will have to be looked into. At slow forward speed, the results correlate well.

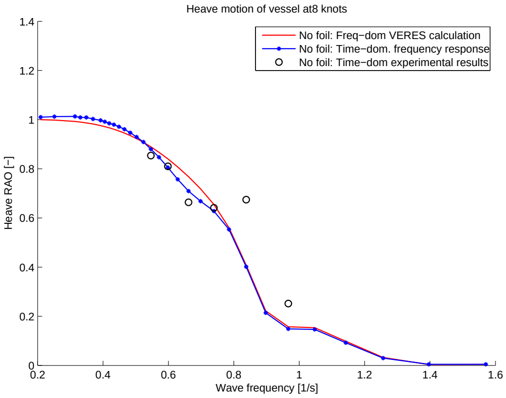

Figure 3.4: Frequency response of UT-751 supply vessel at 8 knots in heave

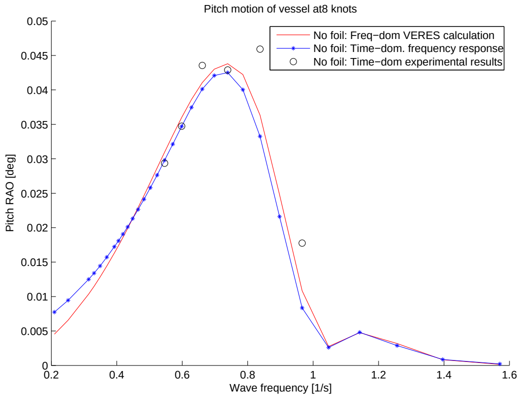

Figure 3.5: Frequency response of UT-751 supply vessel at 8 knots in pitch

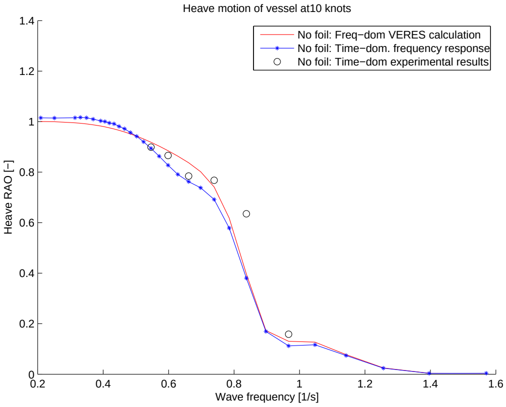

Figure 3.6: Frequency response of UT-751 supply vessel at 10 knots in heave

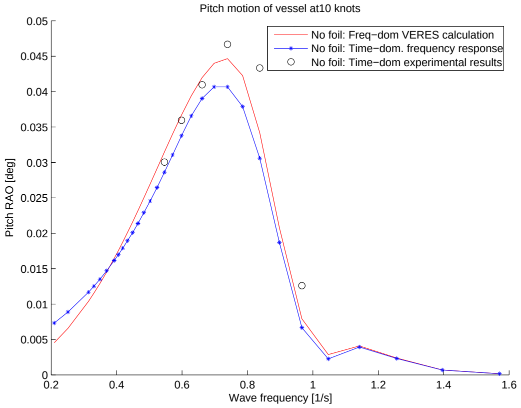

Figure 3.7: Frequency response of UT-751 supply vessel at 10 knots in pitch

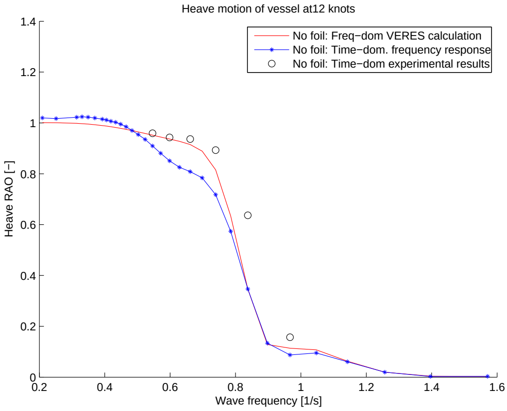

Figure 3.8: Frequency response of UT-751 supply vessel at 12 knots in heave

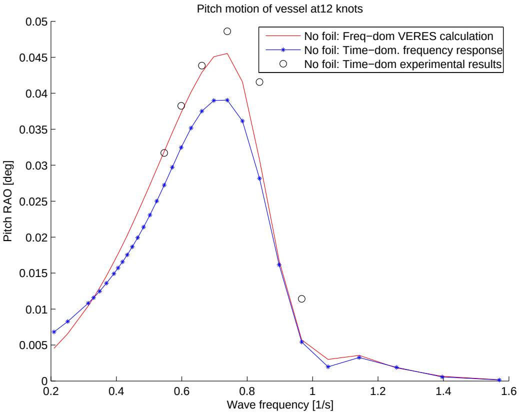

Figure 3.9: Frequency response of UT-751 supply vessel at 12 knots in pitch

Chapter 4

Foil Model

4.1 Foil theory

Expressions for lift and drag on a foil can readily be derived from potential theory and by using the assumption of conservation of fluid momentum (see section 2.1)(Newman [1977], Faltinsen [2005]).

A lift force is caused by circulation around a foil. In fluid dynamics, circulation is related to fluid velocity by the following

$$\Gamma = \oint_C \mathbf{u} \cdot d\mathbf{s} \tag{4.1}$$

where $\mathbf{s}$ is a finite length along the path of the closed curve C. Now, letting $d\mathbf{s} = \mathbf{r} d\theta$ and integrating, circulation can be expressed in terms of *Biot-Savarts* law

$$\Gamma = 2\pi \boldsymbol{r} u(\boldsymbol{r}) \tag{4.2}$$

where r is the radius of integration. *Biot-Savarts* law indicates that circulation is equivalent to induced velocity circulating the foil. The induced velocity causes a relative speed difference between the upper- and lower foil surface. By *Bernoullis* equation for 2D steady flow, a speed difference over a thin foil sets up a pressure-field[1].

$$\Delta p = \frac{\rho}{2}\left[(U + u(r))^2 - (U - u(r))^2\right] = 2\rho U u(r) \tag{4.3}$$

where $\boldsymbol{r} = r$ and $\rho g z = 0$ due to the 1D nature of the foil. Figure 4.1 illustrates the effect. The total lifting force can thus be expressed as

---

[1] As described in Steen [2007]

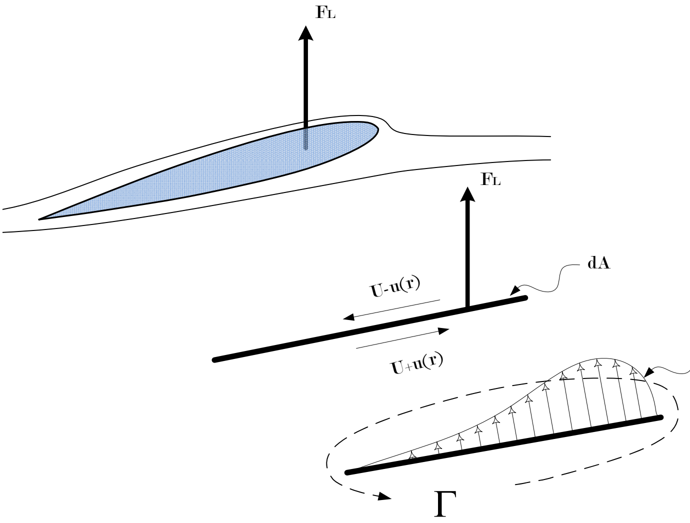

Figure 4.1: Illustration of the concept of circulation and induced velocity of a foil at an angle. Top: Foil at an angle with surrounding fluid streamlines. Middle: Induced velocity. Bottom: Induced pressure-field and circulation

$$F_L = \int \Delta p dl = \oint_C \frac{\Delta p}{2} ds \tag{4.4}$$

$$= \rho U \Gamma \tag{4.5}$$

where (4.1) and (4.3) is used. Expression (4.4) is known as the Kutta-Joukowski theorem. An important consequence of potential theory is that, the circulation around a closed curve C circumpassing the fluid domain must remain constant, according to *Kelvin's* Theorem (Newman [1977]):

$$\frac{d\Gamma_C}{dt} = 0 \tag{4.6}$$

The fact that the total circulation in a fluid remains constant is vital for the understanding of unsteady flow characteristics.

4.1.1 Quasi-static lifting theory

It is common to express the lifting force (and drag) as a function of a dimensionless coefficient, where the coefficient is the ratio between the actual force and kinetic force in the undisturbed flow-field,

$$C_L = \frac{F_L}{0.5 \rho U^2 S} \tag{4.7}$$

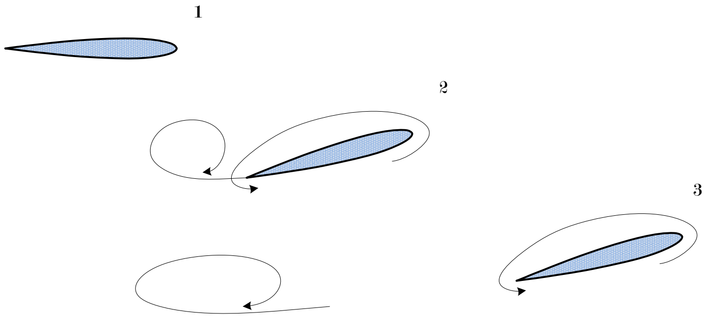

Figure 4.2: Visualisation of the implication of unsteady flow on an airfoil. 1: No angle of attack and no lift. 2: Instantaneous change in angle of attack and the onset of circulation and *vortex-shedding*. 3: Steady-state flow and circulation

where C_L is the lift coefficient, F_L the lift force, U the undisturbed velocity and S the foil surface area.

For a 2D steady flow in infinite fluid, over a flat plate, it can be shown (Faltinsen [2005]) that the circulation is $\Gamma = Uc\pi\alpha$. Here, α is the foil angle of attack and c is the cord. By Kutta-Joukowskis theorem (from (4.4)), the dimensionless lift coefficient yields

$$C_L = \frac{F_L}{0.5\rho U^2 c} = 2\pi\alpha \tag{4.8}$$

$C_L = 2\pi\alpha$ is known as the ideal lift coefficient. *Prandtl's* lifting line theory makes adjustments for 3D effects and C_L becomes

$$C_L = \frac{2\pi\alpha}{(1 + 2/\Lambda)} \tag{4.9}$$

where $\Lambda = s^2/sc$ is the foil aspect ratio and s the span. *Prandtl's* theory gives good indication of 3D effects for high aspect ratio's (Faltinsen [2005]) and approaches the ideal lift coefficient as $\Lambda \to \infty$. Other effects such as free-surface- and strut interaction, might be included for improved results.

When *Prandtl's* lifting line theory is applied to problems including a time-dependent angle of attack ($\alpha(t)$), we call it quasi-static foil theory. Such theory describes unsteady flow by steady-state principles, which might be a blunt assumption.

4.1.2 Unsteady lifting theory

Theodorsen [1935] studied the implications of unsteady flow on an airfoil. He derived what is known as the *Theodorsen* function.

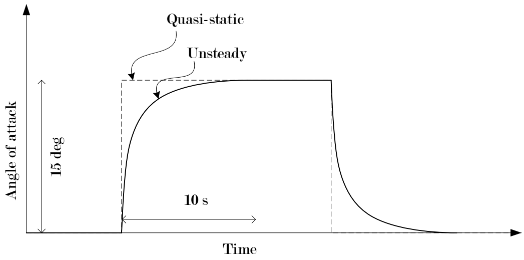

Figure 4.3: Effective angle of attack on an airfoil according to quasi-static- and unsteady lifting theory. For an impulse response ($\omega \to \infty$) the unsteady angle of attack is at a phase with respect to the quasi-static angle

Let us study a foil that is subjected to an instantaneous change in angle of attack, as visualised in figure 4.3. Firstly, we define effective angle of attack as the angle 'felt' by the foil (what is meant by 'felt' will be discussed shortly). As a result, lift forces are estimated adopting the effective angle of attack. Under quasi-static theory the effective angle of attack is equivalent to the theoretical. Hence, the lift will be calculated based on the instantaneous step-functioned angle from figure 4.3. However, a step-functioned lifting force is un-physical and therefore subject to inaccuracies, when applied to mathematical models. Furthermore, *Theodorsen* claimed that the effective angle acting on the foil could be represented by a *filtered* equivalent of the instantaneous angle of attack. The filter is *Theodorsen*'s function. The characteristics of unsteady flow can be understood from the following reasoning and figure 4.2.

Let a change in angle of attack inflict the circulation Γ_{foil}. As the total circulation in the fluid must remain constant, according to *Kelvin's* theorem from (4.6), there must exist a circulation $\Gamma_0 = -\Gamma_{foil}$ within the fluid. Γ_0 is a tip-vortex created at the trailing-edge due to the change in angle of attack. The tip-vortex Γ_0 induces velocity as of *Biot Savart's* law from (4.2), and the velocity in vertical direction reduces the effective, or 'felt', angle of attack on the foil. As the flow becomes steady the distance between Γ_{foil} and Γ_0 increase and the induced velocity decrease inverse-proportionally as of (4.2).

Theodorsen function ($C(k_f)$) is given by

$$C(k_f) = \frac{H_1^{(2)}(k_f)}{H_1^{(2)}(k_f) + iH_0^{(2)}(k_f)} \tag{4.10}$$

where $H_n^{(2)}(k_f)$ are Hankel functions (Faltinsen [2005]), that is

$$H_n^{(2)}(k_f) = J_n - iY_n \tag{4.11}$$

Here, J_n and Y_n are the Bessel functions of first and second kind, respectively. k_f is the reduced frequency, made dimensionless by the cord c and the velocity U, and defined as

$$k_f = \frac{w_e c}{2U} \tag{4.12}$$

(4.10) is plotted in figure 4.2, for a range of frequencies that is relevant for later analysis (within spectral boundaries, as periods range $4 - 30$ seconds).

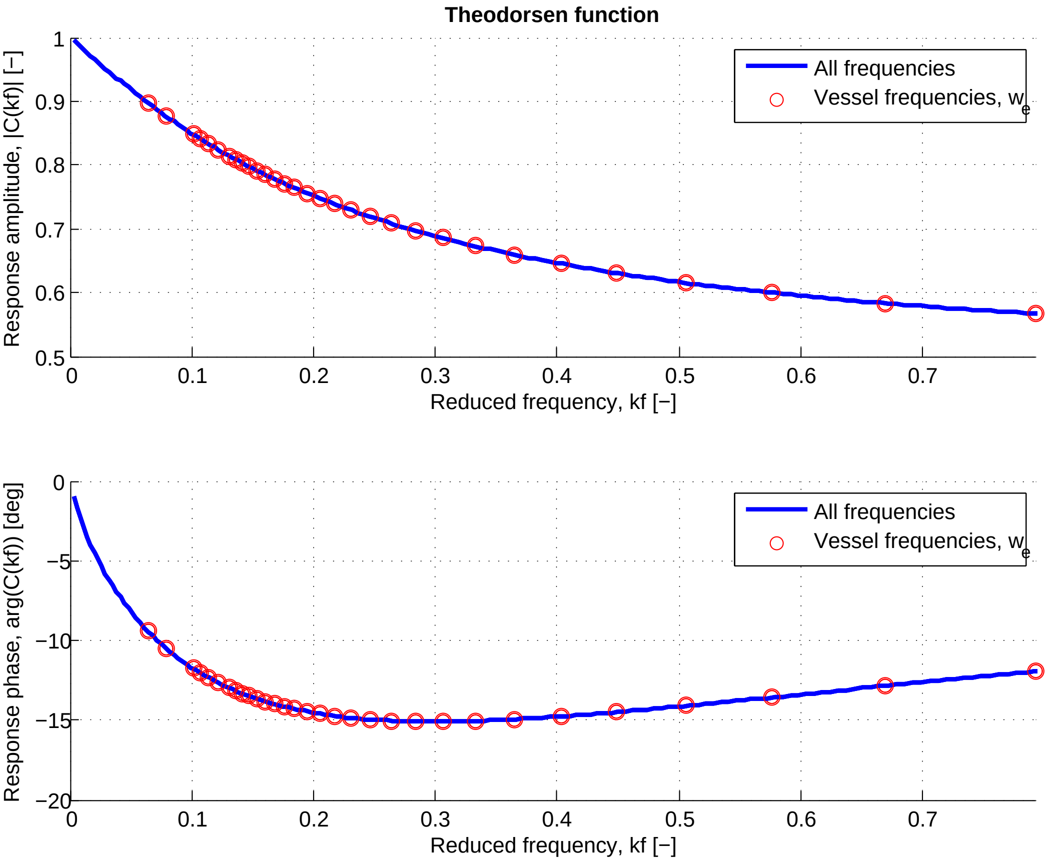

Figure 4.4: Theodorsen function for relevant reduced frequencies. The 'vessel frequencies', ω_e, range from $0.2 - 1.6$, which cooresponds to periods in the range of $4 - 30$ seconds

Frequency-domain fitting of Theodorsen's function

Theodorsen's function is useful when doing analysis in the frequency-domain, however it is difficult to implement when operating in the time-domain. Motivated by this, the author has designed a filter representing the characteristics of the *Theodorsen* function which is suitable for time-domain simulation. A MATLAB-function take in the complex *Theodorsen* response from (4.10), for a range of frequencies, and output the numerator and denominator of a least-square fitted transfer-function. For the least-square fitting, a built-in MATLAB-function is utilised (*invfreqs.m*). The stability of the transfer-function is checked and the approximation plotted. Figure 4.5 illustrate that the approximation is in good compliance with the actual function, hence the technique will be used in the simulations.

4.1.3 Drag

$\frac{\rho}{2}|\nabla\phi|^2$ in *Bernoulli's* equation is the basis for calculating the drag forces, either by direct integration over the projected area in the direction of the fluid flow or by using *Kutta-Joukowski's*

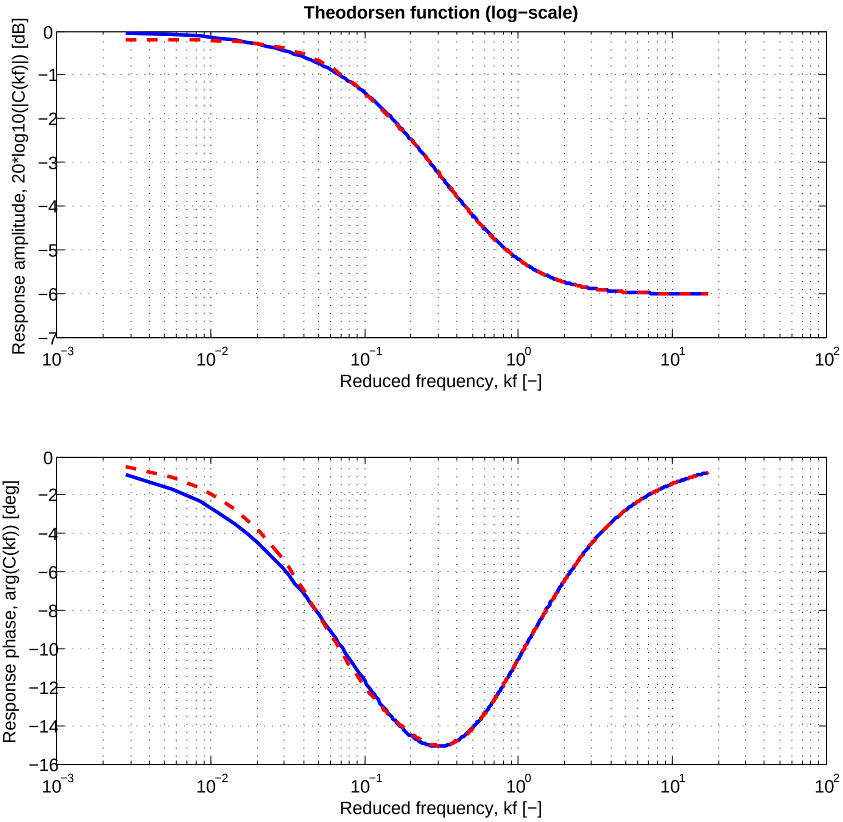

Figure 4.5: Theodorsen approximation function in dotted red vs the actual Theodorsen response in blue

formula (which is based on *Bernoulli's* equation)(Faltinsen [2005]). The drag force is defined in the same dimensionless manner as the lift force

$$C_D = \frac{D}{0.5\rho U^2 S} \tag{4.13}$$

and the drag coefficient is found to be

$$C_D = \frac{4\pi\alpha^2\Lambda}{(\Lambda+2)^2} = \frac{C_L^2}{\pi\Lambda} \tag{4.14}$$

The drag coefficient is a function of the lift coefficient, and for that reason it is often called induced drag. Additionally, viscous drag should be accounted for. This effect will be considered by using experimental results from model tests.

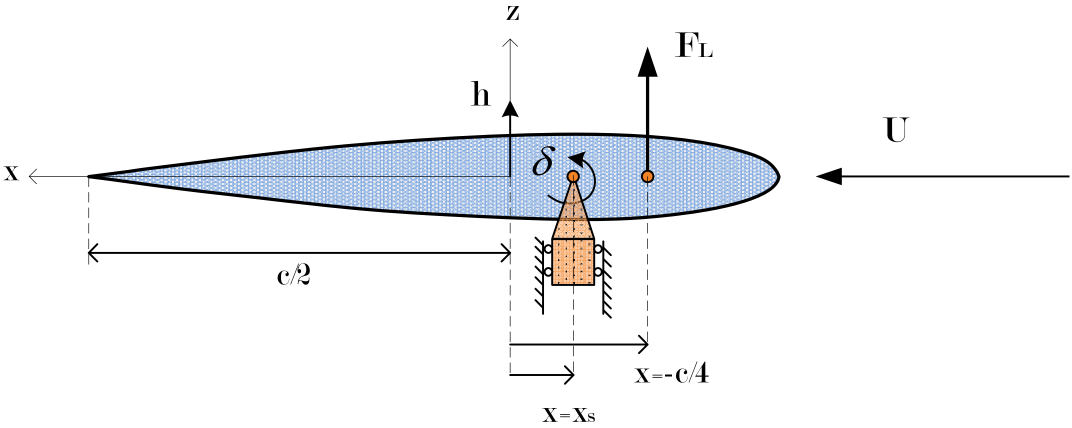

Figure 4.6: Oscillating foil in steady flow with velocity U. The foil is free to move vertically (h) and to rotate about its own suspension (δ)

4.2 Oscillating foil

The vertical velocity of the foil for an arbitrary point x, can be expressed as

$$\dot{\eta}_3 = \dot{h} - (x - x_s)\dot{\delta} - U\delta \tag{4.15}$$

where h is forced vertical displacement amid cord, and δ is the rotation about the position of the foil suspension x_s. U is the incident velocity parallel to the x-axis.

4.2.1 Circulatory forces

The lift force is a circulatory force. The resulting lift force acts through the centre of pressure, which can be expected to lie at approximately $x = -c/4$. From quasi-static theory, the instantaneous angle of attack is

$$\alpha = -\arctan\left(\frac{\dot{\eta}_3}{U}\right) \approx -\frac{\dot{\eta}_3}{U}\bigg|_{x=-c/4} \tag{4.16}$$

whereas the ambient fluid velocity over the foil is

$$V = \sqrt{\dot{\eta}_3^2 + U^2} \approx U \tag{4.17}$$

Both (4.16) and (4.17) can be linearised when $U >> \dot{\eta}_3$. Thereby, the linear, 2D unsteady lift force yields

$$\begin{aligned} f_L &= \underbrace{0.5\rho U^2 c\frac{2\pi}{(1+2/\Lambda)}C(k_f)}_{\frac{df_L}{d\alpha}}\,\alpha \\ &= -\frac{df_L}{d\alpha}\frac{1}{U}(\dot{h} - (-\frac{c}{4} - x_s)\dot{\delta} - U\delta) \end{aligned} \tag{4.18}$$

4.2.2 Non-circulatory forces

Added mass forces are a non-circulatory. The added mass force for a flat plate is found by

$$f_A = -a_{33}\ddot{\eta}_3 = -\rho\pi(\frac{c}{2})^2\ddot{\eta}_3\Big|_{x=0} \tag{4.19}$$

where $-\ddot{\eta}_3|_{x=0}$ is the acceleration at the foil centre, given by

$$\ddot{\eta}_3 = \ddot{h} - (-x_s)\ddot{\delta} - U\dot{\delta}\Big|_{x=0} \tag{4.20}$$

and $a_{33} = \rho\pi(\frac{c}{2})^2$ is the added mass coefficient.

4.2.3 Forces on oscillating foil

Assuming linear theory and the foil to be a flat plate, the resulting external force on the foil can be estimated by

$$\begin{aligned} f_3 &= f_A + f_L \\ &= -a_{33}(\ddot{h} + x_s\ddot{\delta} - U\dot{\delta}) - \frac{df_L}{d\alpha}\frac{1}{U}(\dot{h} - (-\frac{c}{4} - x_s)\dot{\delta} - U\delta) \end{aligned} \tag{4.21}$$

while the resulting moment is

$$f_5 = x_s f_A - (-\frac{c}{4} - x_s)f_L \tag{4.22}$$

considering that *Newton's* second law for the foil is given by

$$I\ddot{\delta} = f_5 \tag{4.23}$$

(4.23) can be rearranged to a more recognisable format:

$$a_f\ddot{\delta} + b_f\dot{\delta} + c_f\delta = \tau_f \tag{4.24}$$

where

$$\begin{aligned}
a_f &= I + a_{33}x_s^2 \\
b_f &= \frac{df_L}{d\alpha}\frac{1}{U}(-\frac{c}{4} - x_s)^2 - x_s a_{33} U \\
c_f &= \frac{df_L}{d\alpha}(-\frac{c}{4} - x_s) \\
\tau_f &= x_s a_{33}\ddot{h} + \frac{df_L}{d\alpha}\frac{1}{U}(-\frac{c}{4} - x_s)\dot{h}
\end{aligned}$$

4.2.4 Open-loop stability

The stability of the open-loop system in (4.24) is dependent on the position of the suspension, x_s. We can find the critical value of x_s by considering the system eigenvalues. If the real part of any eigenvalue for a mathematical system is positive, the system is deemed unstable.

The homogeneous part of the solution for a differential equation on the form $ay'' + by' + cy = \tau$ is

$$y = Ae^{\lambda_1} + Be^{\lambda_2} \tag{4.25}$$

where A and B are constants, while $[\lambda_1, \lambda_2]$ are the system eigenvalues. The eigenvalues can be found by solving the characteristic equation (the Laplace transform), of the homogeneous differential equation. Now, by examining (4.25) it is evident that the solution is unstable if either of the eigenvalues' real part is greater than zero, as y would grow exponentially.

We can therefore determine the boundary of stability by finding the systems eigenvalues and solving for x_s. The characteristic equation is

$$\lambda^2 a_f + \lambda b_f + c_f = 0 \tag{4.26}$$

and the eigenvalues must satisfy

$$Re\left(-\frac{b_f \pm \sqrt{b_f^2 - 4a_f c_f}}{2a_f}\right) < 0 \tag{4.27}$$

and as b_f and a_f are larger than zero for all possible values of x_s the stability criterion becomes

$$c_f > 0 \rightarrow x_s < -\frac{c}{4} \tag{4.28}$$

As long as $x_s < -\frac{c}{4}$ the foil system is stable, which is logical also by observation.

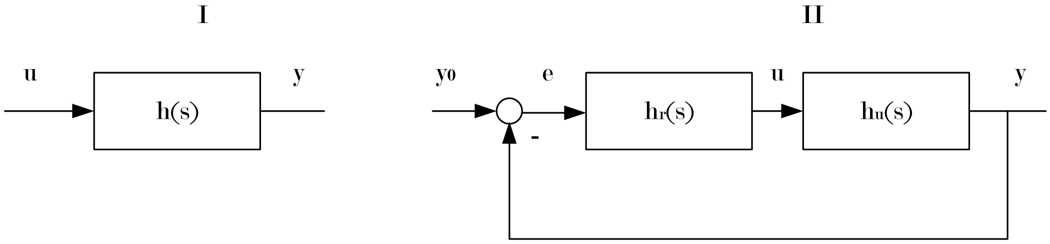

Figure 4.7: Open- and closed-looped systems. h_i are the system transferfunctions, u is the input, y is the output and y_0 is the reference signal. Signal e is the error on which the regulator is controlled

4.2.5 Closed-loop stability

A system that contains feedback-control is called a closed-looped system. Figure 4.7 illustrates the concept of feed-back control, where e is the difference (error) between the output signal, y, and the reference-signal, y_0. The output, u, from the regulator, h_r, is the input to the system, h_u, which again outputs y. The loop is repeated for all time. A closed-looped system is stable under the same criteria as for the open-looped equivalent, that is: $Re(\lambda_i) < 0$. However, the eigenvalues are changed due to the controller, and the system can be made stable where it is not in an open-loop set up.

4.3 Controller

Consider the open-loop foil system from equation (4.24). We wish to interact with the system and be able to control the foil angle δ to approach a given reference signal. The reference signal is the desired foil angle. The principles of control is to alter the original system parameters for the system to behave in a desired manner and satisfy a certain control objective. A controller applies external forces (through an actuator) that are proportional to the state variables. The fundamental examples are the PD- and PID-controllers.

4.3.1 PID-controller

Figure 4.7 illustrate a feedback system. The controller takes in the error and manipulates the signals to represent forces. The PID controller consist of proportional, -derivative and integrator gains, as presented in table 4.1.

PID	Name	Function	Cons.	Feature
P	Proportional	Stiffness	K_p	Amplifies present error
I	Integrator	Damping	K_i	Estimates future error
D	Derivative	Force	K_d	Accumulate past error

Table 4.1: Features of a PID-controller

The control law for the PID-controller can be expressed as (Balchen et al. [2004])

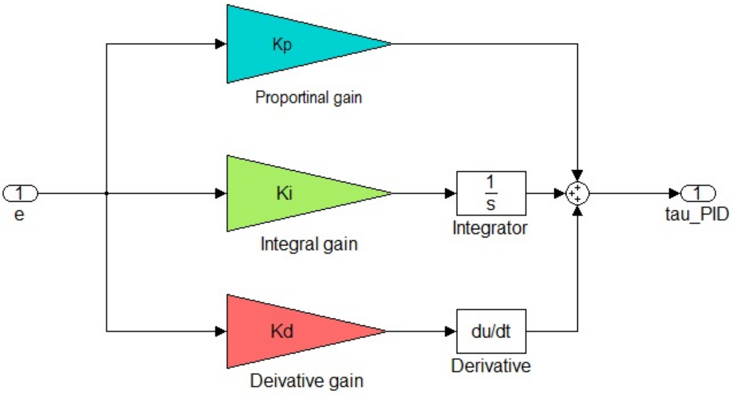

Figure 4.8: PID-controller. Cyan: Proportinal gain. Green: Integral gain. Red: Derivative gain

$$\tau_{PID} = -K_p(\delta - \delta_d) - K_d(\dot{\delta} - \dot{\delta}_d) - K_i \int_t (\delta - \delta_d)dt \tag{4.29}$$

where $(\delta - \delta_d) = e$ and δ is the actual angle of the foil, δ_d is the desired angle of the foil and e is the error of the control process at a given time. The transform of 4.29 yields

$$\tau_{PID}(s) = -K_p e(s) - K_d e(s)s - K_i e(s)\frac{1}{s} \tag{4.30}$$

In the frequency-domain s indicates a derivative and $\frac{1}{s}$ an integral. Hence, the process from (4.30) can be represented in a SIMULINK-block diagram as in figure 4.8. The effects of the controller is exemplified in the following section.

4.3.2 PD-controller

For simplicity we consider a PD-controller where the integrator gain is set to zero i.e $K_i = 0$. Considering the foil system in (4.24), and applying an external controller forcing we obtain

$$a_f\ddot{\delta} + b_f\dot{\delta} + c_f(\delta - \delta_d) = \tau_f + \tau_{PD} \tag{4.31}$$

For the sake of the example, we consider a zero value velocity reference signal $\dot{\delta}_d = 0$. In reality, this makes for a slightly different set up of the PD-controller, however this is not important in the following discussion. The foil equation of motion now reads

$$a_f\ddot{\delta} + (b_f + K_d)\dot{\delta} + (c_f + K_p)(\delta - \delta_d) = \tau_f \tag{4.32}$$

Evidently, the system coefficients has changed, which again affect the dynamics and stability of the system, in accordance with the system eigenvalues from (4.27).

In order to determine the value of the control gains, one could determine the desired characteristics of the controlled system in (4.32) and in that way find the unknown gains. The eigenfrequency, ω_0, and the relative damping factor, ς, are customary choices for tuning the control gains [Fossen, 2011, pg.372]:

$$\omega_0 = \sqrt{\frac{c_f + K_p}{a_f}} \quad \rightarrow \quad K_p = \omega_0^2 a_f - c_f \tag{4.33}$$

$$\varsigma = \frac{b_f + K_d}{2\omega_0 a_f} \quad \rightarrow \quad K_d = 2\varsigma\omega_0 a_f - b_f \tag{4.34}$$

In the above, we would like to tune K_p and K_d with a desired eigenfrequency, ω_d, and a desired relative damping factor, ς_d, of the system. Thus, the below holds

$$\omega_0 = \omega_d \tag{4.35}$$

$$\varsigma = \varsigma_d \tag{4.36}$$

so that (4.31) becomes

$$\ddot{\delta} + 2\varsigma_d\omega_d\dot{\delta} + \omega_d^2\delta = \omega_d^2\delta_d + \frac{\tau_f}{a_f} \tag{4.37}$$

If we assume that $a_f >> 1$, the external forcing vanish. For the foil system this assumption might prove blunt, and it must be experimented with. The following-condition now yields

$$\frac{x}{x_d}(s) \approx \frac{\omega_d^2}{s^2 + 2\varsigma_d\omega_d s + \omega_d^2} \tag{4.38}$$

The integrator can be accounted for by a *rule of thumb* (Fossen [2011]): $K_i = K_p\omega_d/10$. However, the need for the integrator in foil control is questionable, as there is little constant disturbance.

The step response of the following-condition in (4.38) is illustrated in figure 4.9. According to the figure, and judging by the nature of a large oscillating foil, $\omega_d < 5$ and $\varsigma < 1$ for speed. Beyond this, the parameters should be tuned in a simulation model or experiments, which will be considered later in the report.

4.4 Equation of motion

From (4.16) we know that the foil angle of attack can be expressed as

$$\alpha = -\frac{\dot{h}}{U} + \delta \tag{4.39}$$

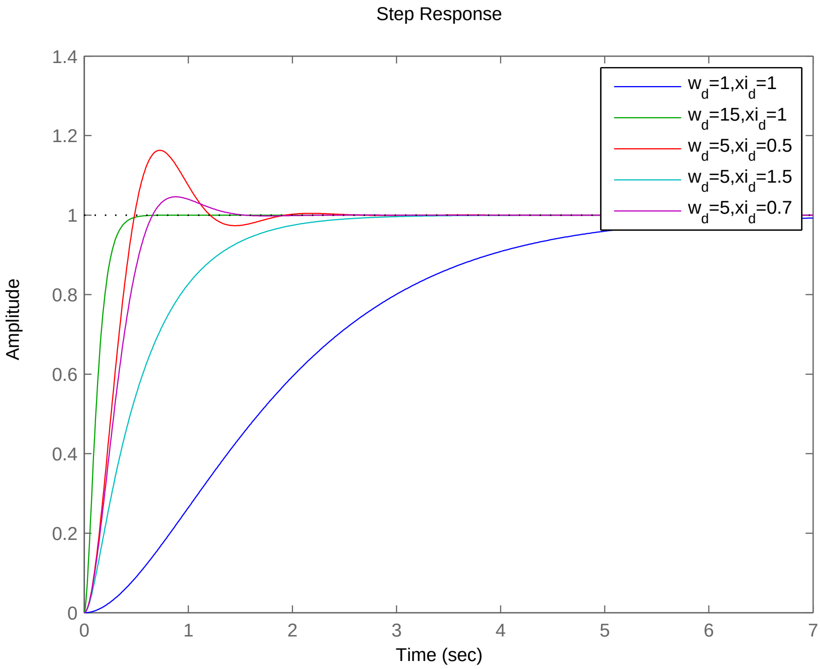

Figure 4.9: Step-response of foil system by setting the desired eigenfrequency and relative damping factor. $w_d = \omega_d$ is the desired eigenfrequency and $xi_d = \varsigma_d$ is the relative damping factor

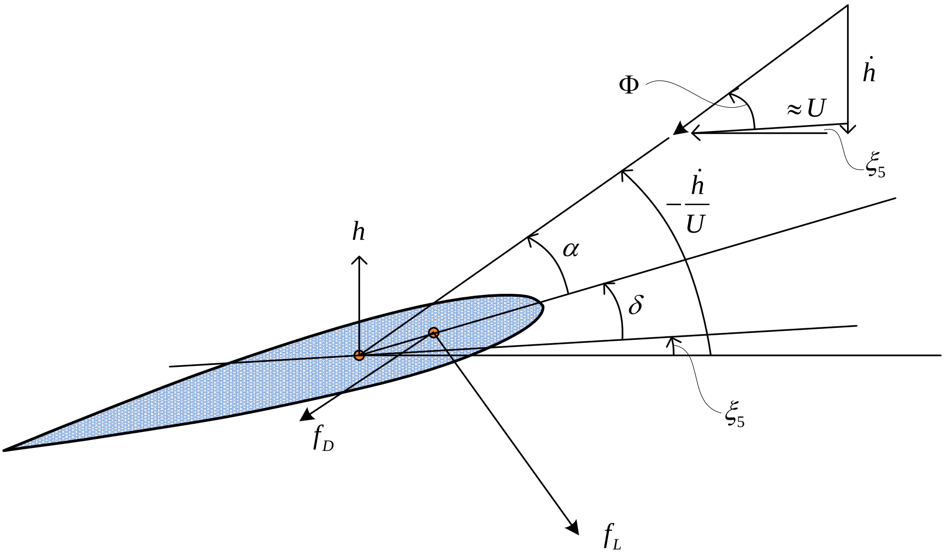
Φ
$\dot{h}$
$\approx U$
ξ_5
$-\frac{\dot{h}}{U}$
h
α
δ
ξ_5
f_D
f_L

Figure 4.10: Forces and angles of foil

where h is the vertical translation of the foil, and the vertical velocity due to a change in foil angle $\dot{\delta}$ has been assumed negligible.

The foil is fitted to a vessel in a sea-state, and the vertical velocity over the foil will consequently be affected by the vessel motion. The foil equation of motion and the vessel equation of motion can therefore be considered coupled. The magnitude of $\dot{h}$ can be denoted

$$\dot{h} = \dot{\xi}_3 - x_f\dot{\xi}_5 - \xi_5 U - w \tag{4.40}$$

where ξ_i is the mode of vessel motion, U is the vessel forward speed, x_f is the longitudinal position of the foil relative to CO and w is the vertical water particle velocity, defined as

$$\begin{aligned} w &= \frac{\partial \phi_0}{\partial z} && (4.41)\\ &= i\omega e^{kz}\zeta && (4.42) \end{aligned}$$

where ϕ_0 is the incident velocity potential and ζ is the wave elevation.

Again, we ignore the change in foil angle as source of vertical velocity and -acceleration. The quasi-static force on the foil is found from (4.21) and is given as

$$f_3 = -a_{33}\ddot{h} - \frac{df_L}{d\alpha}\frac{1}{U}(\dot{h} - U\delta) \tag{4.43}$$

where the first term is the diffraction (non-oscillatory) force and the second term is the (oscillatory) lift force. By applying 4.40, we obtain

$$\begin{aligned} f_3 = &-a_{33}(\ddot{\xi}_3 - x_f\ddot{\xi}_5 - \dot{\xi}_5 U - \dot{w}) && (4.44)\\ &- \frac{df_L}{d\alpha}\frac{1}{U}(\dot{\xi}_3 - x_f\dot{\xi}_5 - w - \xi_5 U - U\delta) && (4.45) \end{aligned}$$

Considering the unsteady oscillatory effects of the lift force, we apply the *Theodorsen*'s filter from section 4.1.2 to the angle of attack in the lift force. The unsteady oscillatory force can then be characterised by

$$\begin{aligned} f_3 = &-a_{33}(\ddot{\xi}_3 - x_f\ddot{\xi}_5 - \dot{\xi}_5 U - \dot{w})\\ &- \frac{df_L}{d\alpha}\frac{C(k_f)}{U}(\dot{\xi}_3 - x_f\dot{\xi}_5 - w - \xi_5 U - U\delta) \end{aligned} \tag{4.46}$$

The foil forces are coupled with the equation of motion for the vessel, according to *Newton's* second law:

$$\boldsymbol{M}\ddot{\boldsymbol{\xi}} = \boldsymbol{\tau}_{hyd} + \boldsymbol{\tau}_{hs} + \boldsymbol{\tau}_{foil} \tag{4.47}$$

where

$$\boldsymbol{\tau}_{foil} = \begin{bmatrix} 0 \\ 0 \\ 1 \\ 0 \\ -x_f \\ 0 \end{bmatrix} \int_s f_3 ds \tag{4.48}$$

Here, the foil force is integrated over the span. In this report, the cord length will be assumed constant over the span s and the integral reduces to a constant multi-plum of s. For notational convenience, the equation in (4.46) can be reformulated to

$$\boldsymbol{\tau}_{foil} = -\boldsymbol{A}_f(\omega_e) - \boldsymbol{B}_f(\omega_e) - \boldsymbol{C}_f(\omega_e) + \boldsymbol{\tau}_f \tag{4.49}$$

where the added mass, potential damping and restoring coefficients are listed in table 4.2.

A_{33}	$a_{33}s$
A_{35}	$-x_f a_{33} s$
A_{53}	$-x_f a_{33} s$
A_{55}	$x_f^2 a_{33} s$
B_{33}	$\frac{df_L}{d\alpha}\frac{C(k_f)}{U}s$
B_{35}	$-x_f \frac{df_L}{d\alpha}\frac{C(k_f)}{U}s - a_{33}Us$
B_{53}	$-x_f \frac{df_L}{d\alpha}\frac{C(k_f)}{U}s$
B_{55}	$x_f^2 \frac{df_L}{d\alpha}\frac{C(k_f)}{U}s + x_f a_{33}Us$
C_{35}	$-\frac{df_L}{d\alpha}\frac{C(k_f)}{U}s$
C_{55}	$x_f \frac{df_L}{d\alpha}\frac{C(k_f)}{U}s$

Table 4.2: Added mass-, potential damping- and restoring coefficients due to the foil. All remaining coefficients that are not listed above are null

4.4.1 Frequency-domain

The frequency-domain model for the foil is

$$[\boldsymbol{M} + \boldsymbol{A}(\omega_e, U)]\ddot{\boldsymbol{\xi}} + \boldsymbol{B}(\omega_e, U)\dot{\boldsymbol{\xi}} + \boldsymbol{C}\boldsymbol{\xi} = \boldsymbol{\tau}_{wave1} + \boldsymbol{\tau}_{foil} \tag{4.50}$$

The frequency response, of the vessel and the foil combined, is found by using the coefficients from table 4.2 and the motion RAO equation from (2.103). For the sake of verifying the foil coefficients, Prandtl's lifting line theory is used in deciding the lift coefficient. The foil dimensions are given in table 5.2. From figures 4.11 and 4.12, it is evident that the foil coefficients coincide well with VERES'. In the figures, a state-space and a simple time-domain model (see section 4.4.2) is also used in the comparison.

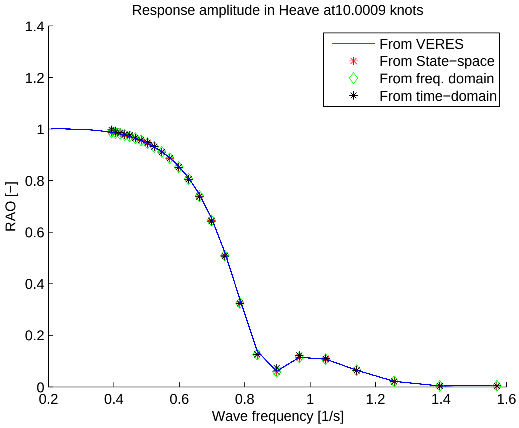

Figure 4.11: Frequency response of UT-751 supply vessel at 10 knots in heave with foil

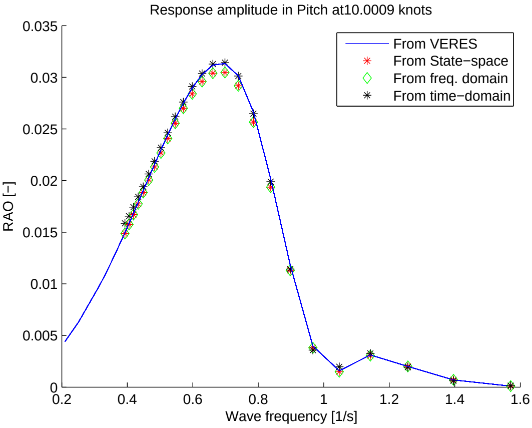

Figure 4.12: Frequency response of UT-751 supply vessel at 10 knots in pitch with foil

4.4.2 Time-domain

Opposed to in the frequency-domain, it is possible to add non-linear effects in a time-domain simulation, and it is therefore attractive for foil control operations. A simple time-domain model is shown in figure 4.13, where the black lines represent flow of forces. The foil forces are calculated according to (4.48). The vessel response is calculated from the hydrodynamic coefficients for a given frequency ω_e and a constant speed U, as in (4.50). It is stressed that, this model should be identical to VERES' result as it utilises the same speed-dependent coefficients, and not fluid memory. As can be seen from the figures 4.11 and 4.12, the time-domain model matches well with the results from VERES. However, for lower frequencies than those shown in the figures, the time-domain model is unstable. In a low-frequency range the hydrodynamic coefficients outputted from VERES are ill-defined and unstable i.e the eigenvalues for the motion RAO's are positive (at least some). This is one of the major reasons for why the application of *Cummins*' equation and an energy approach is favourable, over using the speed-dependent matrices from VERES and STF-theory. The reason for the instability are the singularities in the speed-dependent therms $1/\omega_e$ (see section 2.7.1). These are avoided in the infinite frequency environment of *Cummins*.

4.5 Thrust

The objective of the foil is to both reduce pitch motion and contribute with forward thrust. The thrust producing capabilities of the foil can be defined by the lift and drag coefficient. In theory,

$$\begin{aligned} f_T &= f_L \sin\Phi - f_D \cos\Phi && (4.51)\\ &\approx f_L\Phi - f_D && (4.52) \end{aligned}$$

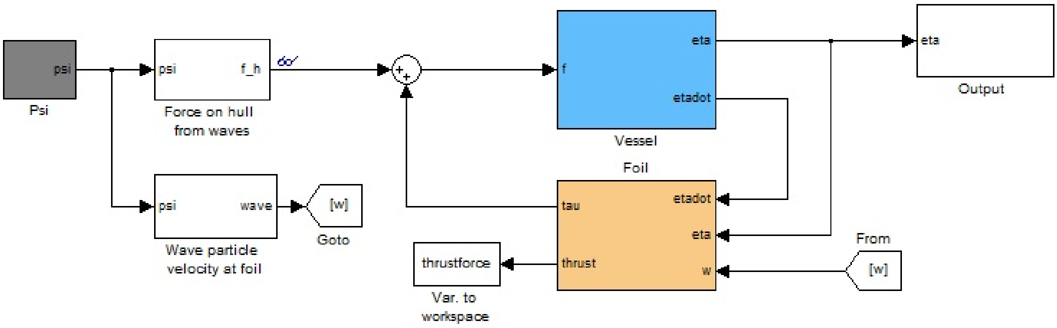
psi
Psi
psi
f_h
Force on hull from waves
psi
wave
Wave particle velocity at foil
[w]
Goto
f
eta
etadot
Vessel
Foil
tau
thrust
etadot
eta
w
thrustforce
Var. to workspace
From
[w]
eta
Output

Figure 4.13: A simple time-domain SIMULINK model. Gray: Incident wave. Light blue: Vessel system. Peach: Foil system

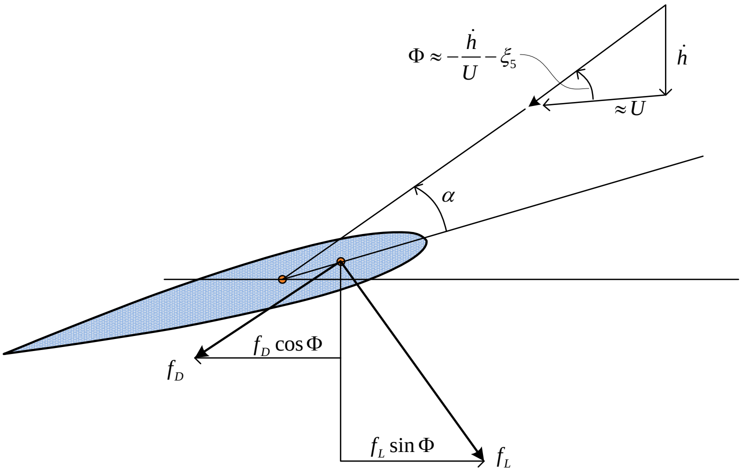
$\Phi \approx -\frac{\dot{h}}{U} - \xi_5$
$\dot{h}$
$\approx U$
α
$f_D \cos\Phi$
f_D
$f_L \sin\Phi$
f_L

Figure 4.14: Characteristic angles and forces on foil in unsteady flow

according to figure 4.14. Here, $\Phi \approx -\frac{\dot{h}}{U} - \xi_5$, when the forward speed is large compared with the vertical velocity over the foil. Φ is a characteristic angle in the quasi-static approach, and the angle of attack can thus be defined as

$$\alpha = \Phi + \xi_5 + \delta \tag{4.53}$$

4.5.1 Time-averaged thrust

Motivated by Borgen [2010], a method for finding the frequency-domain time-averaged thrust is presented. In the following we use Prandtl's lifting line theory, so that the force from (4.51) can be rewritten to

$$f_T = \frac{1}{2}\rho U^2 S \left(C_L \Phi + \frac{C_L^2}{\pi \Lambda} \right) \tag{4.54}$$

where

$$C_L = \frac{2\pi\alpha_e}{(1 + 2/\Lambda)} \tag{4.55}$$

The time-dependent terms in (4.54) are $\alpha_e \Phi$ and α_e^2, where $\alpha_e = C(k_f)\alpha$ is the effective angle of attack corrected for unsteady effects. Writing out Φ, we get

$$\Phi = \frac{1}{U}(\dot{\xi}_3 - x_f \dot{\xi}_5 - w) \tag{4.56}$$

whereas α is defined in (4.53), and the foil is fixed, which leaves $\delta = 0$. Now, the translations can be expressed in terms of motion RAO's for the vessel with a foil:

$$\xi_i = |H(\omega)_i| \cos(\omega_e t + \angle H_i(\omega) + \angle C(k_f)) \tag{4.57}$$

and the velocities as $i\omega_e \xi_i$. The motion RAO's are extracted from VERES. The wave velocity is given from (4.41) as $w = i\omega e^{kz_f} e^{-ikx_f} \zeta$ whilst $\zeta = \zeta_a \cos(\omega_e t)$. Thereby, the wave velocity can formally be expressed as

$$w = |\frac{w}{\zeta}| \zeta_a \cos(\omega_e t + \angle \frac{w}{\zeta} + \angle C(k_f)) \tag{4.58}$$

Time-averaging yields

$$\overline{\alpha_e \Phi} = \frac{1}{T_e} \int_0^{T_e} \alpha_e \Phi dt \tag{4.59}$$

$$\overline{\alpha_e^2} = \frac{1}{T_e} \int_0^{T_e} \alpha_e^2 dt \tag{4.60}$$

For the case of the UT-751 vessel with a fixed foil, the time-averaged thrust is obtained by

$$\overline{f_T} = \frac{1}{2}\rho U^2 S \frac{2\pi}{(1 + 2/\Lambda)} \left(\overline{\alpha_e \Phi} + \frac{2}{(\Lambda + 2)} \overline{\alpha_e^2} \right) \tag{4.61}$$

The method of Borgen [2010] will be verified using a time-domain model.

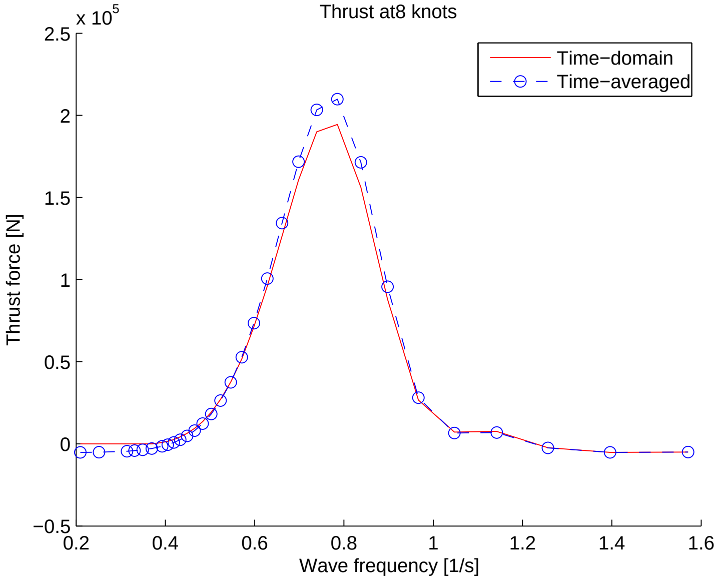

Figure 4.15: Thrust from time-domain simulation and a time-averaged frequency-domain model

4.5.2 Time-domain thrust

In the time-domain model from 4.13, thrust is outputted as a variable. The thrust is calculated in line with the non-linear version of equation (4.51). As the time-domain model was verified against the VERES, the model seems fit to verify the time-averaged thrust formulation from the previous section.

Figure 4.15 indicate that the two methods are, in fact, consistent. However, the time-averaged thrust slightly overestimate the thrust at resonance frequency compared to the time-domain counterpart. This might be due to the non-linear nature of figure 4.15.

4.6 Active control

To avoid stall and maximise thrust, active control of the foil is proposed. The theory is based on finding the theoretical optimal angle of attack and controlling the foil to this angle at all times. If the stall angle is known, stall could be avoided by limiting the angle of attack, by steering the foil angle δ.

From a theoretical viewpoint, maximum thrust is found by differentiation of the thrust force, with regards to the angle of attack. If the force is

$$f_T = f_L \Phi - f_D \tag{4.62}$$

then differentiation leaves

$$0 = \frac{f_L}{d\alpha}\Phi - \frac{f_D}{d\alpha} \tag{4.63}$$

where the angle of attack now is *optimal*; $\alpha = \alpha_{opt}$. For Prandtl's lifting line theory, the linear optimal angle of attack is found by rearranging (4.63) into

$$\alpha_{opt} = \frac{\Lambda}{4} \tag{4.64}$$

Now, if the foil could be steered to follow the optimal angle of attack we would maximise thrust. The optimal foil angle is found from (4.53) when $\delta = \delta_{opt}$

$$\delta_{opt} = \alpha_{opt} - \Phi - \xi_5 \tag{4.65}$$

In the above, the optimal foil angle is found from a theoretical approach, including neither viscous effects, non-linearities nor dynamic stall. A more solid methodology would be to use either non-linear theory or experimental results, in determining the optimal angle of attack and estimating the stall angle. In this report, we will use experimental results to find our optimal angle, which again will serve as a reference signal to our controller steering the foil. The results from the experimental findings are discussed in part II.

4.6.1 The controller

A PID-controller will be considered, according to section 4.3. The desired angle of the foil is to be calculated instantaneously, according to the theory in the previous section and used as a reference signal in the control algorithm. The control force then follows

$$\tau_{PID} = -K_p(\delta - \delta_{opt}) - K_d(\dot{\delta} - \dot{\delta}_{opt}) - K_i \int\limits_t (\delta - \delta_{opt})dt \tag{4.66}$$

Such a controller can be implemented in both a time-domain simulation and a frequency-domain model. For the frequency-domain model the motion RAO's must be calculated based on the controller gains. Consequently, the frequency-domain approach is not specifically suited for tuning the gains, but give valid approximations once the gains are set. The time-domain model is better suited for control design, and the main emphasis in this report will thus be on time-domain simulation models.

4.6.2 Spring-loaded foil

A spring-loaded foil can be simulated by a P-controller, hence the system is closed-loop with regards to the displacement of the foil.

Part II

Model Tests

Chapter 5

Models

The thrust-producing capability of the foil was tested in both the Marine Cybernetics Laboratory (hereafter called the MC-lab) and the towing tank, at MARINTEK in Trondheim. In the MC-lab the foil-model was run freely, while it was installed on a vessel-model for the experiments in the towing tank.

The vessel is of UT-751 Rolls Royce design in scale 1:16. The principal hull data for the full- and model-scale vessel is given in table 5.1.

	Symbol	**Unit**	**Ship**	**Model**
Length overall	L_{OA}	$[m]$	93.9	5.869
Length between perpendiculars	L_{PP}	$[m]$	80.8	5.050
Breadth moulded	B	$[m]$	21	1.312
Depth to 1^{st} deck	D	$[m]$	8.2	0.512
Draught at loading condition	T	$[m]$	4.3	0.269
Wetted surface	S	$[m^2]$	632.94	2.472

Table 5.1: Principal hull data and dimensions for the UT-751 design vessel in full- and model-scale

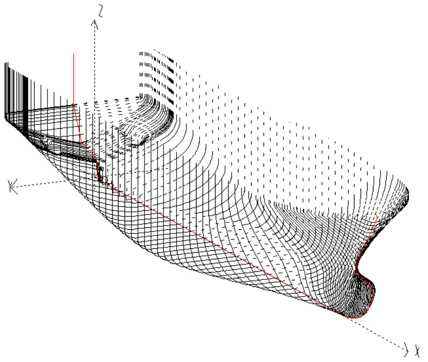

Figure 5.1: Vessel 3D drawing from ShipX

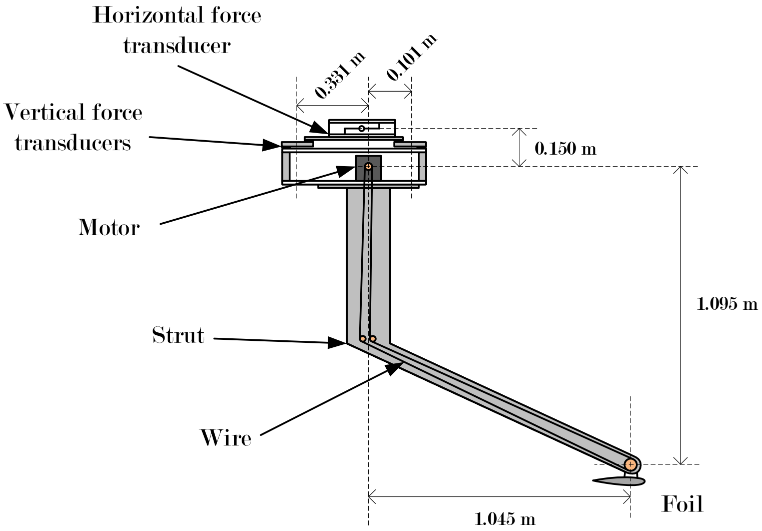

Figure 5.2: Foil system, including struts, motor and force transducers

The foil system was built independently of the vessel and could be installed or dismounted at will. During the tests in the towing tank, the foil was rigidly fitted through a 'moonpool' in the bow of the UT-751, whilst the vessel itself was free to move in all degrees of freedom.

5.1 Foil system

The foil is 3D-printed in a standardised NACA-0015 profile, equipped with five pressure sensors. The pressure sensors are meant to detect an actual angle of attack by knowing the pressure difference over the foil at all given angles. Further, the angle of the foil is mechanically adjustable by a small motor, interconnected by an arrangement of wires running within a strut. The strut is suspended between a hinged connection at the foil and the motor. Above the motor, sits the force transducers. The force transducers measure the relative vertical- and horizontal force between the foil system and the carriage/vessel. This can be interpreted as lift and drag forces. A figure of the foil system is given in 5.2.

	Symbol	**Unit**	**Ship**	**Model**
Span length	s	$[m]$	28.072	1.7545
Cord length	c	$[m]$	2.845	0.1778
Aspect ratio	Λ	$[-]$	9.867	-
Wetted surface (3D)	S	$[m^2]$	164.09	0.6603

Table 5.2: Principal dimensions for the NACA-0015 foil in full- and model-scale

Chapter 6

Marine Cybernetics Lab

6.1 Experimental set up

The foil system was connected to a hydraulic cylinder on the carriage in the MC-lab, in accordance with figure 6.1.

6.2 The experiments

6.2.1 Quasi-static approach

In the MC-lab, experiments were performed on a free-standing, bare foil (no vessel) to assess its performance in producing lift and its proneness to drag. Firstly, the foil was run at a range of static angles, α, at different velocities U.

$$\alpha\ [deg] \in -14:14 \tag{6.1}$$

$$U\ [m/s] \in [0.772, 1.029, 1.286, 1.543, 1.800] \tag{6.2}$$

From this data, under the assumption of quasi-static theory, the lift- and drag coefficient curves were calculated. The curves are shown graphically in figures 6.2 and 6.3. The dimensionless lift coefficients shows good compliance within the range of tested velocities, hence only a single run at $U = 1.286$ is reproduced in the figures. Although the drag coefficient deviate more among the velocities, figure 6.3 represent a fair trend. By regression, a trend line was found (the blue lines in figures 6.2 and 6.3) which represent the result of the quasi-static analysis.

The quasi-static lift coefficient valid for the range in (6.1), in radians, is

$$C_L = -37.618\alpha^3 - 0.197\alpha^2 + 5.614\alpha \tag{6.3}$$

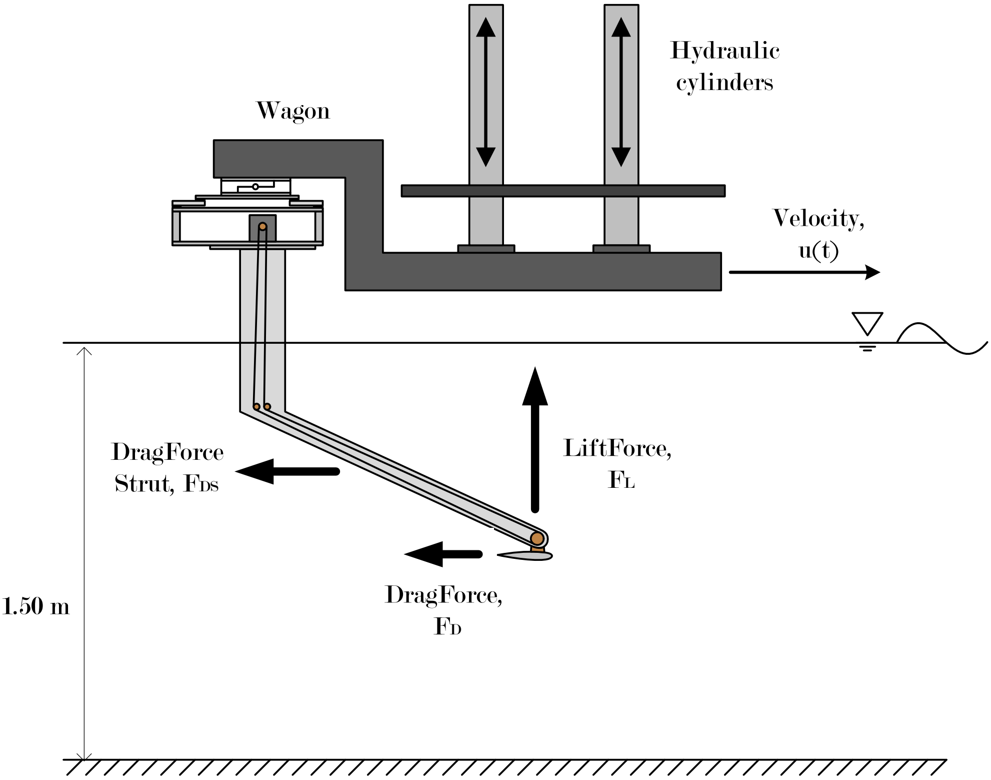

Figure 6.1: Experimental set up in Marine Cybernetics Lab

whereas the drag coefficient for the same range, in radians, is

$$C_D = 1.806\alpha^2 + 0.015 \tag{6.4}$$

According to equation (4.9) and the foil dimensions from 5.2, Prandtl's lifting line theory stipulate a $C_L = 5.224\alpha$, opposed to the linearised C_L from (6.3), which has a gradient of 5.614. The results are in harmony.

As for the drag coefficient, Prandtl's theory underestimates the actual drag measured in the experiments. On the contrary, the fitted curve overestimates the drag for low angles of attack. Nevertheless, the assumption of overestimating the drag force is preferred over the alternative. The constant term in (6.4) is referred to as viscous drag effects.

For the quasi-static theory, stalling appear at around 11 degrees, according to figure 6.2.

Angle of attack from pressure data

To be able to efficiently control the foil, the fluid velocity over the foil and the angle of attack should be known. One way of determining the angle of attack is by using pressure sensors on

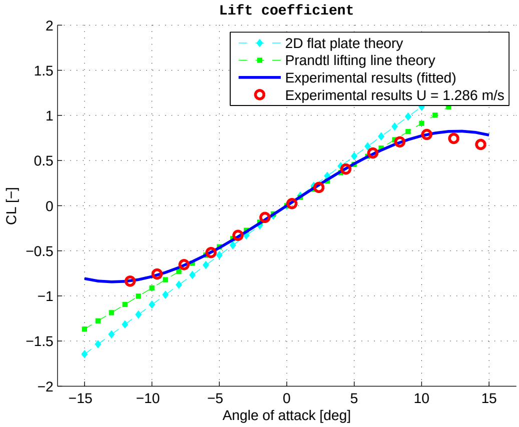

Figure 6.2: Lift coefficients for NACA15 at $R_n = 2.3e5$

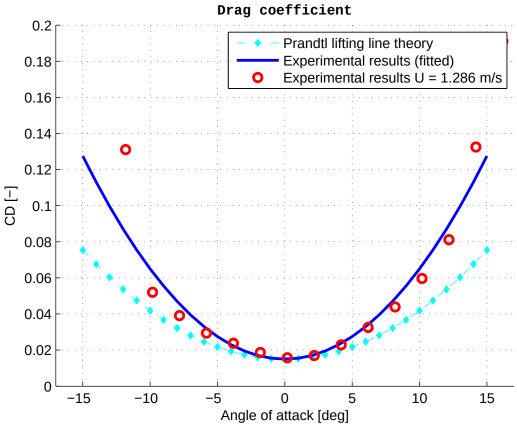

Figure 6.3: Drag coefficients for NACA15 at $R_n = 2.3e5$

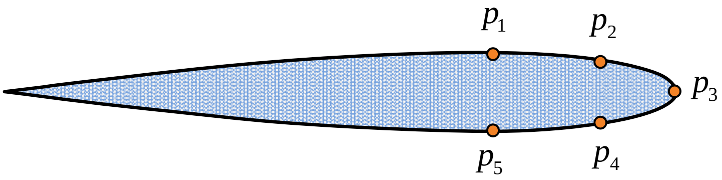

Figure 6.4: Pressure nozzles on the foil. The five pressures sensors named $p_1 - p_5$, in the clockwise direction are shown

the foil (see figure 6.4). The pressure at the sensors are sensitive to the angle at which the foil is projected. During the static runs the angle of attack and the pressure at all five sensors is monitored. By post-processing the data, a relation between pressure and angle of attack can be deducted. Using this relation and by monitoring the pressure data from the sensors in real-time, the pressure could be utilised in finding the angle of attack.

Firstly, a simple method of estimating the angle of attack is to use the pressure difference over the foil. From the experiments, the pressure difference, $p_5 - p_1$, seemed to give the most stable and coherent results when plotting against angle of attack. The dimensionless pressure difference was consistent for all the static runs, at different forward speeds. An illustration of the results is given in figure 6.5. In this method, the speed over the foil is still unknown and must be assumed.

An alternate approach in finding the angle of attack was proposed by PhD-candidate Eirik Bockmann. In this procedure, the pressure-differences $p_5 - p_3$ and $p_3 - p_1$ were plotted against each other, in a two-dimensional scatter-plot (see figure 6.6). Each point in the scatter represent an angle of attack, at a given speed. The theory encompassed using the entire 2D-domain in finding both the velocity over the foil and the angle of attack. In real-time, as p_1, p_3 and p_5 is known, the two differences make up a single point in the graph. By means of interpolation the velocity and angle of attack can be determined. In this method, both speed and angle can be decided. However, the method is restricted to operate within a quasi-static non-stalling environment which limit its applicability in dynamic systems. This is because the dynamic stall angle far exceeds its quasi-static equivalent, which we shall see. Additionally, the method is prone to numerical errors in the interpolation.

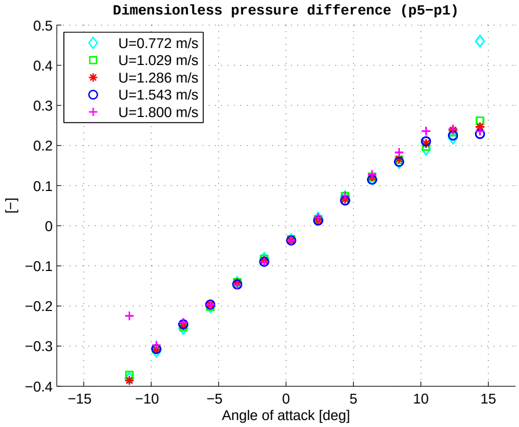

Figure 6.5: Quasi-static lift coefficient versus angle of attack, estimated from the pressure difference over the foil

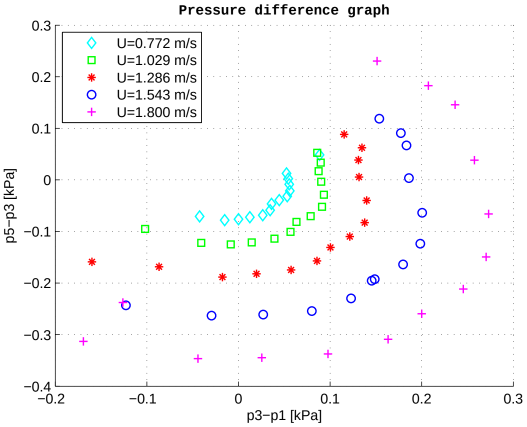

Figure 6.6: Quasi-static pressure difference interpolation chart. The extreme points for each half-circle is the limiting angle of attack (AoA) in the range $[-12 : AoA : 12]$

6.2.2 Dynamic approach

Using the hydraulic cylinders, the foil was exposed to oscillatory motion. A range of heave-amplitudes and periods were experimented with, to define the characteristics of the foil in an unsteady flow regime. Two scenarios will be highlighted in the discussion to follow; flow below stall angle and flow on the verge of stalling. Unfortunately, the results never actually showed clear signs of stalling as the angle at which stall occurred was much higher than expected. As result, we were unable to describe the dynamic effects in full. As a basis for understanding the graphs to be discussed, a brief explanation is appropriate:

Angle of attack: The angle of attack was calculated based on

1. data from the pressure sensors. A fitted line from the plot in figure 6.5 is used to estimate the angle of attack
2. relative vertical velocity at foil centre of pressure. The relative velocity was calculated by time differentiation of the heave-displacement measured in the experiments. The heave velocity was then filtered with a zero-phase low-pass filter, to reduce noise. The quasi-static angle of attack was found by $-\dot{\xi}_3/U$, according to the theory. The angle of attack was adjusted for unsteady effects using *Theodorsen*'s function

Lift forces: The lift forces were found based on

1. forces on the vertical transducers. This is referred to as the actual lift force of the foil and is measured

2. the estimated angles of attack. Here, either the quasi-static non-linear C_L from (6.3) could be used or Prandtl's theory. Both procedures were utilised. However, Prantdl's theory proved more accurate for large angles of attack. The speed over the foil was estimated geometrically by the forward speed and the vertical velocity.

Added mass forces: The added mass forces were calculated from the acceleration of the foil. Again, a low-pass filter was used in omitting noise from the signals after differentiation. The added mass is made dimensionless in the same manner as the lift coefficient

Hysteresis: The lift coefficient was plotted against the angle of attack for one period of oscillations

6.2.3 Scenario 1: No stall

In the scenario described below, the maximum angle of attack obtained was ten degrees, well below the quasi-static stall angle. Figures 6.7-6.8 exemplify the run from post-processing, while the info-box below present the parameters.

Scenario 1		
Speed carriage	U	1.286 m/s
Period of oscillation	T	2.375 s
Heave amplitude	ξ_{3a}	0.0886 m
Maximum angle of attack	α_{max}	10°

The relative vertical velocity overestimate the angle of attack, with respect to the pressure approach. However, when the unsteady effects are accounted for by *Thedorsen*'s function the estimates are in line (see figure 6.7).

When using the estimated angles of attack to find the lift force, the result coincide well with the actual vertical force measured by the transducers, as illustrated in figure 6.7. In this range of angles, the Prandtl theory and the quasi-static C_L give the same results.

Figure 6.8 illustrate the lift coefficient and the dimensionless non-oscillatory added mass coefficient. It is evident that the lift forces are dominating when the foil is at speed. From the hysteresis plot, we see that the lift coefficient runs more or less along the quasi-static lift coefficient curve and there are few traces of dynamic effects.

6.2.4 Scenario 2: Stalling

In this scenario we consider a run which exceeds the stalling limits of 11 degrees, from quasi-static theory. The maximum angle of attack approaches 15 degrees, and it seems the foil is on the verge of stalling.

Scenario 2		
Speed carriage	U	1.286 m/s
Period of oscillation	T	2.125 s
Heave amplitude	ξ_{3a}	0.135 m
Maximum angle of attack	α_{max}	15°

From figure 6.9 it is evident that, the pressure-estimate for the angle of attack suffer from what appear to be stall. Turbulence seem to build up around the pressure sensors and they are incapable of describing the actual angle of attack. From scenario 1, the relative vertical velocity over the foil proved to be sound in estimating the angle of attack. In this scenario it suggests the angle of attack is approaching 15 degrees. From figure 6.5, it is apparent that the pressure sensors start deviating from the constant gradient and thus are not suitable for estimating the angle, as illustrated here. Moreover, 6.9 suggest that the unsteady effects are very important for this range of angles. The hysteresis plot in figure 6.10, also show signs of dynamic effects and a phase shift appearing.

Figure 6.9 show that the relative velocity prediction seems to coincide well with the actual lift force, which indicate that the foil has not yet approach its stalling-limit. Meanwhile, the pressure sensors predict stall and are thus proven unsuitable to describe the angle of attack for large angles.

Additionally, figure 6.9 clearly indicate that the non-linear, quasi-static lift coefficient from 6.3 is unusable for prediction of the lift force at large angles.

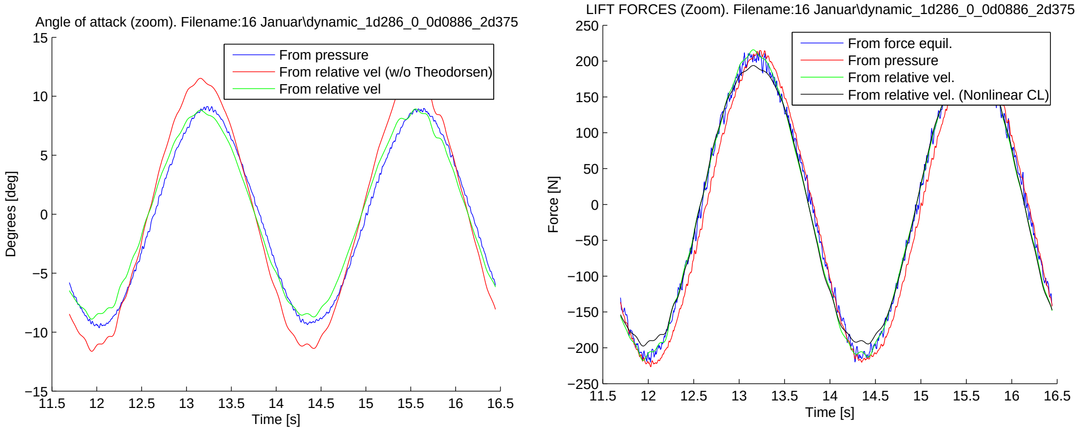

Figure 6.7: Angle of attack (left) and lift forces (right). Angle of attack calculated from pressure (blue) and relative vertical velocity with and without *Theodorsen*'s function (green and red, respectively). Actual measured lift force (blue) vs forces calculated from pressure (red) and relative vertical velocity (green is Prandtl's theory and black non-linear theory). Carriage speed $U = 1.286m/s$, period of oscillation $T = 2.375s$ and heave amplitude $\xi_{3a} = 0.0886m$

6.2.5 Thrust

The main aim of the experiment in the MC-lab is to be able to predict the thrust force. From the discussion of the two different scenarios, it is made clear that the relative vertical velocity give the most representative angle of attack. Hence, this angle of attack is used for estimation of the thrust force. Firstly, the lift force was identified as in the above discussion. Meanwhile, the drag force was calculated based on the C_D from (6.4). The thrust was then computed according to equation (4.51). From figures 6.11 and 6.12, we see that the estimate give a fair indication of the actual thrust force.

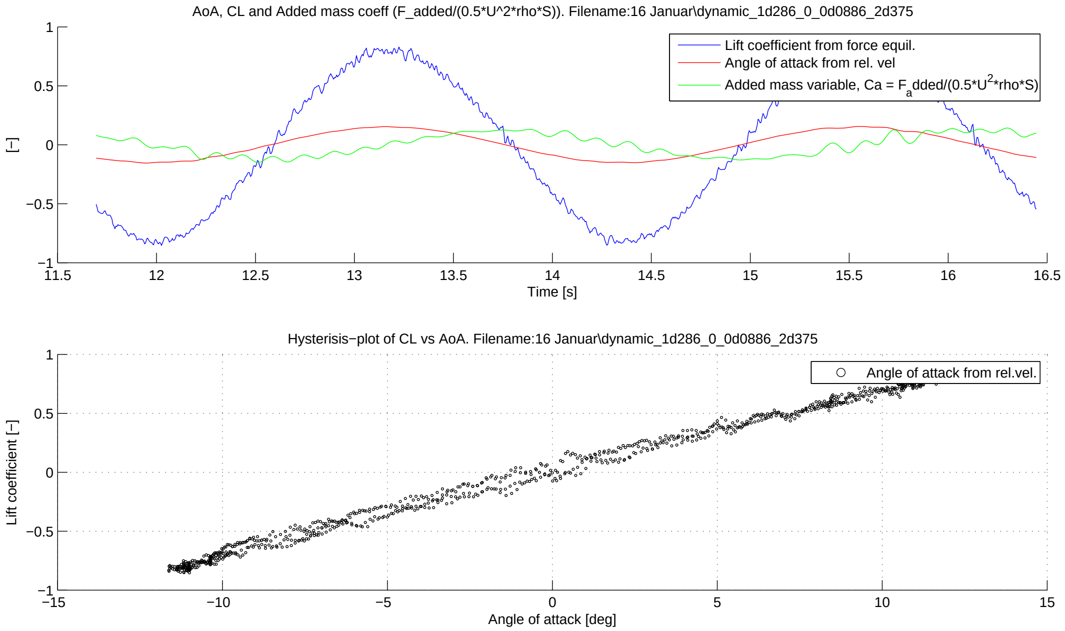

Figure 6.8: Plot A: Comparison of oscillatory and non-oscillatory forces and angle of attack. Plot B: Hysteresis plot; C_L vs α. Cariiage speed $U = 1.286 m/s$, period of oscillation $T = 2.375s$ and heave amplitude $\xi_{3a} = 0.0886m$

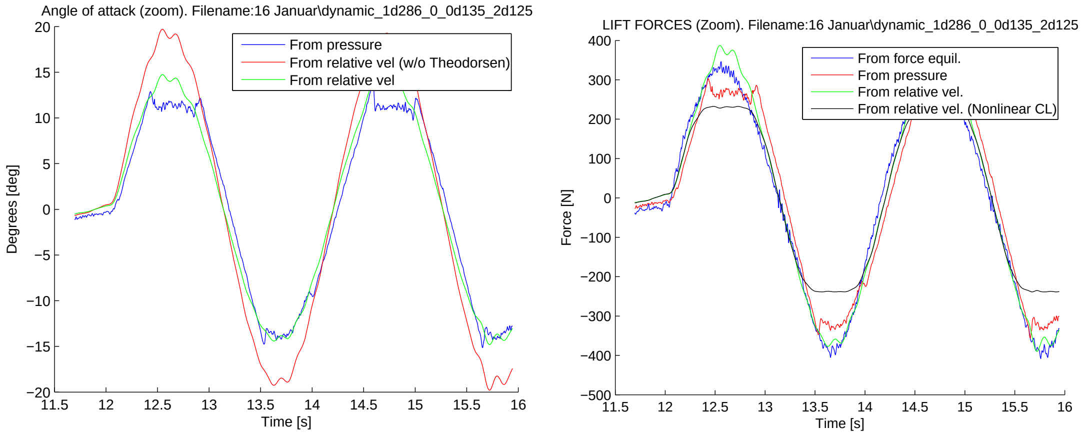

Figure 6.9: Angle of attack (left) and lift forces (right). Angle of attack calculated from pressure (blue) and relative vertical velocity with and without Theodorsen function (green and red, respectively). Actual measured lift force (blue) vs forces calculated from pressure and relative vertical velocity (green is Prandtl's theory and black non-linear theory). Carriage speed $U = 1.286 m/s$, period of oscillation $T = 2.125s$ and heave amplitude $\xi_{3a} = 0.135m$

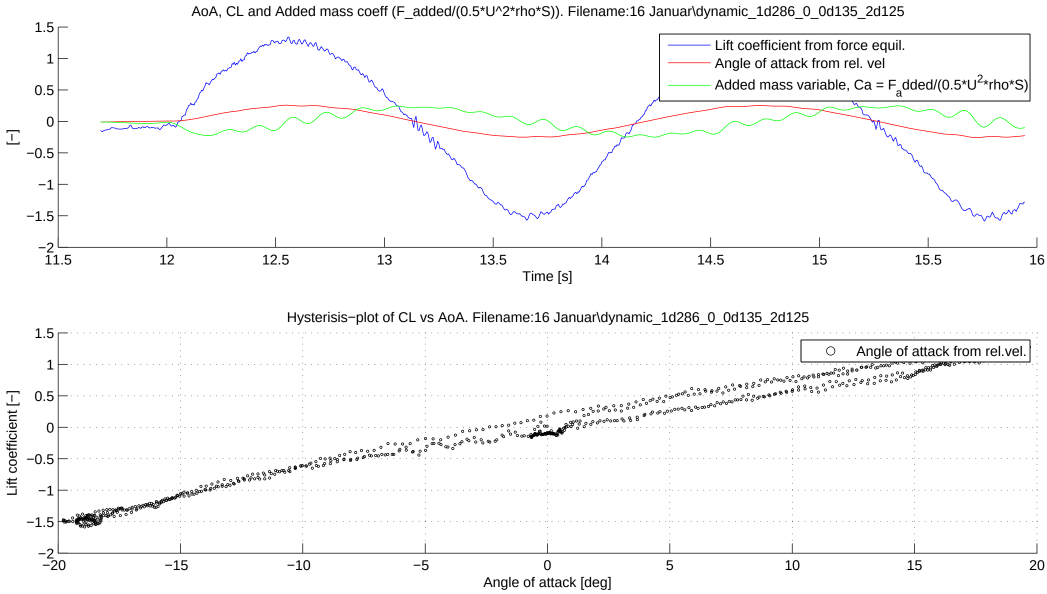

Figure 6.10: Plot A: Comparison of oscillatory and non-oscillatory forces and angle of attack. Plot B: Hysteresis plot; C_L vs α. Cariiage speed $U = 1.286 m/s$, period of oscillation $T = 2.125 s$ and heave amplitude $\xi_{3a} = 0.135 m$

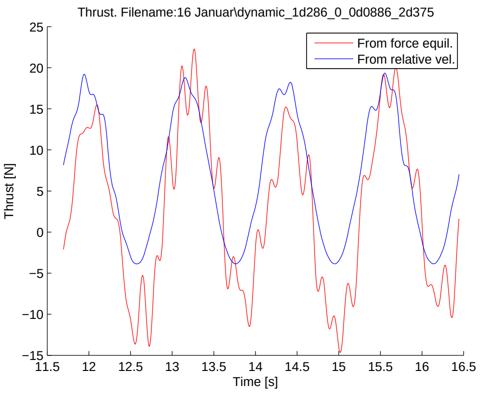

Figure 6.11: Thrust force on foil from scenario 1. Red: Actual. Blue: Estimate

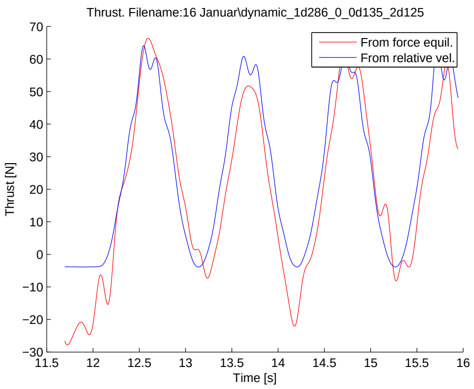

Figure 6.12: Thrust force on foil from scenario 2. Red: Actual. Blue: Estimate

Chapter 7

MARINTEK Towing Tank

7.1 Experimental set up

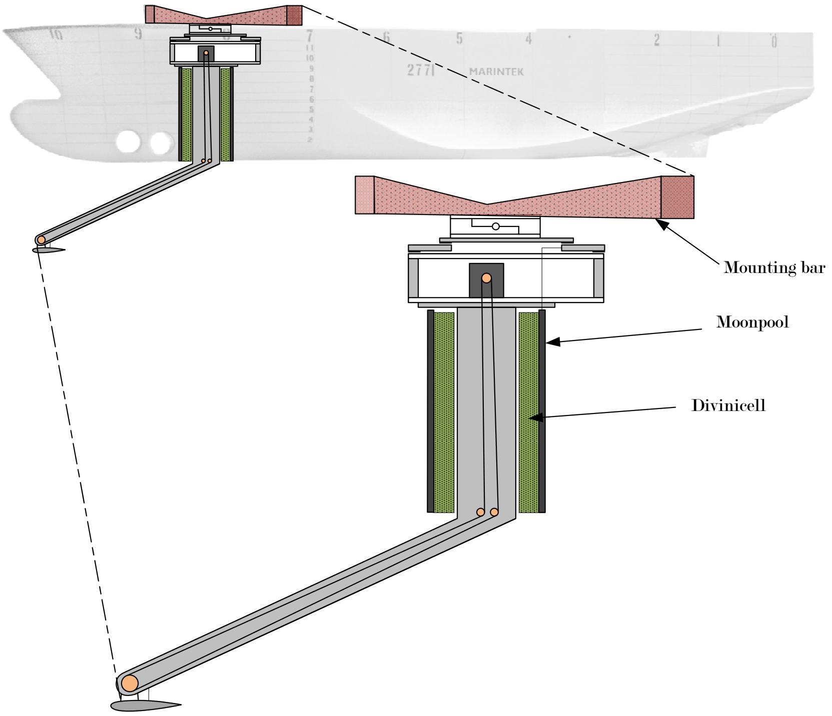
2771
MARINTEK
Mounting bar
Moonpool
Divinicell

Figure 7.1: Experimental set up in towing tank

The experiments in the towing tank were performed with the foil mounted to the UT-751 supply vessel model. The foil system set up was identical to the one in the MC-lab and fitted through a *moonpool* in the bow of the vessel, as visualised in figure 7.1. The space between the vessel hull and the struts was filled with divinicell foam, with some space left for the struts to displace without touching the foam. As for the MC-lab experiments, vertical and horizontal transducers monitored the lift and thrust force.

7.2 The experiment

Test were performed for the vessel without foil, with a fixed foil and using active control of the foil. The runs with a bare ship were performed in order to calculate the calm water resistance and have a benchmark for the test including the foil. The results from the tests with a fixed foil proved the most interesting. We were able to set op motion RAO's, thrust curves and added resistance profiles to compare with the bare-vessel runs. That being said, the results showed many signs of irregularities which have been difficult to predict and explain, and thus pose a challenge when establishing a simulation model. As there were many irregularities in the *simple* set up for a fixed foil, the irregularities and experimental errors were many-folded when introducing an actively controlled foil. Consequently, the findings from the runs with active control will be discussed in section 7.4, but not be included directly in the analysis of the results. The performance was too poor and the results bound with too many uncertainties.

The runs were performed in regular waves for range of wave periods at wave height 3 m, at a range of vessel speeds (see 7.1).

Towing tank runs		
Speed carriage	U	8 kn, 10 kn, 12 kn
Wave period	T	6.5 s, 7.5 s, 8.5 s, 9.5 s, 10.5 s, 11.5 s
Wave amplitude	ζ_a	1.5 m

Table 7.1: Run data for towing tank

The aim is to be able to predict the results of the experimental results using the procedures presented in the MC-lab chapter. If we are able to estimate the results from the towing tank, the basis for making a solid simulation model is set. In the following we shall see how the estimates coincide with the experimental data.

7.2.1 Time-series

Graphed run: $U = 10\ kn$, $T = 9.5\ s$ and $\zeta_a = 1.5\ m$

The time series used as a principle area of discussion in this section is from the time-series in figure 7.2. The time-series spans all the velocities from table 7.1, however the data within $U = 10\ kn$ is primarily used (middle part of the time-series). The wave period is $T = 9.5\ s$ and the wave amplitude is $\zeta_a = 1.5\ m$.

7.2.2 RAO's

In comparing the RAO's from the experimental data with RAO's from VERES, the general observations are (see figures 7.5-7.10):

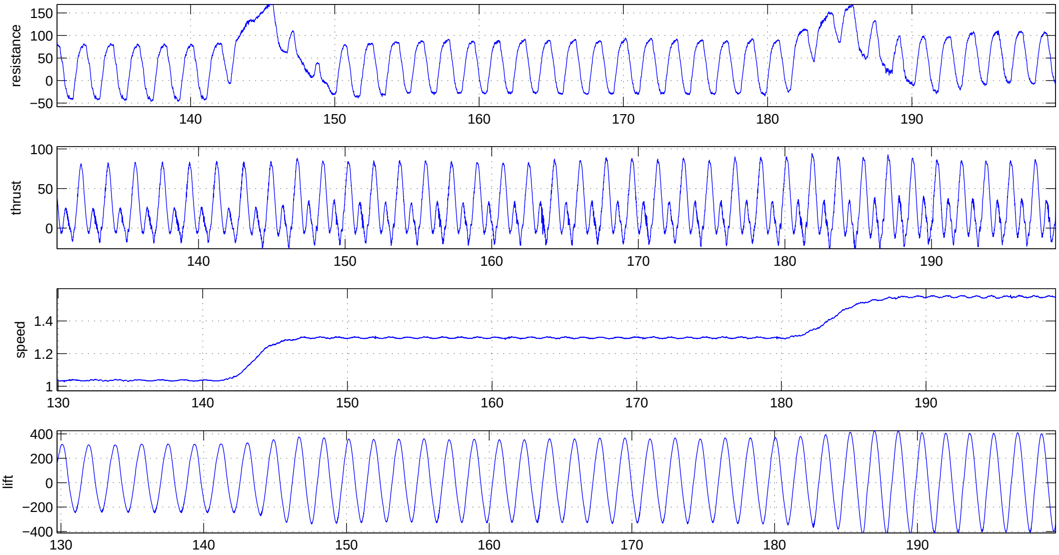

Figure 7.2: Time series results from towing-tank in model-scale. Top: Total surge force on vessel $[N]$. Top-lower: Thrust force from foil $[N]$. Bottom-upper: Speed of carriage $[m/s]$. Bottom: Lift force on foil $[N]$.

In heave:

1. Without foil
    (a) For low speed the response in the experiments surpass the response from VERES
    (b) For low speed there is a dip in the RAO at pitch resonance
    (c) For high speed the trends correlate well, although VERES slightly underestimate the response
2. With foil
    (a) For low speed there is a dip in the response at pitch resonance which is not reflected in the VERES results
    (b) For higher speed the results coincide well

In pitch:

1. Without foil
    (a) At low speed at resonance frequency there is a dip in the pitch response
    (b) The result coincide well for higher and lower frequencies
    (c) For high speed relative deviation is approximately constant
2. With foil
    (a) VERES overestimate the pitch response for all speeds and frequencies

(b) The relative deviation is approximately constant for all speeds and frequencies.

It is evident that the experimental data match fairly well with the computational results at moderate vessel response. When the vessel is experiencing large response action the frequency-domain, linear model is not coping. This might indicate that the bare vessel is experiencing non-linear effects. However, when the foil is fitted the response reduction is significant and VERES' model is in line.

As a whole, there is a significant reduction in pitch and heave response for the case with a fixed foil compared to the response of a bare vessel. The heave response for the vessel with a fixed foil is reduced with 60%, for a wave period of $T = 7.5\ s$. The pitch response reduction is 50%, at the same period. Figures 7.3 and 7.4 illustrate the heave and pitch reduction in percent. This reduction will directly affect the added resistance as it is dependent on the vessel response (see section 2.5), and thereby the fuel efficiency of a foil fitted vessel.

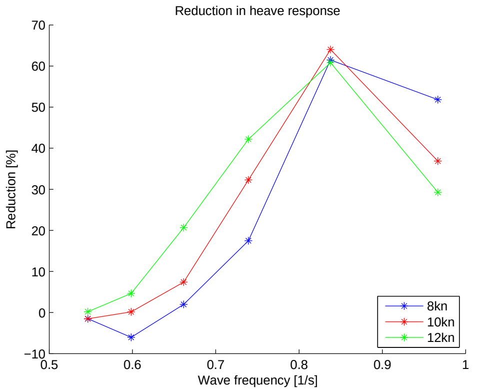

Figure 7.3: Heave reduction from experiments

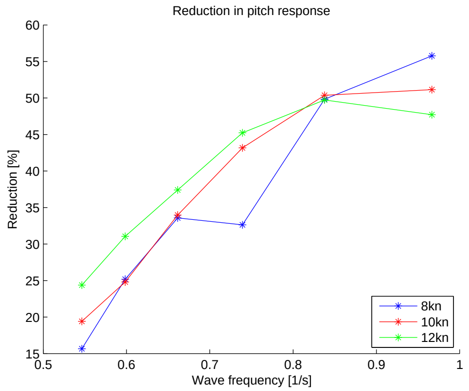

Figure 7.4: Pitch reduction from experiments

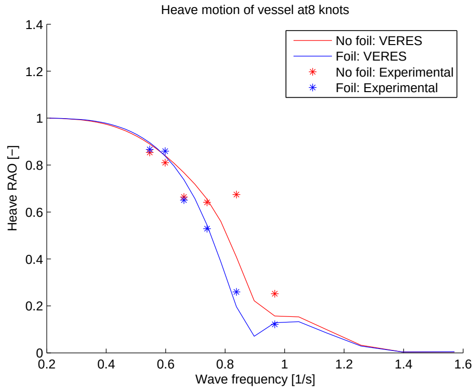

Figure 7.5: Experimental RAO in heave at 8 knots

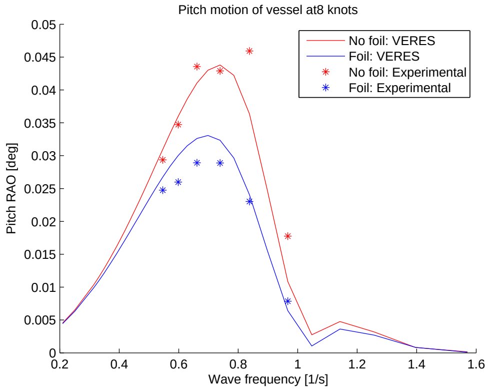

Figure 7.6: Experimental RAO in pitch at 8 knots

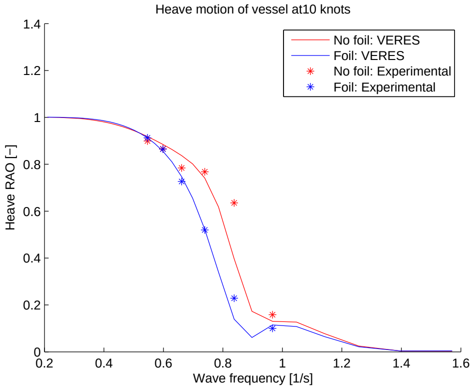

Figure 7.7: Experimental RAO in heave at 10 knots

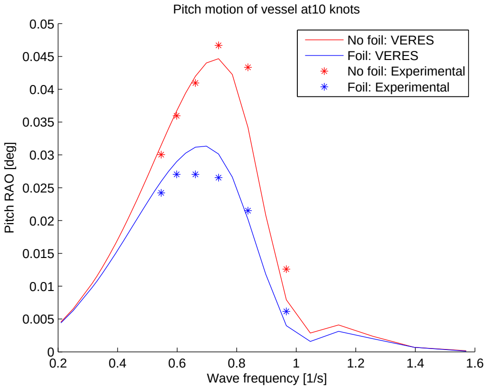

Figure 7.8: Experimental RAO in pitch at 10 knots

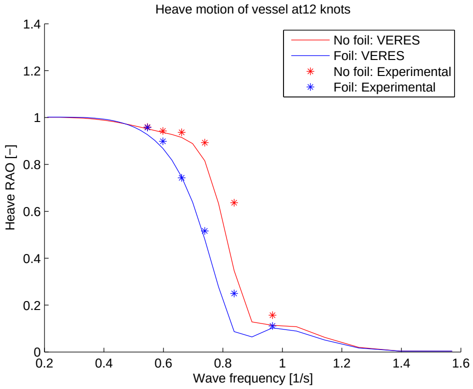

Figure 7.9: Experimental RAO in heave at 12 knots

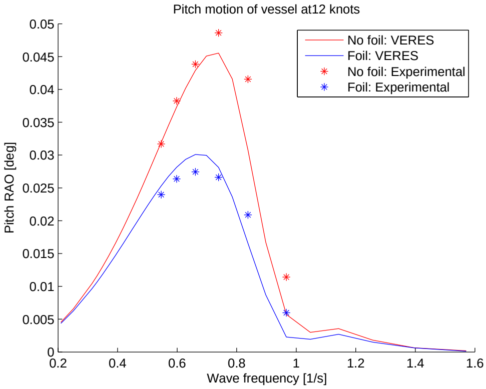

Figure 7.10: Experimental RAO in pitch at 12 knots

7.2.3 Angle of attack

Graphed run: $U = 10\ kn$, $T = 9.5\ s$ and $\zeta_a = 1.5\ m$

In order to estimate the lift, drag and thrust force in the foil, the angle of attack was identified, using the same techniques as for the MC-lab experiment post-processing. This time, the relative velocity was more intricate, as wave action (at the foil depth), and pitch- and heave response was taken into account. Additionally, the phase of the relative velocity depended on the position of the foil with regards to CO, *Theodorsen*'s function and the wave action.

The angle of attack was also estimated by the pressure data. From figure 7.11, it is made clear that the angle of attack found from the pressure method in figure 6.5 and the one calculated from relative vertical velocity concur. The pressure estimate from Bockmann's interpolation method undershoot corresponding to the two others, and is faced with a slight phase shift. It is noted that Bockmann's method was applied real-time during the experiments and is therefore prone to a phase shift when filtering the signals before interpolation.

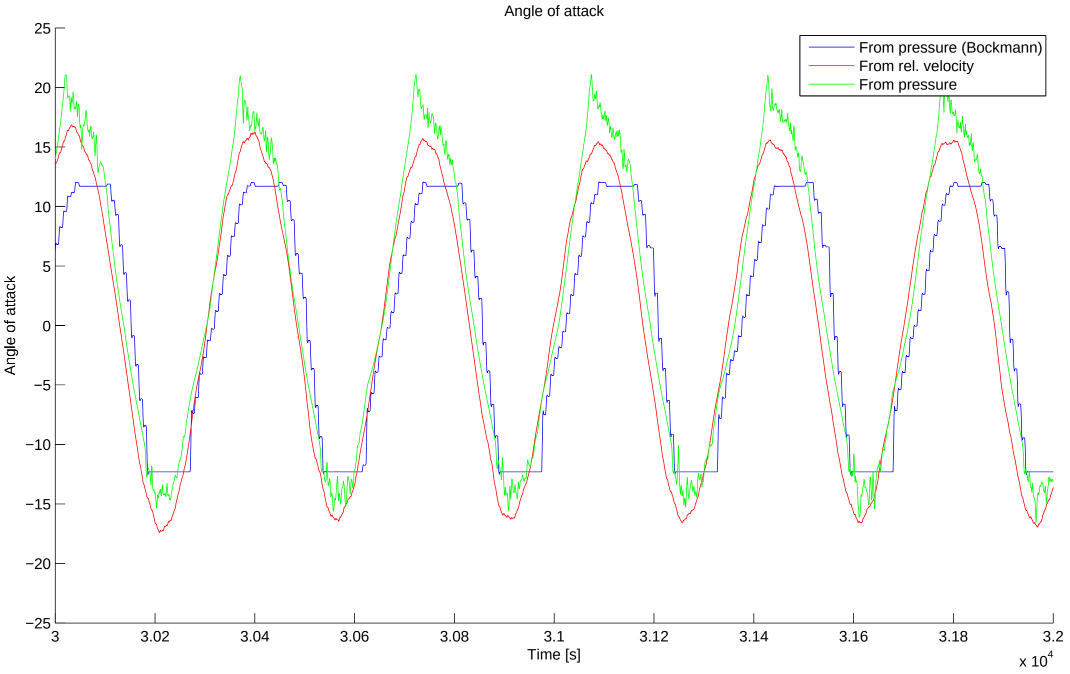

Figure 7.11: Angle of attack of foil. Blue: Angle estimated by Bockmann interpolation method. Red: Calculated from relative vertical velocity. Green: Estimated from pressure sensors

7.2.4 Lift, drag and thrust

Graphed run: $U = 10\ kn$, $T = 9.5\ s$ and $\zeta_a = 1.5\ m$

The thrust- and the lift force was both measured during the tests and estimated in post-processing. The lift and drag was found based on the angle of attack from relative vertical velocity (which concurred well with the angle of attack from pressure). Prandtl's lifting line theory was used in finding the lift coefficient (as the experimental C_L performed poorly in a unsteady flow regime), while the experimental C_D was the basis for calculating drag. The measured and estimated lift force is illustrated in figure 7.12, and they seem to match well. The measured and calculated thrust force is graphed in figure 7.13. It is evident that the thrust-estimate is largely exaggerating the actual measured thrust, which is odd. During the downward action of the foil the measured thrust halts, while the lift force is unaffected. The phenomena is unknown to the author, and will cause large deviations when it comes to estimating the thrust force for a given sea-state. According to the figure it can be expected that the mean actual thrust force is half that of the estimate.

The mean thrust force was extracted from the experimental data and plotted against the time-averaged thrust from section 4.5.1 (see figures 7.16, 7.18 and 7.20). Confirming our suspicion, the mean experimental thrust lies significantly lower than the time-averaged, especially at low speed. The fact that the models for estimating thrust is poor, complicates the implementation of mathematical simulations.

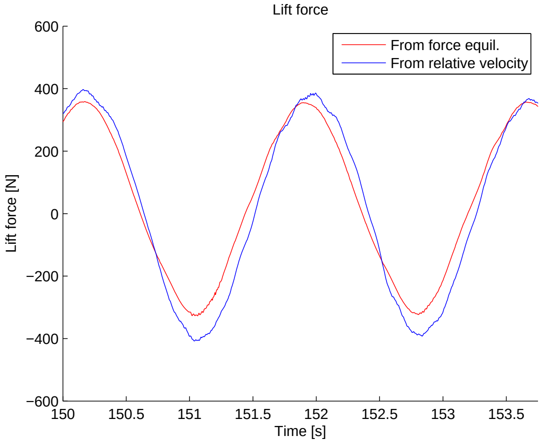

Figure 7.12: Lift force on foil in $[N]$ at 10 kn. Red: Measured force. Blue: Estimated from relative velocity

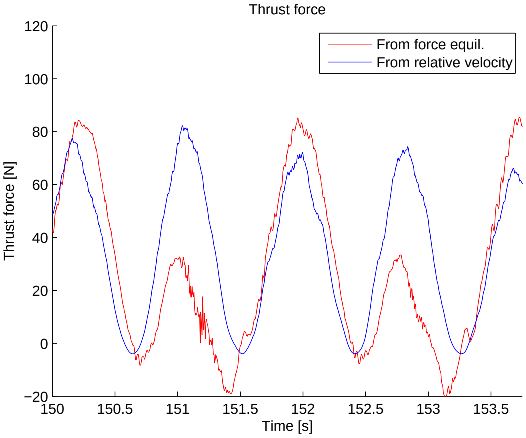

Figure 7.13: Thrust force on foil in $[N]$ at 10 kn. Red: Measured force. Blue: Estimated from relative velocity

7.2.5 Total resistance

The total resistance of the vessel is measured with and without foil. The reduction in resistance at resonance frequency approaches 65%, which indicate massive fuel saving potential. Figure 7.14 illustrate the resistance reduction for all frequencies.

7.2.6 Calm water resistance

In order to find the added resistance, it is imperative to identify the calm water resistance. From the experiments, the total resistance of the model in calm water is deemed known. Using the algorithm in 2.5.2 we can find the full-scale calm water resistance. The total resistance is shown in figure 7.15, along with the estimate from VERES (Holtrop).

7.2.7 Added resistance

In advanced time-domain simulations, the added resistance plays an important role in modelling the horizontal forces correctly. Therefore, we try to deduct the added resistance from the model test data.

The force equilibrium in horizontal direction for the full-scale vessel reads:

$$F_x = R_T + R_{AW} - F_T \tag{7.1}$$

where F_x is the resistance force measured in the model test, R_T is the calm water resistance and F_T is the thrust force on the vessel from the foil. It is stressed that the force conversion from model to full-scale is proportional to λ^3, where λ is the scaling factor between model- and full-scale.

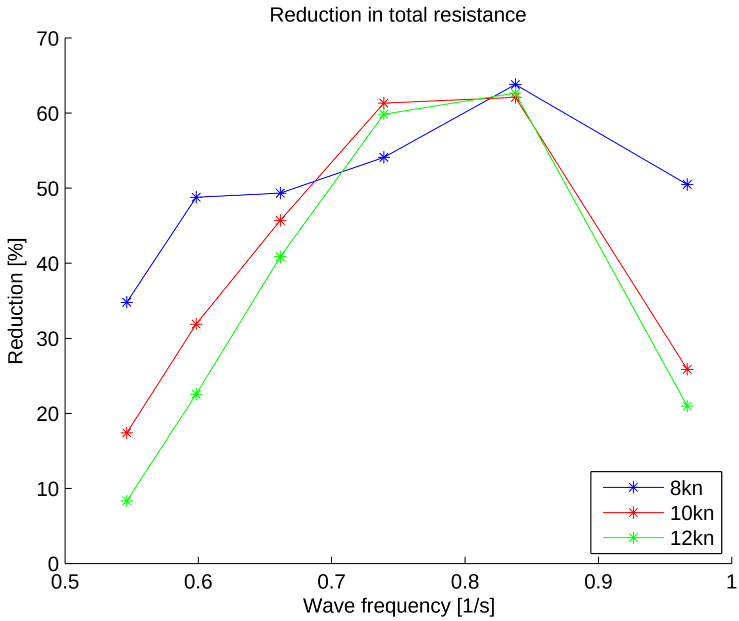

Figure 7.14: Total resistance reduction between a vessel- with fixed foil and without foil at 8 *kn* (blue), 10 *kn* (red) and 12 *kn* (green). Conditions: $T = 9.5\ s$ and $\zeta_a = 1.5\ m$

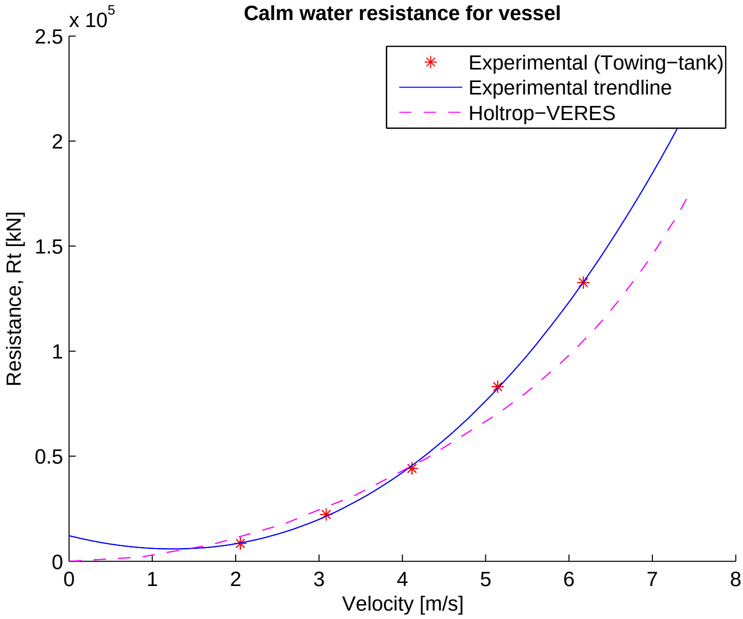

Figure 7.15: Calm water resistance of full-scale vessel. Red stars: Experimental results. Blue: Fitted to experimental data. Magneta dotted: Holtrop method as outputted by VERES

From (7.1) the added resistance can be estimated. Figures 7.17 to 7.21 show the experimental added resistance versus VERES' estimate using Gerritsma & Beukelmanns eqaution for wave drift (see section 2.5). The figures indicate that the added resistance is substantially higher than what is expected, particularly for the vessel without foil. As added resistance is proportional to the square of the wave relative response amplitude, rather small deviation in response-estimation will be exponentially inflated in the added resistance calculations, which defend the large discrepancies in the figures.

Moreover, at resonance frequency the added resistance is reduced with approximately 50% for the foil case. For lower frequencies, however, the added resistance is more or less the same.

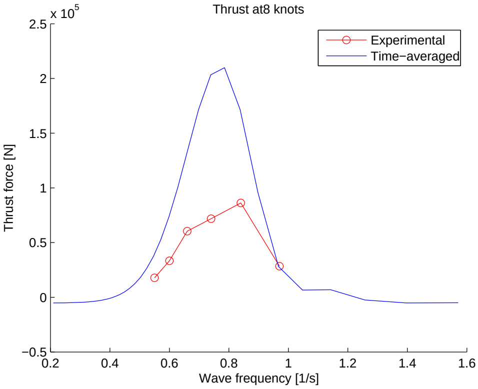

Figure 7.16: Thrust force 8 *kn*. Red: Experimental. Blue: Time-average

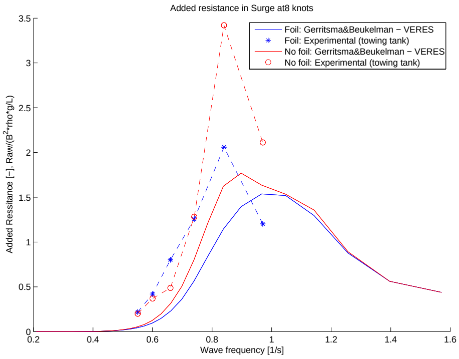

Figure 7.17: Non-dimensional added resistance 8 *kn*. Dots: Experimental. Line: VERES

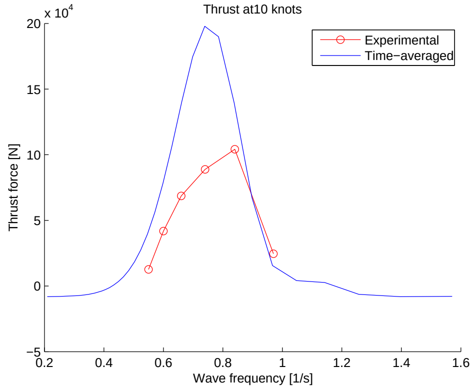

Figure 7.18: Thrust force 10 *kn*. Red: Experimental. Blue: Time-average

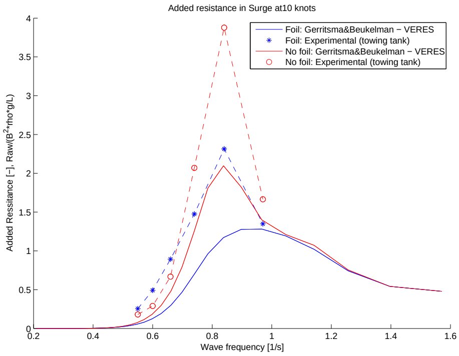

Figure 7.19: Non-dimensional added resistance 10 *kn*. Dots: Experimental. Line: VERES

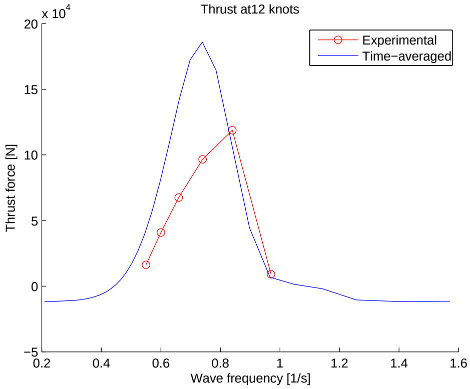

Figure 7.20: Thrust force 12 *kn*. Red: Experimental. Blue: Time-average

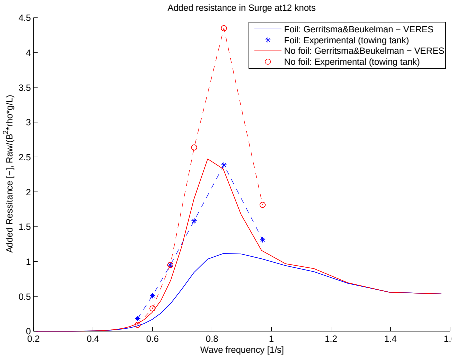

Figure 7.21: Non-dimensional added resistance 12 *kn*. Dots: Experimental. Line: VERES

7.3 Concluding remarks

The model test show large reduction in both heave and pitch when applying a fixed foil to the vessel. As a result, the added resistance is significantly reduced. Furthermore, the reduction in added resistance combined with the forward thrust from the foil contributes to reducing the total resistance of the vessel with 65%, at most. A reduction in resistance is synonymous with fuel efficiency, which is desirable in many respects. However, it must be noted that the experimental tests were performed under optimal conditions, in head sea and in a sea state where the vessel experienced large heave and pitch responses.

What is more, the model test gave us important feedback with respect to the validity of the prediction methods for thrust. The tests showed that the angle of attack, most probably, can be calculated in decent compliance with the actual angle. However, although the calculated lift force complied respectably, the thrust force showed large deviation and was about half of the expected mean value, which was strange.

7.4 Active control

In active control, the aim is to optimise the angle of attack and to prevent stall from setting in. The latter has proven difficult, as the dynamics of the flow complicate the modelling and stalling is delayed with respect to the quasi-static theory. The theory of maximising thrust was partly successful. *Successful* due to the fact that the resistance was generally reduced with about $0 - 10\%$ comparing to the runs with fixed foil. *Partly*, because the behaviour of the foil when actively controlled was difficult the explain, and the method was bound with many uncertainties and sources of error.

The active control algorithm was based on calculating an optimal angle of attack and controlling the foil accordingly, in real-time. The following algorithm was adopted in real-time guidance and control of the foil:

1. The angle of attack was found from the pressure sensors by adopting Eirik Bockmann's interpolation code and the graph in 6.4
2. Φ (from equation 4.53) was calculated based on the angle of attack and the pitch angle
3. The optimal angle of attack could be calculated from $\Phi = C_D/C_L$ (see equation 4.63). Here, the quasi-static C_L and C_D from (6.3) and (6.4) coefficients were utilised
4. By knowing the optimal angle of attack, the optimal foil angle δ_{opt} could be deducted according to 4.65
5. δ_{opt} was regarded as the input-value to the PID-controller and the motor steering the foil

The theory seems fine, however the following list sums up the areas of uncertainty:

1. The active control algorithm was based on quasi-static theory and the non-linear C_L and C_D, from (6.3) and (6.4). The post-processing from the MC-lab experiments clearly showed that the C_L was unsuitable in an unsteady flow environment, as it predicts abrupt stalling when the dynamic system is not even close to its stall limit. The test showed that the foil could encounter a 15° angle of attack without stalling, whilst the quasi-static C_L was based on a $10 - 11°$ limit
2. The towing tank post-processing showed that there was a delay in the signals coming from the interpolation code, which again is relayed into the control of the foil
3. The interpolation code itself is limited to operating within ±12°, which again underestimates the dynamic effects
4. The PID-controller was sat in the motor which again took in the guidance signal δ_{opt}. By investigation, there was a large delay from relaying the input-signal, to when the foil was actually in position. A better approach would have been to have the PID-controller in the computer algorithm, which then could control the moment (force) to be excited on the motor. By this, an unnecessary link would have been avoided
5. The physical set up of the wiring between the motor and the foil was too weak. The wiring slipped and the foil moved out of position when exposed to large forces. In turn it was impossible to determine the actual foil angle
6. The motor itself was not strong enough to withstand the forces on the foil and acted more as a stiff spring
7. There might have been errors in the SIMULINK-code

Throughout the simulations, a LabView real-time interface was used. The control algorithm was coded in SIMULINK and compiled for the LabView software to interpret. The following sections give an overview of the hardware and software used in the active control system.

7.4.1 Hardware and Software

For control and monitoring of the foil system, a National Instrument CompactRIO (NI cRIO-9074) data-acquisition and processing unit was used (www.ni.com). The CompactRIO chassis is an integrated system that combines a real-time processor and a reconfigurable field-programmable gate array (FPGA). The CompactRio has eight slots for NI-C-Series Input/Output (I/O) modules. The I/O modules are linked to the foil system sensors and control signals. The FPGA is programmed in the National Instrument (NI) LabView software, through a LabView Virtual Instrument (VI). LabView is a graphical programming environment that can target FPGA's on NI Reconfigurable I/O (RIO) hardware (in this case a CompactRIO). To implement the foil control algorithm in LabView, a SIMULINK model is created. By using the Mathworks Simulation Interface Toolkit (SIT) and the Real-Time Workshop, the SIMULINK model can be converted to a dynamic link library (DLL) file, which again is readable by LabView. The DLL-file is stored on the real-time processor in the CompactRIO. When the DLL file is communicating with a LabView VI, all variables in the original SIMULINK model (*filname.mdl*) can be altered and monitored at will, real-time [Wahl].

The actual actuation of the foil was done by a MARINTEK controller and motor.

Simulation Interface Toolkit (SIT)

The SIT provides the code for a seamless interface between the LabView-software and a SIMULINK-model. SIMULINK is a model-based programming environment integrated in MATLAB. The SIT package is an add-on from the basic SIMULINK package and includes a plug-in for a Real-Time workshop.

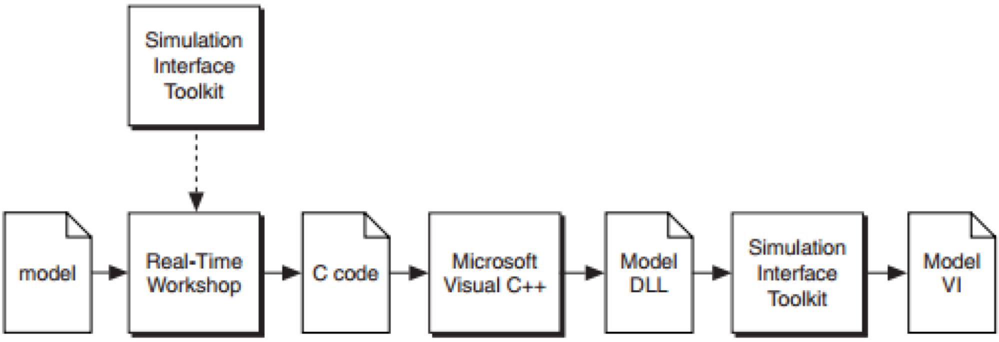

Figure 7.22: Simulation Interface Toolkit flowchart. Source: www.ni.com

A model for the controller design is set up in SIMULINK. The conventional input and output ports in SIMULINK are replaced by their SIT input- and output counterparts. When compiling the SIMULINK model into a DLL-file the system recognises these as real-time I/O connection points i.e the physical signals to be used when controlling the foil (pressure, velocity etc) can later be connected to the SIMULINK model via these ports. The SIMULINK model can then incorporate the signals in the model algorithm, process the signal according to the defined model and output new variables through the SIT output-port. LabView then gains access to the output-values from the SIMULINK model and uses those outputs according to the model set up in the LabView VI. For active control of the foil, the output from SIMULINK is a controller input signal. This signal is then relayed to the physical controller steering the foil angle through LabView. LabView takes in the signals from the pressure sensors etc. which again are relayed back to SIMULINK. And so it goes. However, it is not that simple.

In our case, we are to run the SIMULINK model *on* a real-time processor (the CompactRIO) and we thus need to convert the SIMULINK model into a dynamic link library file (DLL-file) that LabView can interpret and call. This is done by the Real-Time Workshop. The Real-Time Workshop converts the SIMULINK model-file to C-code and then compiles the C-code into a DLL-file using Microsoft Visual Basics (see figure 7.22 for a flowchart of the process). The DLL-file can then be run, independently of SIMULINK, through a model-VI on the real-time target (our CompactRIO).

LabView

LabView is a graphical programming platform that allows for GUI-programming. In LabView, we set up a new FPGA-project. FPGA is a field-programmable gate array that is situated on the CompactRIO unit. In short the FPGA is a programmable microchip. The microchip communicates with the I/O modules of the CompactRIO. For foil control, the FPGA is used to digitise the analogue signals from our sensors that are connected to the I/O modules. The signals are then transferred to the Real-Time processor in the CompactRIO chassis (being our Real-Time (RT) target), which also handles the model-DLL through the host-VI.

In the FPGA-project in LabView, we create a virtual instrument (VI), being our host-VI. The VI is of GUI interface and is what the user sees and what the system appears as on the screen. This VI is set up according to the needs of the experiment, including features for monitoring and manipulation of variables. For example, as we monitor the performance of our controller we can alter the control parameters of a PID-controller (being the proportional-, derivative- or integral gains) real-time. Or we could plot the foil angle of attack in real-time. This is possible as the VI is coupled to the original SIMULINK model (now our model-DLL) using the SIT Connection Manager tool in LabView. Here we link our host-VI (GUI-interface) to the RT target (CompactRIO). The features for monitoring and manipulation of variables in the VI in LabView are mapped to the corresponding variables in the original SIMULINK model. In addition, the hardware connected to the FPGA (sensors etc) is mapped to its corresponding SIT I/O ports in the original SIMULINK model, as mentioned. Through the SIT Connection Manager it is also possible to log data, which is accumulated on the CompactRIO processor, when running the model.

The host-VI and the RT-target (CompactRIO) communicate over a TCP or IP network. Figure 7.23 illustrate the communication scheme and the different parts of the total system.

The routine for implementing a LabView-SIMULINK model is featured in appendix B.

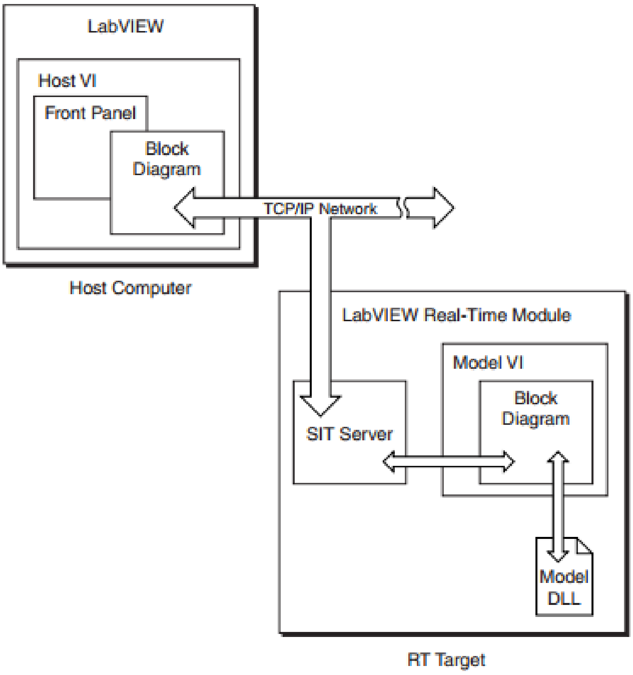
LabVIEW
Host VI
Front Panel
Block Diagram
TCP/IP Network
Host Computer
LabVIEW Real-Time Module
Model VI
Block Diagram
SIT Server
Model DLL
RT Target

Figure 7.23: Flowchart of the communication between the Real-Time (RT) target and the Host-VI. The RT target is the CompactRIO hardware while the Host Computer is the user hardware. Source: www.ni.com

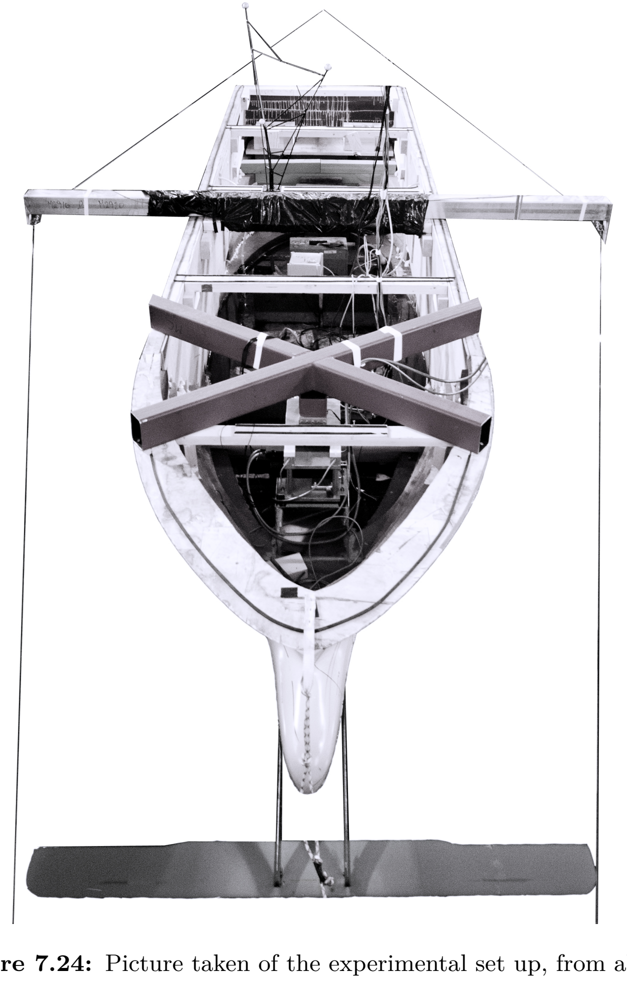

Figure 7.24: Picture taken of the experimental set up, from above

Part III

Mathematical Simulation

Chapter 8

Choice of Model

Throughout the previous chapters, some theory of mathematical modelling and verification with model tests has been presented. It has been emphasised that, in order to verify the potential of a foil propulsion system a solid model should be established. On that account, a simulation model has been chosen to best fit the purpose of simulating a vessel with a foil system. In deciding upon the model the following was considered:

1. The model should be as versatile as possible and should be designed so that it can easily be expanded to account for effects not included in this report
2. Any type of forces can be applied including resistance, added resistance etc.
3. Non-linear effects can be accounted for
4. Simulations can be done for any sea-state and in any heading
5. Active foil control or a spring-loaded can be appended
6. The user can easily adjust the controller gains
7. The model can be used for any speed

With that in mind, a time-domain model based on *Cummins*' equation seems best fit. A time-domain model is capable of coping with non-linear effects and can easily be expanded and adjusted at will. The foil forces are easily implemented, and active control can be tested. As for *Cummins* equation, the model is then independent of speed-dependent added mass and damping coefficients from potential theory. This is favourable in modelling arbitrary speed profiles.

The frequency-domain models are highly powerful and fast, and give important feed-back in a preliminary design phase. However, it is of the authors opinion that a time-domain model is more suited for verifying the potential of the concept. For instance, the thrust force in the experimental results from the towing tank showed strange behaviour. This is difficult to implement in a frequency-domain model, but can be accounted for by non-linear effect in a time-domain equivalent. Moreover, control design is best done in a time-domain model.

It should also be mentioned that, VERES' hydrodynamic coefficients are invalid for frequencies lower than approximately 0.2 rad/s. A time domain simulation with VERES' coefficients, at forward speed, in a low-frequency environment, is unstable. This is not possible to determine by only examining the RAO's. The source of the instability lies in the eigenvalues of the motion RAO's - some of the eigenvalues of the six degree of freedom RAO's are positive (the real part). Once the eigenvalues are positive, the system is unstable, as discussed in section 4.2.4. The reason for why the eigenvalues are positive, lies in the nature of the speed-dependent hydrodynamic coefficients. For any dynamic system existing in the world, the inertia matrix is symmetric and of positive nature (T. I. Fossen), which is not the case for VERES' added mass coefficients. In summary, the VERES coefficient can not be used in time domain simulation, for a sea-state where the frequencies span from zero and upwards.

That being said, it is possible to use the motion RAO's for time-domain simulation in forward speed. The response contributions for all frequencies in a sea state can be superposed, and we get the resulting response. However, for such a model the foil forces must be included together with a fluid-memory term and we are back where we started.

Using *Cummins* equation, and the state space fluid memory term, is an elegant way of including the frequency dependency of the added mass and potential damping. As *Cummins* equation is evaluated at infinite frequency, any force at any frequency can be excited on the system without concern. The fluid memory term can be understood as a filtered velocity term that acts as damping to the system. The filter can either be represented as a state-space model or a time-dependent retardation function (integral). The integral might give numerical difficulties, therefore a state-space representation is preferred (Fossen [2011]).

In the time-domain model, the force RAO's for waves and added resistance are used to represent the wave forces acting on the model.

Chapter 9

The Model and Verification

9.1 Ship model

The time-domain model is built, block by block in SIMULINK.

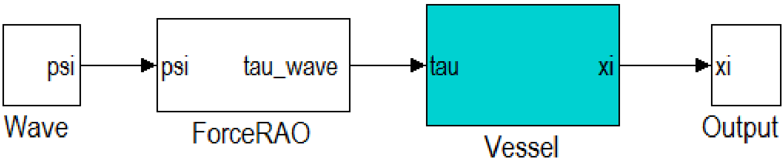

Figure 9.1: Vessel block diagram, with force RAO and a single frequency regular wave

Figure 9.1 illustrate the layout of the model of the UT-751 vessel. Here, a single frequency regular wave is excited on the system. By means of the force RAO the wave excitation forces (diffraction and Froude-Krylov forces) are applied onto the vessel. The structure of the vessel block follows from figure 9.2.

The vessel block is designed according to *Cummins* equation:

$$(\boldsymbol{M}_{RB} + \boldsymbol{M}_A(\infty))\ddot{\boldsymbol{\xi}} + \boldsymbol{C}_A^{VERES}\dot{\boldsymbol{\xi}} + \boldsymbol{B}(\infty)\dot{\boldsymbol{\xi}} + \boldsymbol{\mu} + \boldsymbol{C}\boldsymbol{\xi} = \boldsymbol{\tau} \tag{9.1}$$

where

$$\boldsymbol{\mu} = \int_0^t \boldsymbol{K}(t-\tau)\dot{\boldsymbol{\xi}}(\tau)d\tau \tag{9.2}$$

$$\boldsymbol{B}(\infty, U) = \boldsymbol{B}(\infty) + \boldsymbol{C}_A^{VERES} \tag{9.3}$$

$\boldsymbol{B}(\infty)$ approaches null for zero speed (seen in figure 2.5), and viscous effects are neglected. $\boldsymbol{C}_A^{VERES}$ is the speed dependent Coriolis coefficient, which can be either linear or non-linear

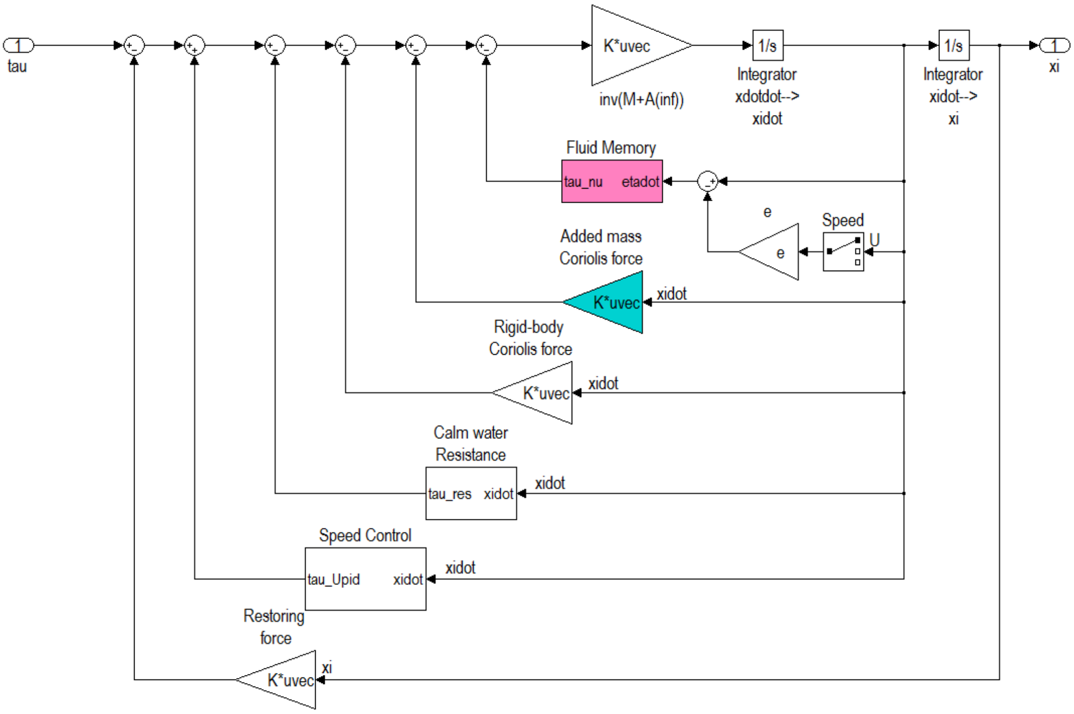
1
tau
K*uvec
inv(M+A(inf))
1/s
Integrator
xdotdot-->
xidot
1/s
Integrator
xidot-->
xi
1
xi
Fluid Memory
tau_nu
etadot
e
e
Speed
U
Added mass
Coriolis force
K*uvec
xidot
Rigid-body
Coriolis force
K*uvec
xidot
Calm water
Resistance
tau_res
xidot
xidot
Speed Control
tau_Upid
xidot
xidot
Restoring
force
K*uvec
xi

Figure 9.2: The vessel block according to *Cummins* formula. Cyan: Coriolis term. Pink: Fluid-memory state-space block

depending on the needs of the model. However, the differences between the two, have not been investigated. The sum of $\boldsymbol{B}(\infty)$ and $\boldsymbol{C}_A^{VERES}$ in heave and pitch is identical to the speed dependent damping matrix provided by VERES. For zero speed, the Coriolis term is zero. The rigid-body Coriolis term is always zero when the coordinates are expressed in the {s}-frame. $\boldsymbol{\mu}$ is the fluid memory term represented by the state-space model:

$$\boldsymbol{\mu}(s) = \boldsymbol{K}(s)\dot{\boldsymbol{\xi}} \tag{9.4}$$

where

$$\boldsymbol{K}(s) = \boldsymbol{C}_r(s\boldsymbol{I} - \boldsymbol{A}_r)^{-1}\boldsymbol{B}_r \tag{9.5}$$

The system coefficients $\boldsymbol{A}_r$, $\boldsymbol{B}_r$ and $\boldsymbol{C}_r$ are found by the *MSS FDI Toolbox* described in section 2.8.2. In figure 9.3 and 9.4 the response of the time domain model and the motion RAO steady-state response is given. We see that the solutions approach one another in time.

The comparison between the time-domain model and VERES' model in the frequency-domain is given in figures 3.4-3.9 in section 3.

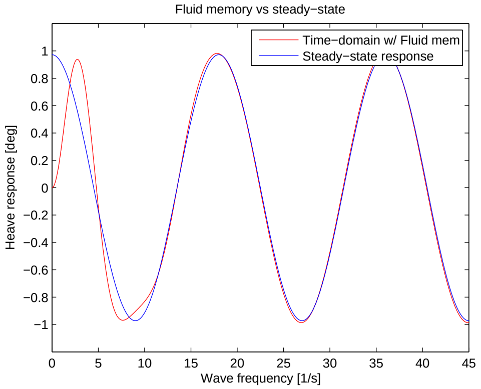

Figure 9.3: Time-domain- versus steady-state response for zero speed

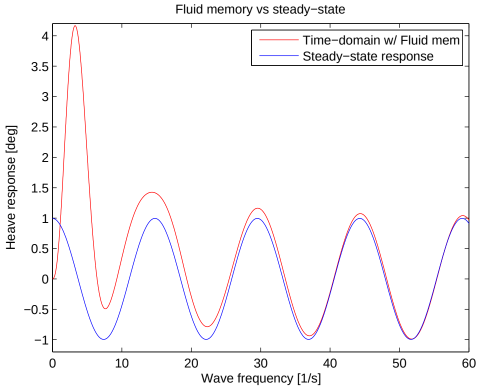

Figure 9.4: Time-domain- versus steady-state response at 12 kn

9.2 Foil model

The foil is model according to chapter 4. The combined vessel and foil model in SIMULINK is given in figure 9.5.

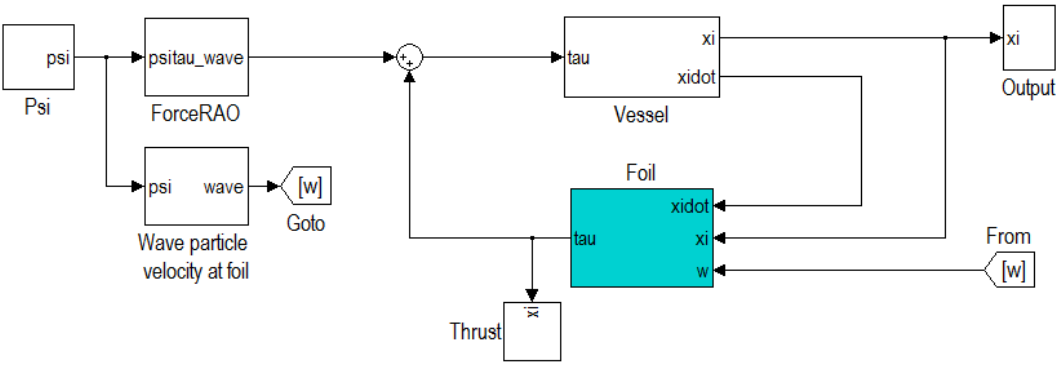
psi
Psi
psitau_wave
ForceRAO
psi
wave
Wave particle velocity at foil
[w]
Goto
+
+
tau
xi
xidot
Vessel
xi
Output
Foil
xidot
tau
xi
w
From
[w]
xi
Thrust

Figure 9.5: Combined vessel and foil model in SIMULINK

Simulations were performed on the combined model. Figures 9.7 and 9.8 illustrate the heave and pitch response at 8 kn. The heave response concur well with the experimental data in heave, while it overestimates slightly in pitch. Figures 9.9 and 9.10 show the heave and pitch response at 12 kn, where VERES seem to coincide better in heave while the time-domain formulation satisfy the pitch response better. In general, the time-domain model need some tuning but has potential.

9.3 Extended Simulations

There is definitely room for improvements of the model presented in the above. Nevertheless, the model was tested in a more advanced environment, to impute the possibilities that lies

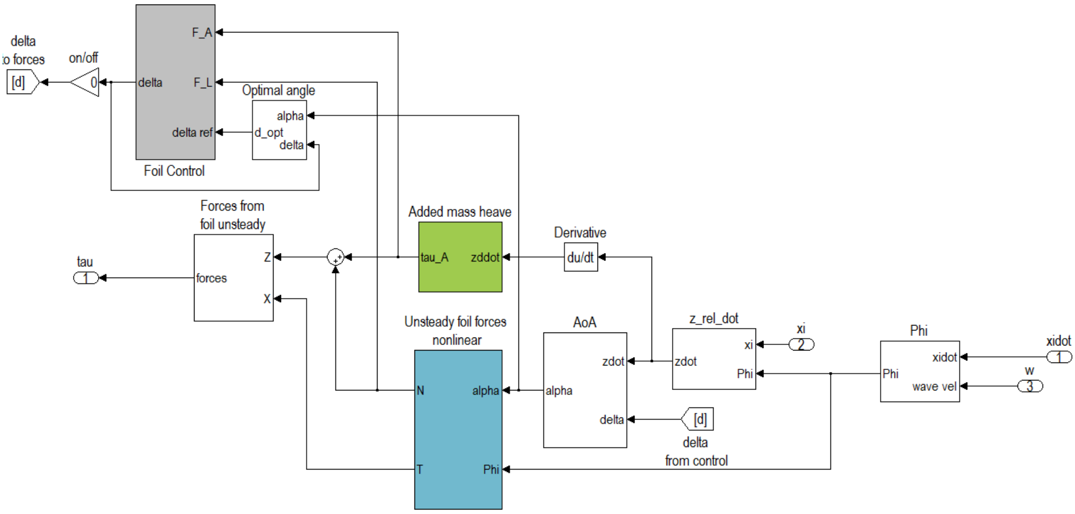
delta
to forces
[d]
on/off
0
F_A
delta
F_L
delta ref
Foil Control
Optimal angle
alpha
d_opt
delta
Forces from
foil unsteady
tau
1
forces
Z
X
Added mass heave
tau_A
zddot
Derivative
du/dt
Unsteady foil forces
nonlinear
N
alpha
T
Phi
AoA
zdot
alpha
delta
[d]
delta
from control
z_rel_dot
zdot
xi
Phi
xi
2
Phi
Phi
xidot
wave vel
xidot
1
w
3

Figure 9.6: Foil block diagram according to foil theory

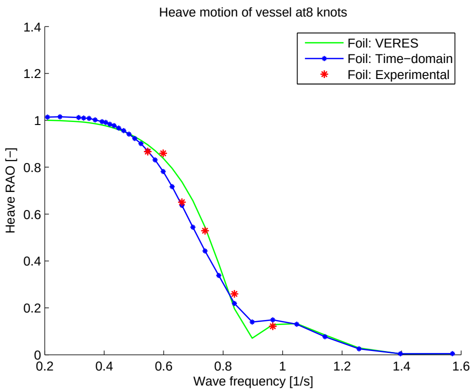

Figure 9.7: Time-domain heave response with foil. Blue: Time-domain. Green: VERES. Star: Experimental at 8 kn

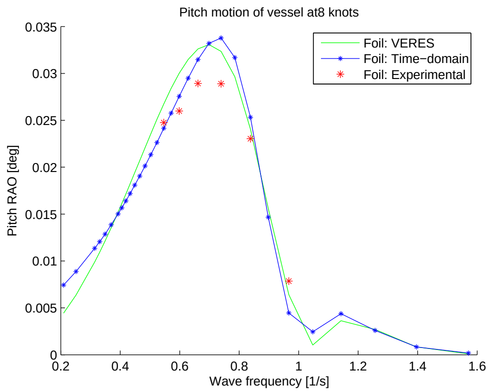

Figure 9.8: Time-domain pitch response with foil. Blue: Time-domain. Green: VERES. Star: Experimental at 8 kn

within reach when using a time based model. In this section, a six-degrees of freedom time-domain model with fluid memory was tested. The model is based on the same principles as outlined in the report so far, only now including added resistance, the experimental calm water resistance and speed control. It is stressed that the model bears uncertainties and that the results are to be regarded thereafter. The model is based on the following:

1. The original model is from the *MSS Toolbox* (Fossen [2011]) where adjustments have been made to fit the scope of work. A foil system is added, the water particle velocity and acceleration is calculated, the Coriolis terms are amended according to the theory presented in the report, the calm water resistance is included and speed control is fitted
2. The added resistance is based on VERES estimates for a vessel without foil. The reason

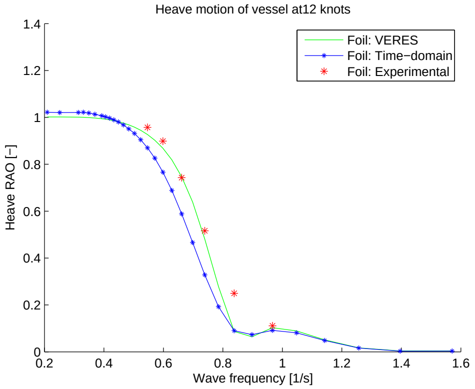

Figure 9.9: Time-domain heave response with foil. Blue: Time-domain. Green: VERES. Star: Experimental at 12 kn

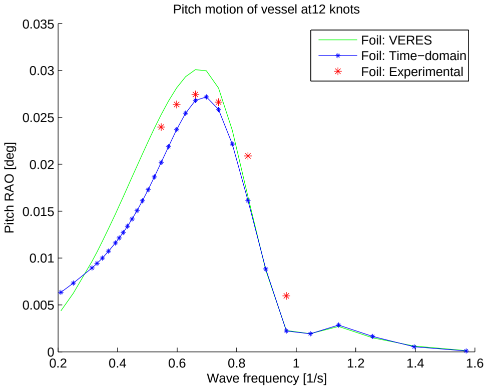

Figure 9.10: Time-domain pitch response with foil. Blue: Time-domain. Green: VERES. Star: Experimental at 12 kn

being that, the experimental results for the vessel with foil coincidently match VERES' result without foil, satisfactorily (seen from figures 7.17-7.21).

3. The calm water resistance is based on the experimental findings

9.3.1 Regular and irregular seas

For regular seas, the thrust force is calculated, and the results are visualised in figure 9.11. The results more or less concur with what we have experienced earlier, however the results worsened when altering the sea-state. In irregular seas, using the JONSWAP-spectrum for long-crested waves, with a significant wave height of 3 m, the thrust-efficiency was reduced drastically. The validity of the results is questionable. Nevertheless, the figures in 9.12 represent the thrust found. Figure 9.13 graph the spectrum and 9.14 visualise the sea-state used in the simulation. A more scientific approach, regarding the implementation of the foil propulsion system in irregular seas will be left for further work.

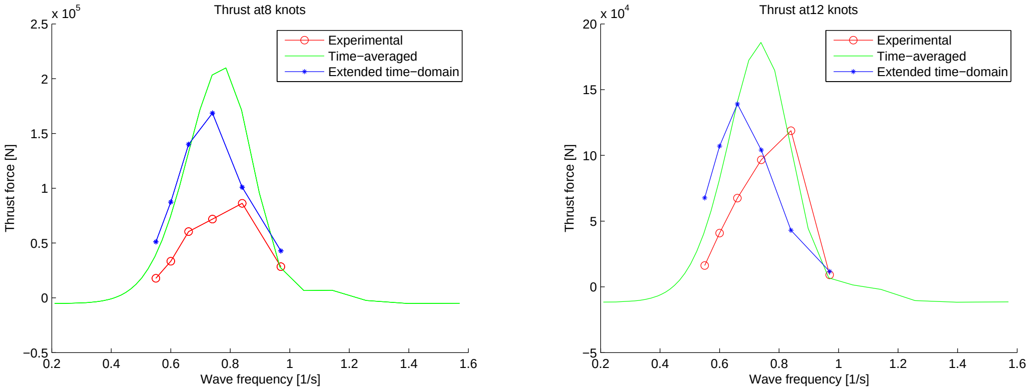

Figure 9.11: Thrust for extended model at 8 *kn* (left) and 12 *kn* (right). Blue-star: Time-domain. Red-circle: Experimental. Green: Time-averaged

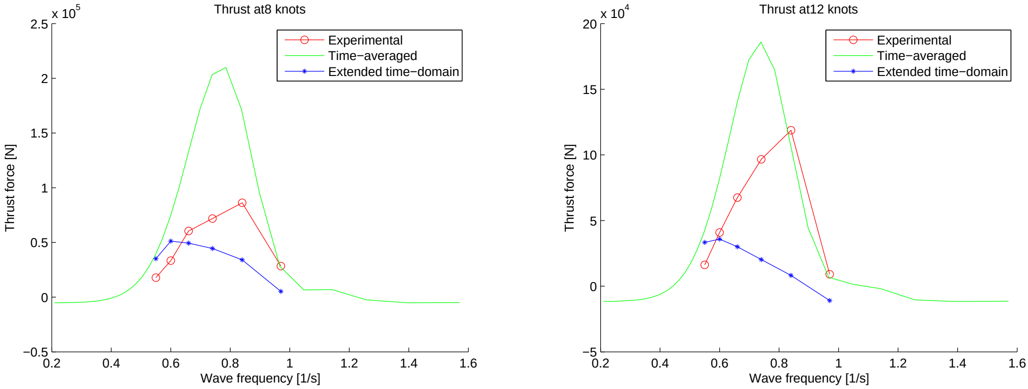

Figure 9.12: Thrust for extended model at 8 *kn* (left) and 12 *kn* (right). Blue-star: Time-domain in irregular sea. Red-circle: Experimental in regular waves. Green: Time-averaged in regular wave

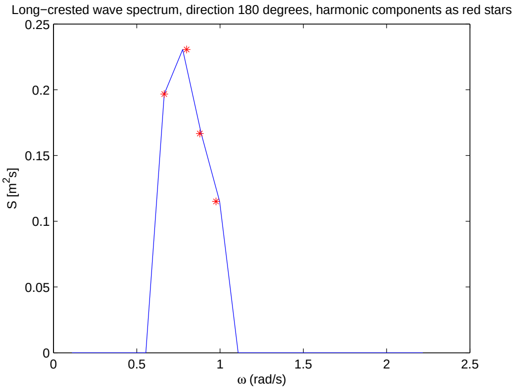

Figure 9.13: JONSWAP spectrum for irregular seas with significant wave height of 3 *m*. Plot produced by the *MSS Toolbox* (Fossen and Perez [2004])

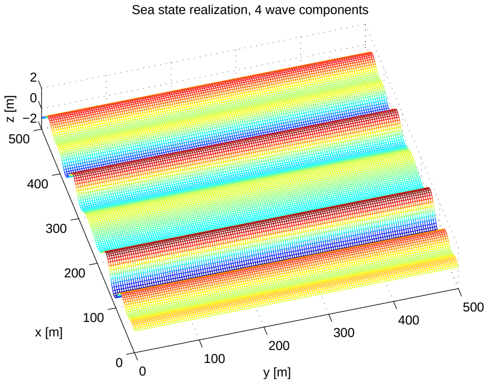

Figure 9.14: Sea-state visualisation of the long-crested JONSWAP spectrum at $T_p = 8.5\ s$

Chapter 10

Conclusions and Discussions

This master thesis has evolved into a discussion of methods for modelling a foil propulsion system. The main emphasis has been on understanding the dynamics of a foil and a vessel, to deliberately be able to suggest a mathematical model that serves the purpose. In line, the author believes that a strong mathematical model is essential in verifying the potential of a foil propulsion system.

Mathematical theory has been revised, and different vessel- and foil models have been suggested and verified throughout the report. As a basis for the verification, VERES has been used extensively. VERES is a trusted computational program that provides hydrodynamic data that has proven to match exceptionally well with the experimental data. However, the hydrodynamic data from VERES is frequency-domain based, while this report has been concerned with time-domain simulations of the vessel-foil system. A time-domain model is more robust and versatile when it comes to control system design and non-linearities. Additionally, time-domain simulations allows the user to interact with the model in a simple manner, which makes it flexible and transparent. For more intricate and complicated simulations this is important.

For the simulations of the foil propulsion system, a time-domain model based on Cummins [1962]' equation and Ogilvie [1964]'s transformation is suggested. *Cummins* equation evaluates the equation of motion in an infinite frequency regime. Fluid memory effects account for the frequency dependency. The fluid memory effects were included using the *MSS Toolbox* and a state-space representation. One of the benefits of using *Cummins*' equation is that the $1/\omega_e^2$-terms, which normally are an important part of the added mass and damping coefficients, according to STF-theory, vanishes. Consequently, the equation is applicable to any frequency, without the numerical problems that follows from the singularities.

Moreover, an alternative approach to using the STF coefficients is proposed. The basis for the approach was motivated by Fossen [2011] and *Fossen*'s use of mechanical transformation between coordinate system, to account for speed-dependent effects in the hydrodynamic coefficients. Fossen [2011] utilises an energy approach to identify Coriolis terms in the equation of motion. It is shown that, the Coriolis term due to added mass matches the speed-dependent terms in the STF-theory. In other words, speed-dependency of the damping and added mass matrices (exempting hull-lift damping) is a direct consequence of mechanical transformation in space, from one reference frame to the other. It is noted that the result is only verified when using *Cummins*' equation. The link between the STF-theory (and thus VERES' coefficients) and the Coriolis term, is to the authors understanding unique and is not referred to in literature. The findings were a direct result of discussions with Thor Inge Fossen, Professor of Guidance, Navigation and Control at NTNU. Using the *Cummins* equation and including the Coriolis term, is the basis for the time-domain model used for the foil propulsion simulations.

The model was tested against VERES' frequency-domain approach with satisfactory results. At zero speed, the time-domain model matches VERES perfectly. As the speed increases, there is a dip in the heave motion RAO around pitch resonance, compared to VERES, a behaviour that is unclear at this point. A possible explanation is the omitted hull-lift damping terms that are included in VERES' analysis. Furthermore, the VERES and time-domain model was compared to experimental data from the towing tank, with reasonable correlation. However, this far VERES, seem to estimate the response more accurately. Concluding, the time-domain model is still premature, however the author believes it bears potential to be a rigid simulation base, both for analysis of foil propulsion systems and other marine operations, in the future.

Also included in the report, is the results of several model tests. In general, the results from the test were promising with regards to reducing overall vessel resistance. The thrust-producing capacity of the vessel-foil system was significant. Firstly, the foil was tested in the Marine Cybernetics laboratory. The experiments gave important insight on the characteristics of the chosen foil profile, and its performance in a dynamic flow field. The results were the basis for the active control algorithm that was to be used in the towing tank. The hypothesis was that, using active control could maximise thrust and avoid foil stall. However, the system did not operate optimally and the results from the active control model tests were poor. Consequently, the emphasis of this report was shifted towards designing an effective simulation model. It seemed logical that a simulation model should be in place before designing the control system of the foil.

Regarding the results from the model tests, under optimal conditions and in head sea for regular waves of magnitude 3 m the resistance reduction peaked at 65%. The reduction in heave response peaked at more than 60% while the pitch response was reduced by 50%, at maximum.

Chapter 11

Recommendations for Further Work

In this thesis some aspect of vessel and foil modelling has been covered, and many more are left undiscovered. Some of the recommendations for further work follow:

Verification :
A time-domain model based on *Cummins*' equation has been proposed. However, the model deviate from the VERES model when the speed increases. The reason for this is unclear and should be evaluated

Expanding :
The time-domain model is fit for expansion and should be evaluated in irregular seas, at different headings and at larger range of speeds. The foil effects in roll damping should also investigated

Foil control :
When the model is completely verified a control system can be included

Foil propeller :
It would have been interesting to evaluate the efficiency of a foil propulsion system that was modified to act as a a stand-alone propulsion system, say in calm seas, by subjecting the foil to a forced oscillations

Extremum-seekeing : Extremum-seeking build son the concept of finding an optimal set-point, without the basis of a mathematical model. Such a system could be of interest for a foil propulsion system

Bibliography

Kinematics, Aeromechanics 1 Notes. Purdue University, 2011.

J. G. Balchen, T. Andresen, and B. A. Foss. *Reguleringsteknikk.* NTNU-Trykk, 2004.

C. T. Borgen. Application of an active foil propeller. Master's thesis, NTNU, 2010.

W. E. Cummins. The impulse response function and ship motions. Technical report, Department of the Navy David Taylor Model Basin, January 1962.

R. G. Dean and R. A. Dalrymple. *Water Wave Mechanics for Engineers and Scientists.* World Scientific Publishing, 1991.

O. Egeland and T. Gravdahl. *Modeling and Simulation for Automatic Control.* Marine Cybernetics, 2002.

O. M. Faltinsen. *Sea Loads on Ships and Offshore Structures.* Cambridge University Press, 1990.

O. M. Faltinsen. *Hydrodynamics of High-Speed Marine Vehicles.* Cambridge University Press, 2005.

D. Fathi. User manual - shipx vessel responses (veres). Technical report, MARINTEK, SINTEF Group, 2010.

D. Fathi and J. R. Hoff. User manual - shipx veres theory manual. Technical report, MARINTEK, SINTEF Group, 2010.

T. I. Fossen. A nonlinear unified state-space model for ship maneuvering and contril in seaway. *Journal of Bifurcation and Chaos*, 2005.

T. I. Fossen. *Handbook of Marine Craft Hydrodynamics and Motion Control.* WILEY, 2011.

T. I. Fossen and T. Perez. Mss toolbox. www.marinecontrol.org, 2004. MATLAB Toolbox.

J. Gerritsma and W. Beukelman. Analysis of the resistance increase in waves of a fast cargo ship. *Intern Shipbuilding Program*, pages 285–293, 1972.

M. Greco. Lecture notes - sea loads on ships and offshore structures. Hand-out in lecture, 2010.

E. Kristiansen and O. Egeland. Frequency-dependent added mass in models for controller design for wave motion damping. In *IFAC*. 2003.

L. R. Marshall, A. H. Nayfeh, and D. T. Mook. Forward speed effects in the equations of ship motion. *Journal of Sound and Vibration*, (85):303–313, 1982.

J. N. Newman. *Marine Hydrodynamics.* The MIT Press, 1977.

T. F. Ogilvie. Recent progress towards the understanding and prediction of ship motions. In *Proceedings of the 5th Symposium on Naval Hydrodynamics*, pages 3–79, 1964.

T. Perez and T. I. Fossen. Time- vs. frequency-domain identification of parametric rafiation force models for marine structures at zero speed.

J. A. Pinkster and G. van Oortmessen. Computation ot the first- and second-order wave forces on oscillating bodies in regular waves. In *Proc. Second Int. Conf. Numerical Ship Hydrodynamics*, 1977.

T. Perez R. Taghipour and T. Moan. Hybrid frequency-time domain models for dynamic response analysis of marine structures. *Ocean Engineering*, (35), 2008.

N. Salvesen, E. O. Tuck, and O. M. Faltinsen. Ship motions and sea loads. In *The Society of Navel Architects and Marine Engineers*, 1970.

S. Steen. Motstand og propulsjon, propell- og foilteori, 2007.

J.R. Taylor. *Classical Mechanics.* Sausalito CA: UNiversity Science Books, 2004.

T. Theodorsen. General theory of aerodynamic instability and the mechanism of flutter. Technical Report 496, National Advisory Committee for aeronautics, 1935.

T. Wahl. Personal assistance from torgeir wahl at ntnu.

www.ni.com. National instruments inc. Official webpages.

Appendix A

Rigid-body kinetics

Rigid-body kinetics

An equation of motion is always computed with respect to the centre of gravity CG. In order to solve the equation of motion, the acceleration (and velocity) at CG must be known. However, hydrodynamic coefficients are often computed with respect to an arbitrary centre of origin. Hence, the body-fixed coordinate system is placed at CO while the acceleration is found at CG. The distance between CO and CG is $\boldsymbol{r}_g$, while the distance from the inertial coordinate system to its body-fixed equivalent (CO) is $\boldsymbol{r}_0$.

Firstly, we seek the translational motion about CO and define the vectors from A.1

$$\boldsymbol{r}_g = \sum_{i=1}^{3} x_i \hat{\boldsymbol{u}}_i \tag{A.1}$$

$$\boldsymbol{r}_0 = \sum_{i=1}^{3} y_i \hat{\boldsymbol{v}}_i \tag{A.2}$$

where $\hat{\boldsymbol{u}} = [\hat{\boldsymbol{\imath}}, \hat{\boldsymbol{\jmath}}, \hat{\boldsymbol{k}}]$ is the unit vector of the body-fixed coordinates and x_i is the distance between CO and CG in direction i. $\hat{\boldsymbol{v}} = [\hat{\boldsymbol{\imath}}, \hat{\boldsymbol{\jmath}}, \hat{\boldsymbol{k}}]$ is the unit vector for the inertial system, while y_i is the distance between the inertial origin and CO in direction i. The vector from the inertial frame to CG is then

$$\begin{aligned}\boldsymbol{r} &= \boldsymbol{r}_0 + \boldsymbol{r}_g \\ &= \sum_{i=1}^{3} y_i \hat{\boldsymbol{v}}_i + \sum_{i=1}^{3} x_i \hat{\boldsymbol{u}}_i\end{aligned} \tag{A.3}$$

and the velocity is found by differentiation in time

$$\begin{aligned}\dot{\boldsymbol{r}} &= \dot{\boldsymbol{r}}_0 + \dot{\boldsymbol{r}}_g \\ &= \sum_{i=1}^{3} \dot{y}_i \hat{\boldsymbol{v}}_i + \sum_{i=1}^{3} y_i \dot{\hat{\boldsymbol{v}}}_i + \sum_{i=1}^{3} \dot{x}_i \hat{\boldsymbol{u}}_i + \sum_{i=1}^{3} x_i \dot{\hat{\boldsymbol{u}}}_i\end{aligned} \tag{A.4}$$

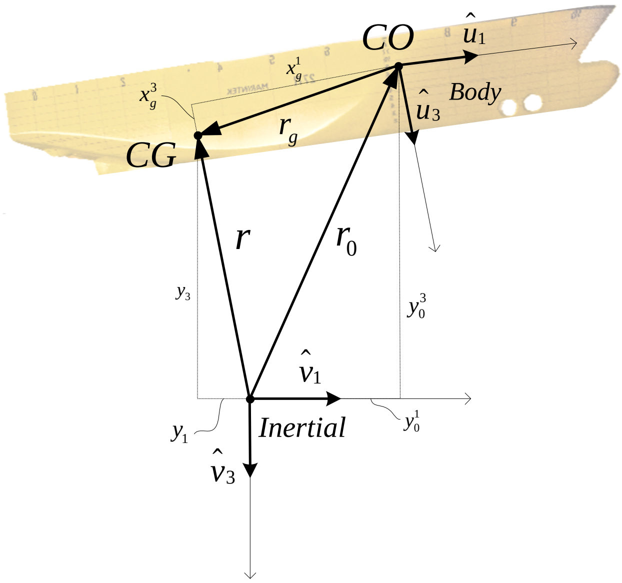

Figure A.1: Rigid-body kinematics

where the unit vector time derivative can be expressed as[1]

$$\dot{\hat{\boldsymbol{u}}} = \dot{\boldsymbol{\theta}}_{\hat{u}} \times \hat{\boldsymbol{u}} = \boldsymbol{\omega}_{\hat{u}} \times \hat{\boldsymbol{u}} \tag{A.5}$$

and $\boldsymbol{\omega}_u$ is the angular velocity of the body-fixed coordinate system relative to the inertial frame. From (A.4) it is made clear that time differentiation of a vector in a moving reference frame is

$$\frac{d\boldsymbol{r}_g}{dt} = \boldsymbol{v}_g^{\hat{u}} + \boldsymbol{\omega}_{\hat{u}} \times \boldsymbol{r}_g \tag{A.6}$$

$$= \left(\frac{d}{dt} + \boldsymbol{\omega}_{\hat{u}} \times \right) \boldsymbol{r}_g \tag{A.7}$$

where we have used

$$\sum_{i=1}^{3} \dot{x}_i \hat{\boldsymbol{u}} = \boldsymbol{v}_g^{\hat{u}} \tag{A.8}$$

$$\sum_{i=1}^{3} x_i (\boldsymbol{\omega}_{\hat{u}} \times \hat{\boldsymbol{u}}) = \boldsymbol{\omega}_{\hat{u}} \times \sum_{i=1}^{3} x_i \hat{\boldsymbol{u}} = \boldsymbol{\omega}_{\hat{u}} \times \boldsymbol{r}_g \tag{A.9}$$

---

[1] From [Taylor, 2004, pg. 343]

(A.6) is known as the basic kinematic equation.[1]

On the other hand, the axes of the inertial system are fast and the time derivative of the unit vector ($\boldsymbol{\omega}_{\hat{v}}$) is zero (the earth's motion relative to a star-fixed inertial system is eliminated) and we define

$$\dot{\hat{\boldsymbol{v}}} = \boldsymbol{\omega}_{\hat{v}} \times \hat{\boldsymbol{v}} = 0 \tag{A.10}$$

Now, (A.4), (A.5) and (A.10) combines to

$$\boldsymbol{v} = \dot{\boldsymbol{r}} = \sum_{i=1}^{3} \dot{y}_i \hat{\boldsymbol{v}}_i + \sum_{i=1}^{3} \dot{x}_i \hat{\boldsymbol{u}}_i + \sum_{i=1}^{3} x_i (\boldsymbol{\omega}_{\hat{u}} \times \hat{\boldsymbol{u}}) \tag{A.11}$$

and the acceleration exist so that

$$\begin{aligned}
\dot{\boldsymbol{v}} = & \sum_{i=1}^{3} \ddot{y}_i \hat{\boldsymbol{v}}_i + \sum_{i=1}^{3} \ddot{x}_i \hat{\boldsymbol{u}}_i + \sum_{i=1}^{3} \dot{x}_i \dot{\hat{\boldsymbol{u}}}_i \\
& + \sum_{i=1}^{3} \dot{x}_i (\boldsymbol{\omega}_{\hat{u}} \times \hat{\boldsymbol{u}}) + \sum_{i=1}^{3} x_i [(\dot{\boldsymbol{\omega}}_{\hat{u}} \times \hat{\boldsymbol{u}}) + (\boldsymbol{\omega}_{\hat{u}} \times \dot{\hat{\boldsymbol{u}}})] && \text{(A.12)} \\
= & \sum_{i=1}^{3} \ddot{y}_i \hat{\boldsymbol{v}}_i + \sum_{i=1}^{3} \ddot{x}_i \hat{\boldsymbol{u}}_i + 2\boldsymbol{\omega}_{\hat{u}} \times \sum_{i=1}^{3} \dot{x}_i \hat{\boldsymbol{u}} + \boldsymbol{\alpha}_{\hat{u}} \times \sum_{i=1}^{3} x_i \hat{\boldsymbol{u}} && \text{(A.13)} \\
& + \boldsymbol{\omega}_{\hat{u}} \times (\boldsymbol{\omega}_{\hat{u}} \times \sum_{i=1}^{3} x_i \hat{\boldsymbol{u}}) && \text{(A.14)}
\end{aligned}$$

By using the identities from (A.8)-(A.9) and simplifying we find the resulting fictitious acceleration acting on CG:

$$\dot{\boldsymbol{v}} = \dot{\boldsymbol{v}}_0^{\hat{v}} \; + \; \dot{\boldsymbol{v}}_g^{\hat{u}} \; + \; \underbrace{2\boldsymbol{\omega}_{\hat{u}} \times \boldsymbol{v}_g^{\hat{u}}}_{Coriolis\ acc} \; + \; \underbrace{\dot{\boldsymbol{\omega}}_{\hat{u}} \times \boldsymbol{r}_g}_{Transversal\ acc} \; + \; \underbrace{\boldsymbol{\omega}_{\hat{u}} \times (\boldsymbol{\omega}_{\hat{u}} \times \boldsymbol{r}_g)}_{Centripetal\ acc} \tag{A.15}$$

where $\dot{\boldsymbol{\omega}}_{\hat{u}}$ is the angular acceleration and $\dot{\boldsymbol{v}}_g^{\hat{u}}$ the linear acceleration of $\boldsymbol{r}_g$, in body-coordinates. $\dot{\boldsymbol{v}}_0^{\hat{v}}$ is the acceleration of CO in the inertial frame. Assuming that CG is fixed in the body-frame then $\boldsymbol{r}_g$ is constant. Subsequently, $\boldsymbol{v}_g^{\hat{u}} = 0$ and $\dot{\boldsymbol{v}}_g^{\hat{u}} = 0$, and the Coriolis-acceleration dissipates. In summary, the acceleration is

$$\dot{\boldsymbol{v}} = \dot{\boldsymbol{v}}_0^{\hat{v}} \; + \; \dot{\boldsymbol{\omega}}_{\hat{u}} \times \boldsymbol{r}_g \; + \; \boldsymbol{\omega}_{\hat{u}} \times (\boldsymbol{\omega}_{\hat{u}} \times \boldsymbol{r}_g)\Big|_{\boldsymbol{r}_g fixed} \tag{A.16}$$

whereas, under the same convention the velocity from (A.11) yields

$$\boldsymbol{v} = \boldsymbol{v}_0^{\hat{v}} \; + \; \boldsymbol{\omega}_{\hat{u}} \times \boldsymbol{r}_g \tag{A.17}$$

---

[1] From [Cor, 2011, pg. 213]

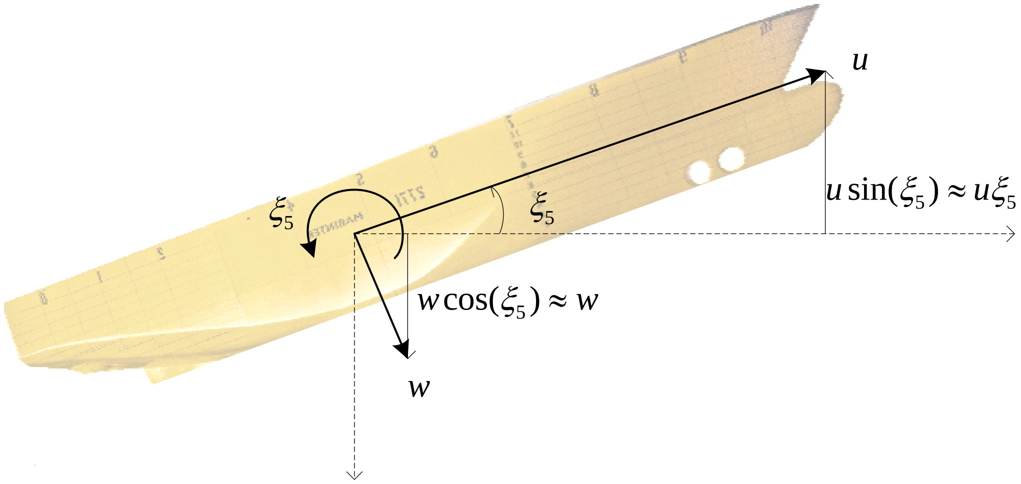

Figure A.2: Geometry of vessel at an exaggerated angle, at forward speed

The one remaining task is to translate $\boldsymbol{v}_0^{\hat{v}}$ and $\dot{\boldsymbol{v}}_0^{\hat{v}}$ from the inertial frame to the body-fixed frame. The velocity is found from a geometrical perspective, as illustrated in figure A.2. In accordance with figure A.2, the vertical velocity can be denoted

$$\begin{aligned} v_3 &= w\cos(\xi_5) - u\sin(\xi_5) && \text{(A.18)} \\ &\approx w - u\xi_5 && \text{(A.19)} \end{aligned}$$

where all angles are assumed small, i.e linear theory. The velocity $\boldsymbol{v}_{\hat{v}}$ can be generalized in body-fixed coordinates as follows

$$\boldsymbol{v}_0^{\hat{v}} = \boldsymbol{v}_{\hat{u}} + \boldsymbol{\xi}_{4,5,6} \times \boldsymbol{v}_{\hat{u}} \tag{A.20}$$

where $\boldsymbol{\xi}_{4,5,6}$ are the seakeeping angles (assuming zero heading and translation along x-axis). The acceleration $\dot{\boldsymbol{v}}_{\hat{v}}$ is found by the kinematic relation in (A.6) as

$$\dot{\boldsymbol{v}}_0^{\hat{v}} = \dot{\boldsymbol{v}}_{\hat{u}} + \boldsymbol{\omega}_{\hat{u}} \times \boldsymbol{v}_{\hat{u}} \tag{A.21}$$

Finally, the linear velocity and acceleration of CG with respect to the inertial frame, expressed in body-fixed coordinates becomes

$$\begin{aligned} \boldsymbol{v} &= \boldsymbol{v}_{\hat{u}} \;+\; \boldsymbol{\theta}_{\hat{u}} \times \boldsymbol{v}_{\hat{u}} \;+\; \boldsymbol{\omega}_{\hat{u}} \times \boldsymbol{r}_g && \text{(A.22)} \\ \dot{\boldsymbol{v}} &= \dot{\boldsymbol{v}}_{\hat{u}} \;+\; \boldsymbol{\omega}_{\hat{u}} \times \boldsymbol{v}_{\hat{u}} \;+\; \boldsymbol{\alpha}_{\hat{u}} \times \boldsymbol{r}_g \;+\; \boldsymbol{\omega}_{\hat{u}} \times (\boldsymbol{\omega}_{\hat{u}} \times \boldsymbol{r}_g) && \text{(A.23)} \end{aligned}$$

Similarly, and by using the Parallel-axes Theorem, the rotational motion about CO can be derived (Egeland and Gravdahl [2002], Fossen [2011]). This will not be done here.

Newton's **second law revisited**

Restating *Newton's* second law from (2.1) as

$$\boldsymbol{Ma} = \boldsymbol{\tau}_{hyd} + \boldsymbol{\tau}_{hs} \tag{A.24}$$

where $\boldsymbol{a}$ is the acceleration. Inserting (A.23) and the force due to rotational acceleration ([Fossen, 2011, pg. 52]), we get

$$\boldsymbol{M}_{RB}\dot{\boldsymbol{\nu}} + \boldsymbol{C}_{RB}(\boldsymbol{\nu})\boldsymbol{\nu} = \boldsymbol{\tau}_{hyd} + \boldsymbol{\tau}_{hs} \tag{A.25}$$

where we have used *Fossen*'s notation $\boldsymbol{\nu} = [\boldsymbol{v}_{\hat{u}}, \boldsymbol{\omega}_{\hat{u}}]$ and $\dot{\boldsymbol{\nu}} = [\dot{\boldsymbol{v}}_{\hat{u}}, \dot{\boldsymbol{\omega}}_{\hat{u}}]$. Here, $\boldsymbol{M}_{RB}$ is the rigid-body mass matrix accounting for the position of CG with regards to CO. The non-linear $\boldsymbol{C}_{RB}(\boldsymbol{\nu})$ is called the Coriolis-Centripetal matrix, even though the Coriolis-term in (A.15) is cancelled out.

Appendix B

Programming flow

For the courtesy of others, who are to implement a LabView project that interacts with a SIMULINK model and I/O modules, the programming flow goes as follows:

1. Create a FPGA-project and a VI
2. Create a SIMULINK model. The model must include the *Signal Probe* block, standing freely. All input and output ports must be of *SIT in/out* type for compatibility. The blocks are found under the NI SIT Blocks in SIMULINK, provided the SIT and Real-Time Workshop is installed
3. In SIMULINK, choose 'Simulation' and 'Configuration Parameters'
    (a) Under 'Solver':
        i. Set 'Stop time' to *inf*. This must be done as the model is to run real-time
        ii. Set 'Type' to *Fixed-step* in the drop-down menu
        iii. Set 'Fixed-step size' to *0.02*, or the step-size corresponding to your sampling frequency in the experiment
    (b) Under 'Real-Time Workshop':
        i. Find 'Browse' in 'Target Selction'. Choose 'nidll.tlc - NI Real-Time target...'. Click 'OK', 'Build' and 'Apply' if prompted. Set the MATLAB 'Current Directory' to the directory in which you are working
        ii. Find 'Browse' again. Choose 'nidll_vxworks.tlc - NI Real-Time VxWorks...'. Click 'OK', 'Build' and 'Apply', if prompted
4. Exit 'Configuration Parameters' by clicking 'OK'. We are done in SIMULINK
5. Connect the CompactRIO device to the network so that your computer recognises the device
6. Go to the LabView VI. Insert all the features that are applicable; graphs, variable controls etc.
7. Under 'Tools', find 'SIT Connection Manager'

    (a) Under 'Model and Host':
        i. Browse 'Real-Time Target' and click 'Change'. Choose 'Existing target or Device' and 'Discover an..'
            A. Find 'Real-Time CompactRIO' and choose '*name of device*'. You need to know the name of your CompactRIO i.e 'NI-cRIO9974-0154C2CF'
            B. Click 'OK'
        ii. Browse 'Current Model DLL'. Choose the DLL-file that was created by SIMULINK
        iii. Browse 'Project Directory'. Choose 'Use current...' and choose the folder in which you work
    (b) Go to 'Mappings'. Here, all the indicators and controllers in the VI are mapped to the variables and input- and output ports of the original SIMULINK model. Map them by clicking 'Change Mapping'
    (c) Find 'Data LoggingÃÿ if data log is to be used. The data log files are stored on the CompactRIO and can be accessed through FTP. The files re found under 'ni-rt/system'
    (d) Go to 'Hardware I/O'. When the FPGA is configured, the input and output modules can be found by clicking 'Configure HW I/O'. Here the analogue I/O signals can be mapped to their cohering model I/O's
    (e) We are done in the 'SIT Connection Manager' window

8. The VI should now be compatible and communicate with the Real-Time target. The project can be run by clicking 'Operate' and 'Run'